Human stem cell-based models to analyze the pathophysiology of motor neuron diseases

Humane Stammzell-basierte Modelle zur Analyse der Pathophysiologie von Motoneuronerkrankungen

Doctoral thesis for a doctoral degree
at the Graduate School of Life Sciences,
Julius-Maximilians-Universität Würzburg,
Section Neuroscience

submitted by
Bita Massih

from
Hamburg, Germany

Würzburg 2023

Submitted on: ……..……..

Office stamp

Members of the Thesis Committee

Chairperson: Prof. Dr. Carmen Villmann

Primary Supervisor: Dr. Patrick Lüningschrör

Supervisor (Second): Prof. Dr. Erhard Wischmeyer

Supervisor (Third): Prof. Dr. Dr. Andreas Hermann

“sometimes your words just hypnotize me”

Table of contents

1 Summary

Motor neuron diseases (MNDs) encompass a variety of clinically and genetically heterogeneous disorders, which lead to the degeneration of motor neurons (MNs) and impaired motor functions. MNs coordinate and control movement by transmitting their signal to a target muscle cell. The synaptic endings of the MN axon and the contact site of the muscle cell thereby form the presynaptic and postsynaptic structures of the neuromuscular junction (NMJ). In MNDs, synaptic dysfunction and synapse elimination precede MN loss suggesting that the NMJ is an early target in the pathophysiological cascade leading to MN death. In this study, we established new experimental strategies to analyze human MNDs by patient derived induced pluripotent stem cells (iPSCs) and investigated pathophysiological mechanisms in two different MNDs.

To study human MNDs, specialized cell culture systems that enable the connection of MNs to their target muscle cells are required to allow the formation of NMJs. In the first part of this study, we established and validated a human neuromuscular co-culture system consisting of iPSC derived MNs and 3D skeletal muscle tissue derived from myoblasts. We generated 3D muscle tissue by culturing primary myoblasts in a defined extracellular matrix in self-microfabricated silicone dishes that support the 3D tissue formation. Subsequently, iPSCs from healthy donors and iPSCs from patients with the progressive MND Amyotrophic Lateral Sclerosis (ALS) were differentiated into MNs and used for 3D neuromuscular co-cultures. Using a combination of immunohistochemistry, calcium imaging, and pharmacological stimulations, we characterized and confirmed the functionality of the 3D muscle tissue and the 3D neuromuscular co-cultures. Finally, we applied this system as an *in vitro* model to study the pathophysiology of ALS and found a decrease in neuromuscular coupling, muscle contraction, and axonal outgrowth in co-cultures with MNs harboring ALS-linked superoxide dismutase 1 (*SOD1*) mutation. In summary, this co-culture system presents a human model for MNDs that can recapitulate aspects of ALS pathophysiology.

In the second part of this study, we identified an impaired unconventional protein secretion (UPS) of Sod1 as pathological mechanisms in Pleckstrin homology domain-containing family G member 5 (*Plekhg5*)-associated MND. Sod1 is a leaderless cytosolic protein which is secreted in an autophagy-dependent manner. We found that Plekhg5 depletion in primary MNs and NSC34 cells leads to an impaired secretion of wildtype Sod1, indicating that Plekhg5 drives the UPS of Sod1 *in vitro*. By interfering with different steps during the biogenesis of autophagosomes, we could show that Plekhg5-regulated Sod1 secretion is determined by autophagy. To analyze our findings in a clinically more relevant model we utilized human iPSC MNs from healthy donors and ALS patients with *SOD1* mutations. We observed reduced SOD1 secretion in ALS MNs which coincides with reduced protein expression of PLEKHG5 compared to healthy and isogenic control MNs. To confirm this correlation, we depleted PLEKHG5 in

control MNs and found reduced extracellular SOD1 levels, implying that SOD1 secretion depends on PLEKHG5. In summary, we found that Plekh5 regulates the UPS of Sod1 in mouse and human MNs and that Sod1 secretion occurs in an autophagy dependent manner. Our data shows an unreported mechanistic link between two MND-associated proteins.

2 Zusammenfassung

Motoneuronerkrankungen (MNE) umfassen eine Vielzahl klinisch und genetisch heterogener Erkrankungen, die zur Degeneration von Motoneuronen (MN) und zu beeinträchtigten motorischen Funktionen führen. MN koordinieren und steuern Muskelbewegungen, indem sie ihr Signal an eine Zielmuskelzelle übertragen. Die synaptischen Endungen des MN-Axons und die Kontaktstelle der Muskelzelle bilden dabei die präsynaptischen und postsynaptischen Strukturen der neuromuskulären Endplatte (NME). Bei MNE zeichnen sich synaptische Dysfunktion und Synapseneliminierung bereits vor dem Verlust von MN ab, was darauf hindeutet, dass die NME ein frühes Ziel in der pathophysiologischen Kaskade ist, die zum MN-Tod führt. In dieser Studie haben wir neue experimentelle Strategien zur Analyse humaner MNE mithilfe von humanen induzierten pluripotenten Stammzellen (iPSZ) entwickelt und pathophysiologische Mechanismen bei zwei verschiedenen MNE untersucht.

Um humane MNE zu untersuchen sind Zellkultursysteme erforderlich, die die Verbindung von MN mit ihren Zielmuskelzellen ermöglichen, um NME zu bilden. Im ersten Teil dieser Studie haben wir ein humanes neuromuskuläres Co-Kultursystem etabliert und validiert, das aus iPSZ abgeleiteten MN und 3D Skelettmuskelgewebe aus Myoblasten besteht. Wir haben 3D Muskelgewebe erzeugt, indem wir primäre Myoblasten in einer definierten extrazellulären Matrix in selbst gefertigten Silikonschalen kultivierten, die die 3D-Gewebebildung unterstützen. Anschließend wurden iPSZ von gesunden Spendern und iPSZ von Patienten mit der MNE Amyotrophe Lateralsklerose (ALS) in MN differenziert und für neuromuskuläre 3D Co-Kulturen verwendet. Mithilfe von immunhistochemischen Untersuchungen, Calcium-Imaging und pharmakologischen Stimulationen konnten wir die Funktionalität des 3D Muskelgewebes und neuromuskulären 3D Co-Kulturen charakterisieren und validieren. Anschließend wurde das System als in vitro Modell zur Untersuchung der Pathophysiologie von ALS verwendet. ALS Co-Kulturen mit MN, die eine Superoxid Dismutase 1 (*SOD1*)-Genmutation aufwiesen, zeigten eine Abnahme der neuromuskulären Verbindung, der Muskelkontraktion und des axonalen Wachstums. Zusammenfassend stellt dieses Co-Kultursystem ein humanes Modell für die Untersuchung von MNE dar, das Aspekte der ALS-Physiologie rekapitulieren kann.

Im zweiten Teil dieser Studie konnten wir eine Beeinträchtigung der unkonventionellen Proteinsekretion (UPS) von Sod1 als pathologischen Mechanismus bei Pleckstrin homology domain-containing family G member 5 (Plekhg5)-assoziiertem MNE identifizieren.

Sod1 ist ein cytosolisches Protein ohne Signalsequenz für konventionelle Sekretion. Stattdessen wird die UPS über sekretorische Autophagie-Mechanismen reguliert. Unsere Ergebnisse zeigen, dass Plekhg5-Depletion in primären MN und NSC34-Zellen zu einer beeinträchtigten Sekretion von Wildtyp-Sod1 führt, was darauf hinweist, dass die UPS von Sod1 Plekgh5 abhängig ist. Indem verschiedene Schritte während der Biogenese von Autophagosomen gestört wurden, konnten wir nachweisen, dass die Plekhg5-regulierte Sod1-

Sekretion Autophagie abhängig ist. Um unsere Ergebnisse in einem klinisch relevanteren Modell zu analysieren, wurden humane iPSZ-MN von gesunden Spendern und ALS-Patienten mit S*OD1*-Mutationen untersucht. Hier fand sich, dass die Sekretion von mutiertem *SOD1* in ALS-MN im Vergleich zu gesunden und isogenen Kontrollen verringert ist. Dabei konnten wir zeigen, dass eine verringerte SOD1 Sekretion in ALS-MNs mit einer verringerten Expression von PLEKHG5 einhergeht. Um diese Korrelation zu bestätigen, wurden Kontroll-MN nach PLEKHG5-Depletion untersucht und eine verminderte SOD1-Sekretion dokumentiert, was auf eine PLEKHG5 Abhängigkeit hindeutet. Zusammenfassend konnten wir zeigen, dass Plekh5 die UPS von Sod1 in Maus MN und humanen MN reguliert und dass die Sod1-Sekretion Autophagie abhängig erfolgt. Unsere Daten belegen eine bislang noch nicht gezeigte mechanistische Verknüpfung zwischen zwei MNE-assoziierten Proteinen.

3 Introduction

3.1 The Neuromuscular junction (NMJ)

3.1.1 Functional organization of the NMJ

The NMJs is a highly specialized chemical synapse, which is crucial for the signal transduction between MNs and skeletal muscles. MNs transmit patterned electrical activity and convert this information via neurotransmitter to their target muscle and thereby trigger muscle movement. Complex movements, including breathing, walking, and fine motor skills require the conveyance of commands from MNs to serve the effector muscles in the periphery. Over the last decades the NMJ became the most investigated synapse in vertebrates (Sanes & Lichtman, 1999). The NMJ comprises three cellular components: The presynaptic nerve terminal of MNs, the postsynaptic membrane of skeletal muscle cells, and terminal Schwann cells (Figure 1) (Ogata, 1988).

The unique structure of NMJs comprises a high degree of complexity. The formation and maturation of pre- and postsynaptic compartments are tightly coordinated by shared molecular mechanisms. For its formation, upper MN (UMN) axons descending from the primary motor cortex travel through the central nervous system (CNS) and build glutamatergic connections with lower MNs (LMNs) in the brain stem and the anterior horn of the spinal cord. LMNs steer their axons through the peripheral nervous system (PNS) and terminate at muscles where they build presynaptic nerve terminals. The axons are myelinated by myelinating Schwann cells for the rapid propagation of action potentials. At their target site, MN axons profoundly ramify in thin axons to contact many muscle fibers. The thin ending of the MN axon terminates as boutons from where the neurotransmitter is released (Z. W. Hall & Sanes, 1993). These contact sites are highly specialized structures and are capped by terminal Schwann cells. Terminal Schwann cells function as protection layer and provide trophic support, for example by producing ciliary neurotrophic factor (CNTF), and thereby contribute to growth of the axon terminal, axon sprouting and NMJ formation and maturation (Alhindi et al., 2021; Darabid et al., 2014; Simon et al., 2010; Son et al., 1996).

The boutons contain numerous 50 nm diameter, membrane-bound synaptic vesicles (SVs) which in turn contain around 10.000 molecules of the neurotransmitter acetylcholine (ACh) (in mammals). The packing of SVs with neurotransmitter is referred as quanta. The SVs are enriched at so called active zones, which are sites of induced transmitter release (Figure 2). Upon MN activation the axon terminal depolarizes and opens voltage-gated calcium channels, resulting in an increase of the intracellular free calcium level. This triggers that SVs fuse with the plasma membrane and thereby ACh is released in the synaptic cleft between nerve and

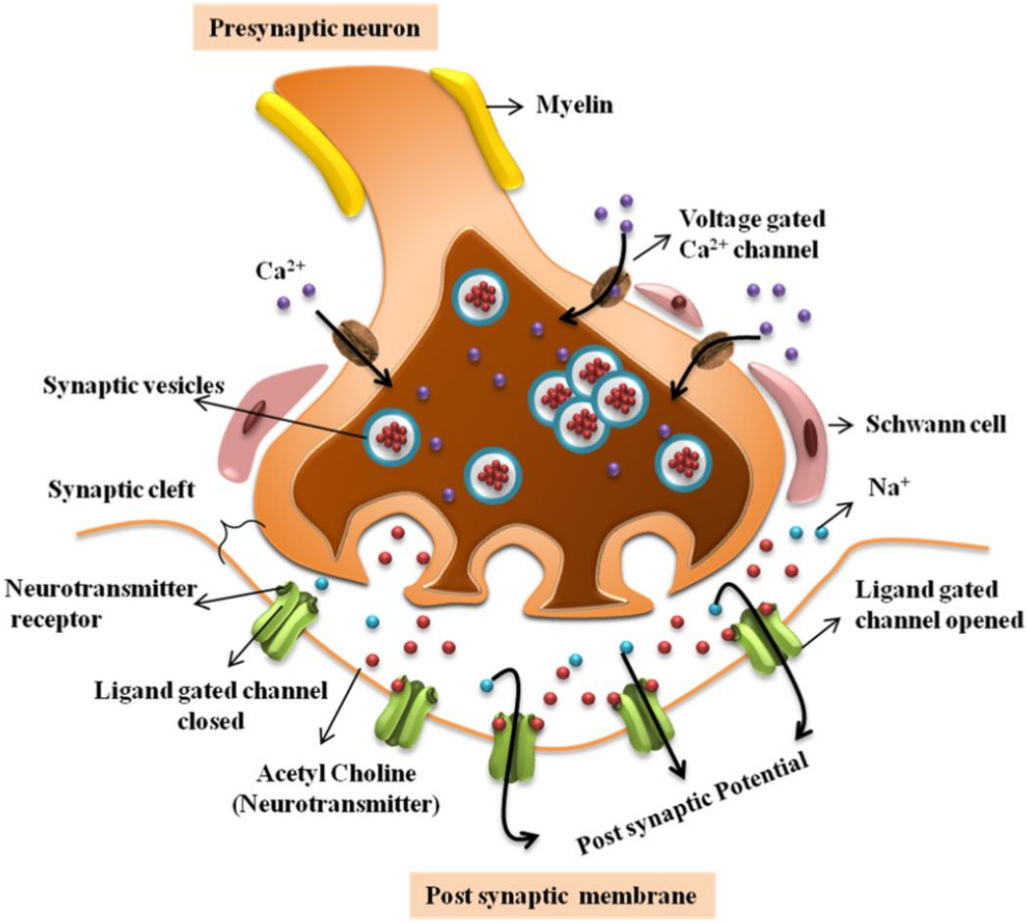

Figure 1: Schematic representation of the NMJ. The NMJ comprises three main compartments: The presynaptic nerve terminal of a MN, the postsynaptic membrane of skeletal muscle cells, and terminal Schwann cells. Depolarization of the nerve terminal opens voltage gated calcium channels and induces calcium influx and release of the neurotransmitter ACh into the synaptic cleft. ACh binds to its receptors (ligand gated channels) on the postsynaptic membrane, leading to muscle depolarization and muscle contraction. Adapted from (Natarajan et al., 2019) . Copyright © 2019 American Chemical Society.

muscle. Within the synaptic cleft is the basal lamina (BL), an extracellular matrix, which contains proteins like Laminin and Collagen, as well as key proteins like Agrin and Rapsyn,which play an important role in clustering and maintenance of postsynaptic ACh receptors (AChRs). Further, acetylcholinesterase (AChE) is bound to the BL, an enzyme which hydrolyses ACh for presynaptic reuptake (Hirsch, 2007; Naguib et al., 2002). Voltage-gated potassium channels and calcium-activated potassium channels in the presynaptic membrane take part in regulating and ending transmitter release. After reaching an intracellular calcium threshold, the channels open and potassium outflow repolarizes the membrane and limits further calcium entry (Hammond & Esclapez, 2015).

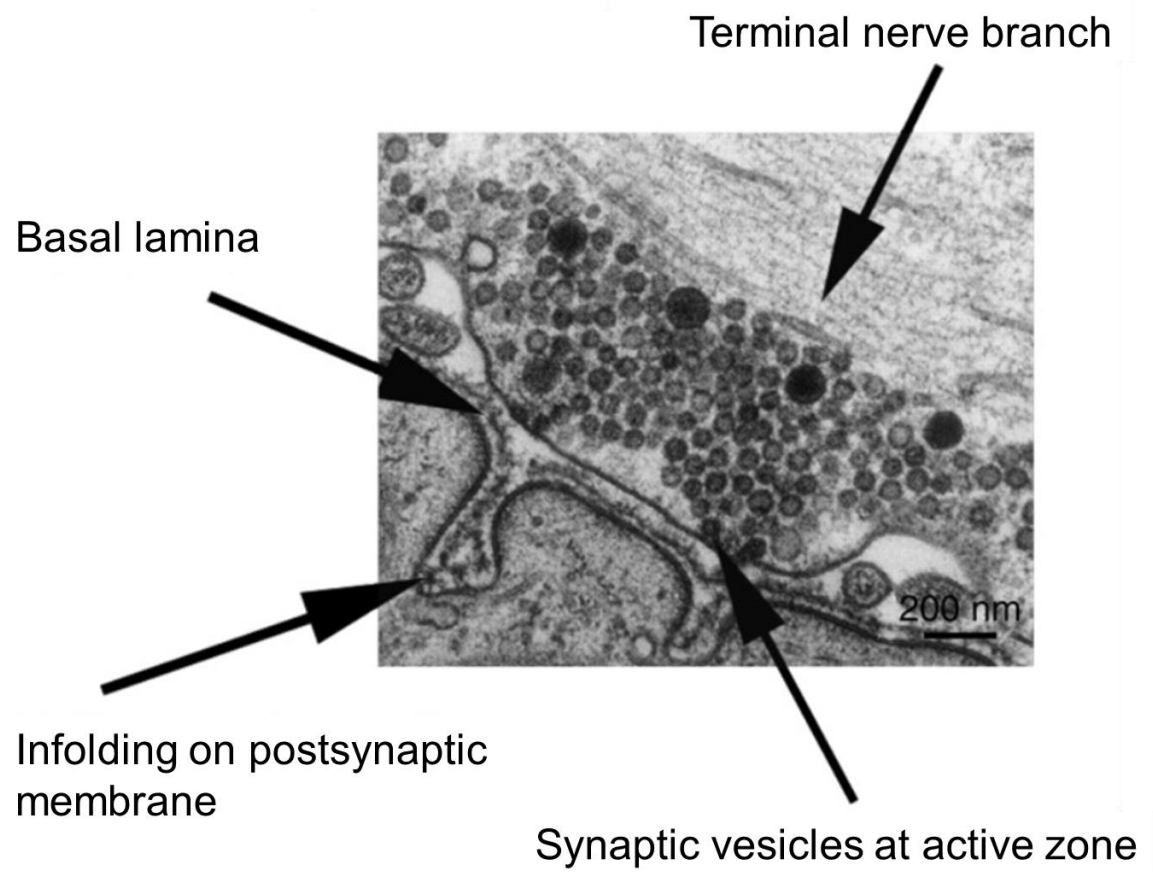

Figure 2: Transmission electron micrograph of the NMJ. Image shows a terminal nerve branch in close proximity to the basal lamina and the postsynaptic membrane with infoldings. Synaptic vesicles are enriched at the active zone. Adapted from (Hirsch, 2007).

On the postsynaptic muscle site, ACh binds to its AChR, a ligand-gated ion channel, allowing the transition of positive potassium ions into the muscle. AChRs cluster at 10.000 receptor/µm² and consist of 5 subunits (ααβδε) with two binding sites for ACh. After binding, the receptor undergoes formation changes and becomes ion permeable. Depolarization of the muscle cell consequently induces muscle fiber contraction.
Termination of ACh-induced depolarization occurs when ACh unbinds its receptor and is hydrolyzed by the AChE. The resulting choline molecule is up taken again in the nerve terminal and reused to synthesize new transmitters (Slater, 2017; Tintignac et al., 2015).

3.1.2 Development of the NMJ

The NMJ develops during embryogenesis in a series of steps that involve the exchange of signals among its three cellular components. Although it displays at timepoint of birth already an advanced and functional structure it undergoes several postnatal changes.

Muscle fibers derive from mesodermal cells that acquire a myogenic identity in the somites and then migrate to sites of muscle formation. There they divide, and their postmitotic progenitor cells differentiate into myoblasts. The myoblasts fuse into aligned, multinucleated myotubes, and later into myofibers, however muscle maturation is a protracted process. The contraction of myotubes initiates activation of numerous contractile and synaptic protein encoding genes. The expression of AChR subunit genes is upregulated during myotube fusion and subunits are translated, assembled, and inserted in the plasma membrane. During formation of nerve-muscle contact, diffusely distributed AChRs cluster in the postsynaptic membrane at the contact sites. Moreover, the post synapse matures into a complex apparatus and the membrane undergoes morphological changes. Most apparently, the membrane builds small invaginations which subsequently form to junction folds in colocalization to the presynaptic active zone.

The neural tube gives rise to the CNS which is composed of the brain and the spinal cord. Schwann cells derive from the neural crest, which arises from the dorsal margin of the neural tube. Schwann cells become associated with MN axons and follow axons through the periphery towards muscles. During this process, the axons provide migratory guidance and mitogenic stimulation for the Schwann cells. Myelinating Schwann cells and terminal Schwann cells derive from the same progenitors and mature postnatally (Castelnovo et al., 2017). Myelinating Schwann cells start the myelination of axons after birth. Terminal Schwann cells form in the beginning a loose cap over groups of axonal terminals, whereas in adults each terminal bouton is separately capped (Muppirala et al., 2021; Woodhoo et al., 2009).

MNs derive from multipotential progenitors from the neural tube and differentiate into UMNs and LMNs with distinct functions. UMNs mature in the primary motor cortex and terminate in the brainstem or spinal cord, restricting them to the CNS. They transmit information from the brain to the LMNs via glutamatergic connections. LMNs are efferent neurons that connect the CNS with the muscle to be innervated. They mature in the brain stem and the anterior horn of the spinal cord and extend their axons through the PNS. The axons transit through different tissues and terminate at their specific muscle target where they build cholinergic connections and thereby regulate the contraction of skeletal muscles and thus control movement (Hammond & Esclapez, 2015; Sanes & Lichtman, 1999).

Axonal targeting of muscle cells displays a critical process of MN development. To find their muscle target, MNs must pass several “checkpoints” and use intrinsic mechanisms to orientate along the axonal route. To connect with the muscle, axonal targeting relies on signals which are received at the growth cone, and which induce molecular and anatomical modifications (Hammond & Esclapez, 2015; Stifani, 2014). Axons contact myotubes near their sites of entry into the muscle. Axon terminals branch numerous times intramuscularly to innervate up to hundreds of muscle fibers and thereby build the first NMJs. In the beginning, newly formed

axon terminals are simple bulbous enlargements which bear only few synaptic vesicles. Subsequently, the synaptic topography matures accompanied by an increase in synaptic volume, increase in synaptic vesicle number, active zone formation and spontaneous exocytosis.

During the first few postnatal weeks the mammalian NMJ undergoes remarkable changes in structure and its molecular architecture. The best studied molecular change is the conversion of AChRs from an embryonic to an adult form. AChRs of the embryonic vertebrate muscles are pentamers composed of five membrane-spanning subunits: two alpha-, one beta-, one delta- and one gamma subunit. During the first 2 weeks after birth, AChRs containing a gamma subunit are replaced by AChRs with an epsilon subunit which is caused by a downregulation of the gamma gene and upregulation of the epsilon gene. Although the factors that initiate the switch between the subunits are not completely understood, the role of the neuronal input has been the focus of investigation (Martinou & Merlie, 1991; Missias et al., 1996; Numberger et al., 1991). It is also assumed, that the switch is linked to a maturational program in muscle cells and that the functional importance lies in the different kinetics of the gamma subunit and epsilon subunit (Brehm & Henderson, 1988; Schuetze & Role, 2003).
Furthermore, the innervation structure of the vertebrate NMJ changes remarkably during the first postnatal weeks. At birth, muscle fibers are innervated by several nerve terminals originating from distinct MN. Postnatally, these nerve terminals undergo an activity-dependent competition and all inputs, but one is withdrawn in a synapse elimination process. This eventually results in each NMJ being innervated by a single axon capped by terminal Schwann cells and that the size of the endplate and the numbers of AChRs, junctional folds, and active zones increase during this period (Sanes & Lichtman, 1999; Stifani, 2014).

3.1.3 The human NMJ

Although the principal organization of vertebrate/mammalian NMJs share important features, there are considerable inter-species differences in the NMJ morphology.
Compared to other vertebrate species, human NMJs are with an average size of 15 nm the smallest known and consistently have small vesicle quanta. However, human muscle fibers have large diameters, and the postsynaptic membrane has among other species extensive and deep infoldings which increase the local surface (Slater, 2017). A systematic comparative analysis between mouse and human NMJs revealed differences in morphology, distinct synaptic proteomes, and distinct localization of active zone proteins such as SNAP-25. Although human NMJs were typically only half the size of mouse NMJs, with axon diameters only a third of the size, they were found to innervate muscle fibers that were up to twice the diameter of those in mice (Jones et al., 2017).

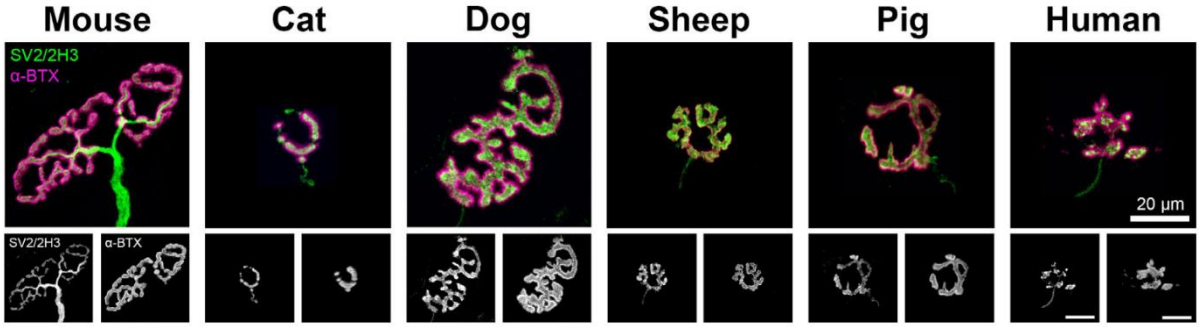

Figure 3: Heterogenity in mammalian NMJ morphology. Representative confocal images of mammalian NMJs shows distinct morphological differences between mouse and human NMJs, while sheep and pig NMJs display morphological similarities. α-bungarotoxin = acetylcholine receptors (magenta); SV2/2H3 = synaptic vesicle and neurofilament (green). Adapted from (Boehm et al., 2020).

The significant heterogeneity in NMJ morphology raises questions about the extent to which NMJ form and function in one species can be applied to another species. While there are certainly many aspects of NMJ form and function that have been successfully replicated across species, it is possible that responses to degenerative or disease stimuli could elicit distinct species-specific responses at the NMJ. This may contribute to the difficulty in translating studies of NMJ-related diseases in mouse models to human patients, such as in MNDs like ALS. Interestingly, a comparative study by Boehm et al. showed that pig and sheep NMJs more closely resemble human NMJs than rodent NMJs do, which could imply that the utilization of large animal models may be more appropriate and accurate for understanding human NMJs in health and disease (Figure 3) (Boehm et al., 2020) . However, this may only be one aspect of the many factors affecting the poor therapeutic translation of potential drugs, for example for ALS, in clinical trials (Perrin, 2014).

3.2 Motor neuron diseases (MNDs)

Neurodegenerative diseases are a diverse group of neurological conditions characterized by the irreversible loss of neurons in the central or peripheral nervous system. They can be divided into two categories: MNDs primarily affecting muscle movement, and cognitive impairments involving the cerebral cortex (Lamptey et al., 2022; Wilson et al., 2023).
MNDs encompass a variety of clinically and genetically heterogeneous disorders, which lead to the degeneration of MNs. Due to the high degree of genetic heterogeneity among these diseases, a common disease mechanism has not been identified so far. However, alterations in autophagy appear to play a central role in the disease process of various motor neuron disorders and therefore might provide a potential target for therapeutic development (Kang et

al., 2019; Lüningschrör et al., 2017; Porras et al., 2018; Ramesh & Pandey, 2017; Rodríguez-Muela, 2020).

Based on clinical criteria, two main forms of MNDs can be distinguished: ALS in adults and spinal muscular atrophy (SMA) in children and young adults. SMA affects only the lower MNs and is the predominant form of MND in children and young adults (Jablonka & Sendtner, 2017). The most common cause of SMA is associated to a deletion or mutation of the survival of motor neuron (*SMN1*) gene (Wee et al., 2010). Over 95% of the total cases of SMA are associated to *SMN1* gene mutation, located on chromosome 5q, in the 5q13.2 locus, and therefore referred to as 5q SMA, while the rest of about 4-5% of the SMA cases, referred to as non-5q SMA, are genetically heterogeneous and clinically diverse (Darras, 2011; Shelby & Mirea, 2021). Non-5q SMA also overlaps clinically with the MN affecting disorders Charcot-Marie-Tooth disease (CMT) and distal hereditary motor neuropathy (dHMN). More than 80 genes were identified to cause CMT neuropathies and based on clinical findings CMT is mainly associated to defects of the Schwann cells resulting in abnormal myelination (CMT1) or to neuronal defects resulting in nerve axon damage (CMT2) (Bienfait et al., 2006). Most types of CMT typically manifest during childhood or adolescence, although the age of onset can vary from infancy to late adulthood. CMT is characterized by a symmetric, gradually advancing distal motor neuropathy affecting the arms and legs. Typically, it emerges between the first and third decades of life, leading to muscle weakness and wasting in the feet and/or hands (Bird, 2023; Stavrou et al., 2023; Stojkovic, 2016). dHMN disorders primarily affect MNs and are characterized by weakness in the distal lower MNs. Unlike CMT, where sensory involvement is a significant component of the disease, dHMN primarily affects the MNs and is characterized by weakness in the distal lower MNs. However, some forms of dHMN exhibit minor sensory abnormalities, showing an overlap between the axonal forms of CMT 2 and dHMN, where the same mutation in a gene can cause both phenotypes (Landrieu et al., 2013).

In ALS, the upper MNs and lower MNs are affected, leading to progressive muscle weakness and muscle atrophy, and partly leading to cognitive impairments. The onset of symptoms is usually between the ages of 50 and 65 years, however there are also juvenile forms of ALS. Most patients die from respiratory muscle failure 2-5 years after the onset of the disease (Yamashita & Ando, 2015; Zarei et al., 2015). In contrast to SMA, several genes are associated with ALS. About 90% of ALS cases occur sporadically (sALS), with no prior family history of ALS, and approximately 10% of the ALS cases are considered as familial ALS (fALS), usually inherited as dominant traits. In Europe, *C9orf72* is the most common gene associated with fALS, however, 17 different definitive gene defects have been identified in fALS (https://alsod.ac.uk/, accessed on 05 June 2023), indicating a high degree of genetic and pathomechanistic heterogeneity (Figure 4) (Brenner & Weishaupt, 2019; DeJesus-Hernandez

et al., 2011; G. Kim et al., 2020; Renton et al., 2011; Suzuki et al., 2022; Zou et al., 2017). While a therapy for SMA in the form of the drugs Spinraza/Nusinersen and Zolgensma has been successfully developed in recent years (Mercuri et al., 2018), there is currently no cure for ALS (Jerath & Shy, 2015; Kumar Jaiswal & Jaiswal, 2019). Two drugs, Riluzole and Edaravone, are available as therapies for ALS, both of which only slow the progression of the disease but do not stop or cure it. The exact mechanism of action for both drugs is not fully understood. Riluzole is believed to act as a glutamate antagonist and prevent neuronal hyperexcitability. Edaravone binds hydrogen peroxide and protects cells from oxidative stress (Jami et al., 2015; Mejzini et al., 2019).

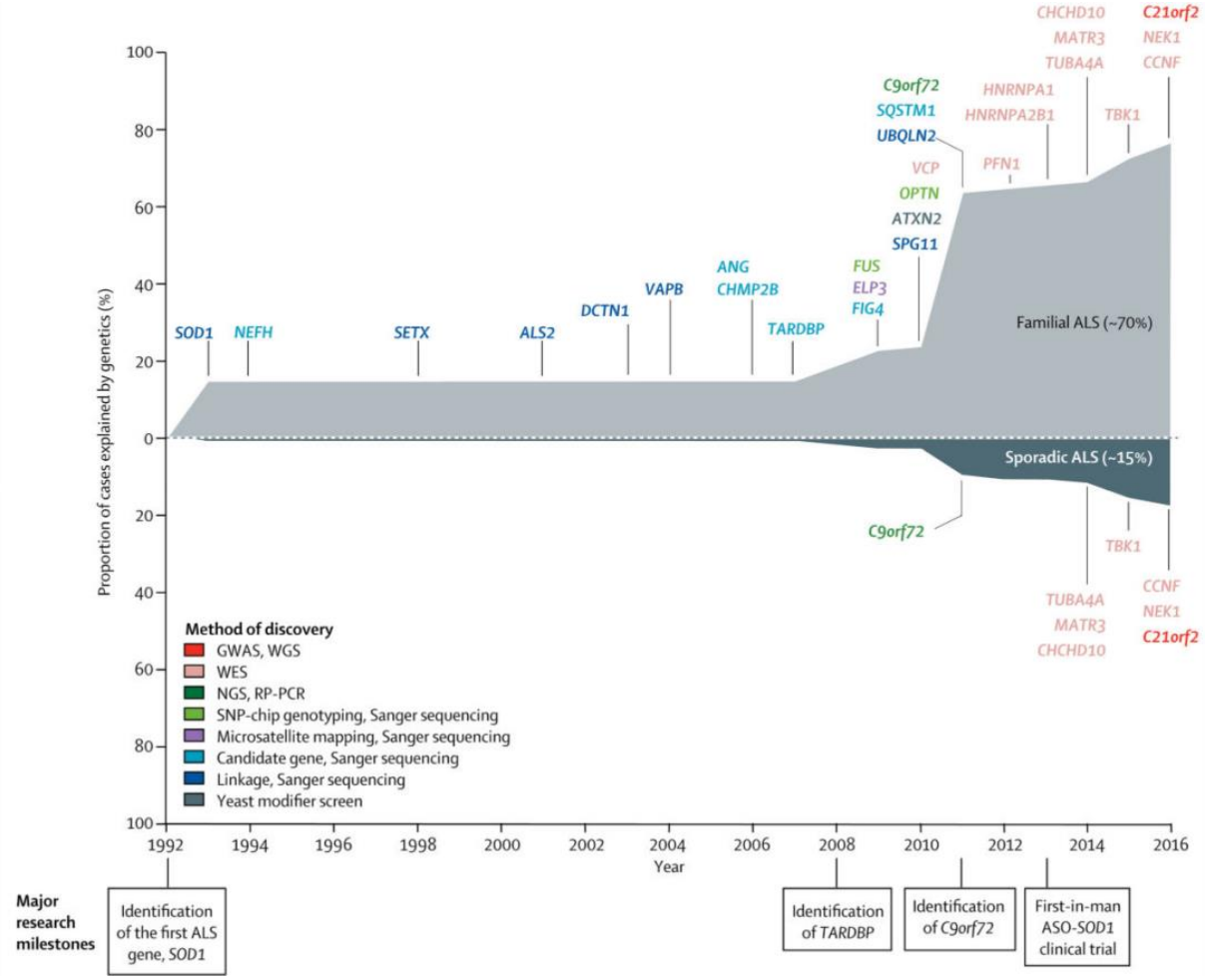

Figure 4: Discovery of ALS-associated genes from 1992 to 2016. The y-axis shows the gene variant prevalence in fALS and sALS in percentage. The x-axis represents the year of gene discovery. Adapted from (Chia et al., 2018).

3.2.1 The role of SOD1 in ALS

In 1993, copper-zinc *SOD1* was identified as the first gene associated with ALS (Deng et al., 1993; Rosen et al., 1993). SOD1 is a metalloenzyme that binds to copper and zinc, forming a highly stable homodimer. SOD1 dimers are present in the cytosol and intermembrane space

of mitochondria, serving as a crucial antioxidant defense mechanism. They catalyze the conversion of toxic superoxide species, generated during cellular respiration, into oxygen and hydrogen peroxide (McCord & Fridovich, 1969). In Europe, pathogenic variants in *SOD1* are responsible for approximately 15% of fALS cases and 1%-2% of sALS cases (Figure 5) (Mejzini et al., 2019; Zou et al., 2017). Over 200 disease-associated variations in *SOD1* have been identified, distributed throughout the gene (https://alsod.ac.uk/, accessed on 05 June 2023). The most common mutations found in the *SOD1* gene are the D90A (aspartic acid at codon 90 changed to alanine) and the A4V (alanine at codon 4 changed to valine) mutations, mainly occurring in Europe and North America, respectively (Andersen, 2006; Andersen et al., 1995; Pansarasa et al., 2018; Valentine & Hart, 2003). The phenotype, disease duration, and severity can vary significantly depending on the specific variants involved. For example, the A4V variant is associated with a limb-onset, aggressive form of ALS. Patients with the D90A mutation typically display slowly progressive paresis starting in the legs and gradually spreading upward (Mejzini et al., 2019).

Figure 5: ALS-associated genes in populations of European and Asian ancestry. In European populations *SOD1* mutations account for 14,8% in fALS and 1,2% in sALS. In Asian populations the proportion for *SOD1* in fALS is twice as high (30%). Adapted from (Mejzini et al., 2019).

Although the *SOD1*-linked pathophysiological mechanisms are not fully understood yet, there are several distinct neuropathological hallmarks, with major indication for neurotoxicity (Ferraiuolo et al., 2011; Hayashi et al., 2016; Kaur et al., 2016; Peggion et al., 2022). The most commonly mouse model used in this research is the transgenic *SOD1*^{G93A} model. These mice overexpress mutant *SOD1* and show a late-onset disease progression resulting in impaired motor function and loss of MNs (Gurney et al., 1994). Several studies with *SOD1*^{G93A} mice and other transgenic *SOD1* models showed that *SOD1* mutations are linked excitotoxicity (Tortarolo et al., 2006), oxidative stress (An et al., 2014), endoplasmic reticulum stress (Nishitoh et al., 2008), mitochondrial dysfunction (Cassina et al., 2008) and axonopathy (Fischer et al., 2004). Further, SOD1 protein inclusions were found in MNs of transgenic *SOD1* models misfolding (Marino et al., 2015), and in MNs of patients with fALS and sALS (Bosco et al., 2010; Rakhit et al., 2007). As discussed earlier, protein inclusions and aggregations, for example caused by altered autophagy homeostasis, can result in toxicity (Ramesh & Pandey, 2017) and might be one reason for the described ALS pathology and specifically for MN loss. The exact pathophysiological cascade which leads to the loss of motor functions is still under debate. Studies with *SOD1*^{G93A} mice provided evidence for the dying-back hypothesis, which proposes that ALS pathology is initiated at the distal axon terminals of the lower MNs and advances in a retrograde direction from the NMJ to the CNS (Fischer et al., 2004). Consequently, NMJs become an early and vulnerable target in ALS, representing the starting point of the pathological cascade leading to muscle atrophy and MN loss (Carrasco et al., 2010; Fischer et al., 2004; Murray et al., 2010; Piotrkiewicz & Hausmanowa-Petrusewicz, 2013).

3.2.2 The role of PLEKHG5 in lower MND

PLEKHG5 is a guanine exchange factor (GEF) which is highly expressed in the nervous system (Marx et al., 2005). Plekhg5 regulates the autophagy of SVs by activating Rab26, a small GTPase, enriched on SVs (Binotti et al., 2015; Lüningschrör et al., 2017). Different mutations in the human *PLEKHG5* gene have been linked to various forms of MNDs (Azzedine et al., 2013; Chen et al., 2021; Gonzalez-Quereda et al., 2021; H. J. Kim et al., 2013; Maystadt et al., 2007; Özoğuz et al., 2015; Senderek, 2021).

In an initially studied African family with a unique form of autosomal recessive lower MND (distal spinal muscular atrophy, DSMA4), characterized by childhood onset, widespread muscle involvement, and severe outcome, a single homozygous missense mutation in the

PLEKHG5 gene was identified (Maystadt et al., 2007). Subsequently, additional *PLEKHG5* mutations have been observed in patients with autosomal recessive intermediate CMT disease, DSMA, and dHMN (Chen et al., 2021; Gonzalez-Quereda et al., 2021; Senderek, 2021). Furthermore, a *PLEKHG5* gene mutation was found in a screening approach of patients suffering from ALS and a variant in the *PLEKHG5* gene has been identified as a disease modifier in a family with *TARDBP*-linked ALS, characterized by an early onset and rapid disease progression (Goldstein et al., 2020). These findings highlight the crucial role of *PLEKHG5* in maintaining the integrity and function of MNs and the PNS. Studies with *Plekhg5*-deficient mice show impaired autophagy-mediated clearance of SVs in axon terminals of MNs in the spinal cord, resulting in large accumulations of SVs and swollen axon terminals at NMJs. These mice develop a MND pathology displaying hindlimb clasping, reduced grip strengths and reduced rotarod performance. However, beyond its involvement in SV autophagy, limited knowledge exists regarding the specific function of Plekhg5.

3.3 NMJ and MND models

3.3.1 Potential and limitations of animal models in MND

In human MNDs the NMJ is an early and vulnerable target. In order to understand human disease biology, research relies on model organisms for insight. Animal studies, for example with *Plekhg5*-deficient mice, recently revealed an unknown pathological pathway in MND and are crucial for continuously improving our understanding of pathological mechanisms in MNDs (Lüningschrör et al., 2017). Further, they play a central role in the development of new therapies, as in the case of SMA. However, effective therapies for ALS and other MNDs have not yet been developed. Many findings obtained from mouse models could not be validated in clinical studies, raising concerns about their relevance and utility as predictive models in preclinical research (Bart van der Worp et al., 2010; McGonigle & Ruggeri, 2014; Perrin, 2014). Studies using the well-characterized *SOD1*^{G93A} transgenic mouse model, have led to the discovery of compounds that counteract the disease in mouse models. However, these compounds have not shown efficacy in clinical trials (McGonigle & Ruggeri, 2014; Perrin, 2014). The reason why ALS mouse models inadequately phenocopy the disease is unclear. As discussed earlier, one reason might be significant differences in the morphology and molecular composition of the NMJ between mice and humans (Boehm et al., 2020; Jones et al., 2017). From these differences unique physiological properties arise, which need to be considered when studying pathological processes affecting the NMJ. In *SOD1*^{G93A} mice, human *SOD1*^{G93A} is overexpressed, resulting in mutant protein at non-physiological levels. Studied aspects of the disease in this model may be partly not relevant for human. Therefore,

new disease models based on human cells are necessary, ideally reflecting the physiological and morphological aspects of human NMJs *in vitro*.

3.3.2 Human iPSCs for MND modeling

Human iPSC-based techniques provide a promising approach to directly address these challenges by using human disease-relevant cell culture models. Somatic cells from patients and healthy donors can be reprogrammed to a pluripotent state by the exogenous addition of the four transcription factors, *Oct4*, *Sox2*, *c-Myc*, and *Klf4* (Takahashi et al., 2007; Takahashi & Yamanaka, 2006). These iPSCs inherit the ability to differentiate into any of the three embryonic germ layers: Ectoderm, mesoderm, and endoderm (Hanna et al., 2010). Patient-derived iPSCs carrying disease-relevant mutations at physiological levels are a powerful tool to analyze diseases adequately. Over the past decade, researchers have developed methods with increasing efficiency to differentiate iPSCs toward specific cellular lineages, including MNs, via addition of morphogens, small molecules, or expression of lineage-specific transcription factors (Du et al., 2015; Maury et al., 2014; Reinhardt et al., 2013; Shi et al., 2017).

The application of iPSC derived MNs in disease models ideally requires their integration into complex and functional networks. Over the last decades, progress was made towards engineering and analyzing complex 3D NMJ- and MND models *in vitro.* This was accomplished by the development of specialized tissue engineering methods, resulting in co-cultures, assembloids or organoids (de Jongh et al., 2021; Natarajan et al., 2019). Initial studies with ALS-patient derived MNs primarily focused solely on MNs as a tool for disease modeling, drug screening, and RNA sequencing (Donnelly et al., 2013; Egawa et al., 2012; Fujimori et al., 2018). However, although iPSC derived MNs show the characteristic morphology and exhibit spontaneous activity (Devlin et al., 2015; Giovanni & Sheng, 2015; Schenke et al., 2020; Wainger et al., 2014), studies have shown that MNs in monocultures do not fully mature *in vitro* (Arbab et al., 2014; Ho et al., 2016; Schenke et al., 2020). Complete maturation of MNs requires the synaptic connection with muscle cells as an innervating target to establish functional activity (Natarajan et al., 2019; Sances et al., 2016). Further, NMJs play a central role in MNDs, thus, for the analysis of MNDs like ALS, a functional NMJ with a pre- and postsynaptic structures is essential. Therefore, human co-culture systems with MNs and muscle cells are progressing as a powerful tool to generate mature MNs and to recapitulate a more realistic NMJ physiology.

3.3.3 Human iPSC-based co-culture systems

First studies with neuromuscular 2D co-culture systems utilized rodent or other inter-species spinal cord and muscle explants (Bornstein & Breitbart, 1964; Crain & Peterson, 1964; Peterson & Crain, 1970). Advances in human iPSC differentiation initiated 2D co-culture approaches with human MNs and human muscle. Human iPSC MNs have been co-cultured with primary human skeletal muscle cells (Afshar Bakooshli et al., 2019; Santhanam et al., 2018; Steinbeck et al., 2016) or with human iPSC derived skeletal muscle cells (Figure 6) (Demestre et al., 2015; Puttonen et al., 2015). In 2016, Steinbeck et al. reported for the first time a 2D co-culture system under optogenetic control by using transduced MNs with a light-sensitive ion channel which enabled blue-light induced contraction of muscle cells, and which could be used as a model for the autoimmune disorder Myasthenia gravis (Steinbeck et al., 2016). These studies demonstrated that neuromuscular 2D co-cultures form synaptic contacts, exhibit electrophysiological activity, and control the contraction of myotubes. However, the complexity of a 3D biological environment cannot be fully recapitulated in these models. This is especially true for the muscle strand physiology. A 3D environment *in vitro* supports the maturation and alignment of myotubes, increases the expression and clustering of AChR, the upregulation of muscle markers such as myosin heavy chain, and spontaneous electrical activity accompanied by twitching. Further, 3D muscle tissues show an increase in muscle fiber diameter over time (Afshar Bakooshli et al., 2019; Natarajan et al., 2019; Smith et al., 2016). Therefore, the establishment of 3D cultures has opened a more sophisticated approach to elucidate NMJs and the pathogenesis of MNDs like ALS. By utilizing ALS-patient derived cells in 3D neuromuscular co-cultures, studies could show that MNs reproduce pathological phenotypes, including increased axonal varicosities, increased excitability, and reduced axonal branching. Analyzed NMJs displayed quality deficits, resulting in poor muscle innervation and muscle contraction (Guo et al., 2010; Stoklund Dittlau et al., 2021). Further studies could provide ALS models to test potential therapy strategies and drug screening approaches (Osaki et al., 2018, 2020; Stoklund Dittlau et al., 2021). However, until today only few 3D co-cultures based on ALS patient derived iPSCs were reported.

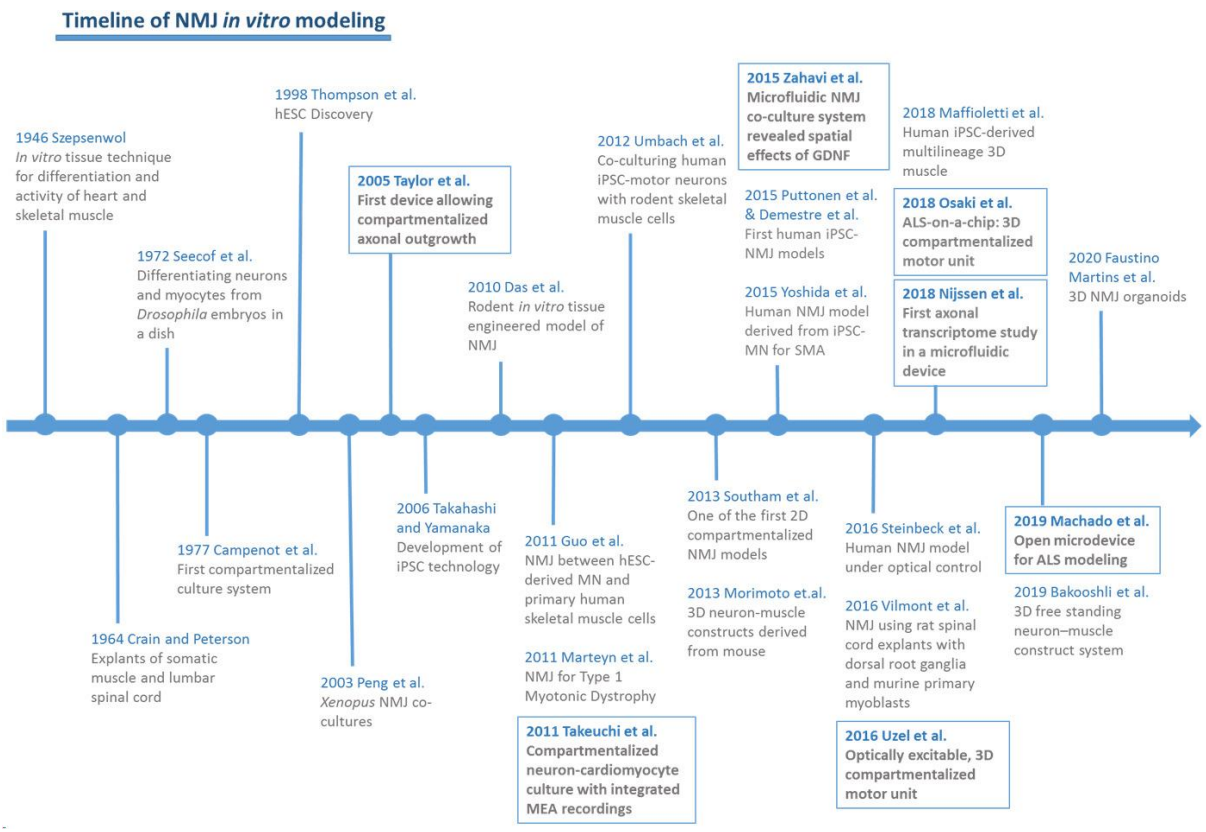

Figure 6: Timeline of NMJ *in vitro* modeling. Timeline showing advances and highlights (blue frames) of in vitro studies in chronological order. Adopted from (de Jongh et al., 2021).

Despite significant progress in differentiating human iPSCs into MNs (Du et al., 2015; Maury et al., 2014; Reinhardt et al., 2013) and establishing responsive human muscle fibers *in vitro* (Madden, 2002), the first studies on human NMJ models, whether in 2D co-cultures (Guo et al., 2020; Santhanam et al., 2018; Steinbeck et al., 2016) or 3D co-cultures (Maffioletti et al., 2018; Osaki et al., 2018) did not demonstrate mature NMJ formation through the gamma to epsilon AChR subunit switch. In 2019 Afshar Bakooshli et al. reported for the first time a human 3D co-culture model that expresses the mature postsynaptic AChR with epsilon subunits, approaching a mature NMJ to some extent. This system was used to model and analyze disease mechanisms in Myasthenia gravis though (Afshar Bakooshli et al., 2019). Based on this protocol, a 3D co-culture system for modeling ALS with mature NMJs was adapted using different iPSC derived MN lines from ALS patients with *SOD1* mutation and primary human skeletal myoblast. Utilizing this system, ALS co-cultures were able to recapitulate aspects of the human ALS pathology, displaying distinct axonal degradation and hampered muscle contraction over time (Massih et al., 2023).

There are still open questions about *in vitro* NMJ engineering, maturation, maintenance, and degradation which are of high importance, especially for understanding pathological

mechanisms in NMJ-associated diseases. Untill today, co-culture systems for disease modeling have not fully exploited their potential. The integration of human Schwann cells in neuromuscular co-cultures, for example, is not described yet. Furthermore, long culturing periods and its effect on NMJ morphology, and the generation of co-cultures derived from the same pool of iPSCs are interesting future perspectives which need to be further investigated.

3.4 Autophagy

Autophagy is a catabolic process in which damaged or unused cellular components are degraded and recycled, serving as a regulatory mechanism for maintaining homeostasis in cells, tissues, and organisms. There are three distinct autophagic pathways: macroautophagy, microautophagy, and chaperone-mediated autophagy (Boya et al., 2013; Mizushima et al., 2011). The following paragraph focuses on the molecular machinery required for macroautophagy, hereafter termed autophagy.

While originally believed to be a non-specific cellular degradation process, it is now known that autophagy includes various specialized forms that selectively degrade specific targets, such as organelles like mitochondria (mitophagy) or ribosomes (ribophagy) (Kiel, 2010), synaptic vesicles (Binotti et al., 2015; Birdsall & Waites, 2019; Gundelfinger et al., 2022), and even intracellular pathogens (xenophagy) (Sharma et al., 2018). During autophagy, cytoplasmic materials destined for degradation are sequestered within a double-membrane structure called the autophagosome. The autophagosome then fuses with a lysosome for the proteolytic digestion of the cargo materials, including damaged proteins or organelles. Upon amino acid starvation, mammalian target of rapamycin complex 1 (mTORC1) becomes inactivated, which leads to the induction of autophagy and increased autophagosome formation. The biogenesis of autophagosomes is initiated at the isolation membrane (phagophore), followed by the coordinated action of autophagy-related (ATG) proteins and protein complexes, including Microtubule-associated protein 1A/1B-light chain 3 (LC3-I) (Lamb et al., 2013; Mizushima, 2007; Mizushima et al., 2011). LC3-I is conjugated to phosphatidylethanolamine to form LC3-LC3-II, which is recruited to the phagophore and plays a role in autophagosome biogenesis and recognition of distinct sets of cargoes for selective autophagy (Tanida et al., 2008). Moreover, the expansion of the phagophore membrane relies on vesicular transport from several cellular compartments, including the ER–Golgi intermediate compartment, the Golgi and recycling endosomes. In the next step, autophagosomes fuse with lysosomes which generates autolysosomes. The inner membrane and the cargo of the autophagosome are degraded by lysosomal/vacuolar hydrolases and released into the cytoplasm for cellular recycling processes (Figure 7) (Lamb et al., 2013).

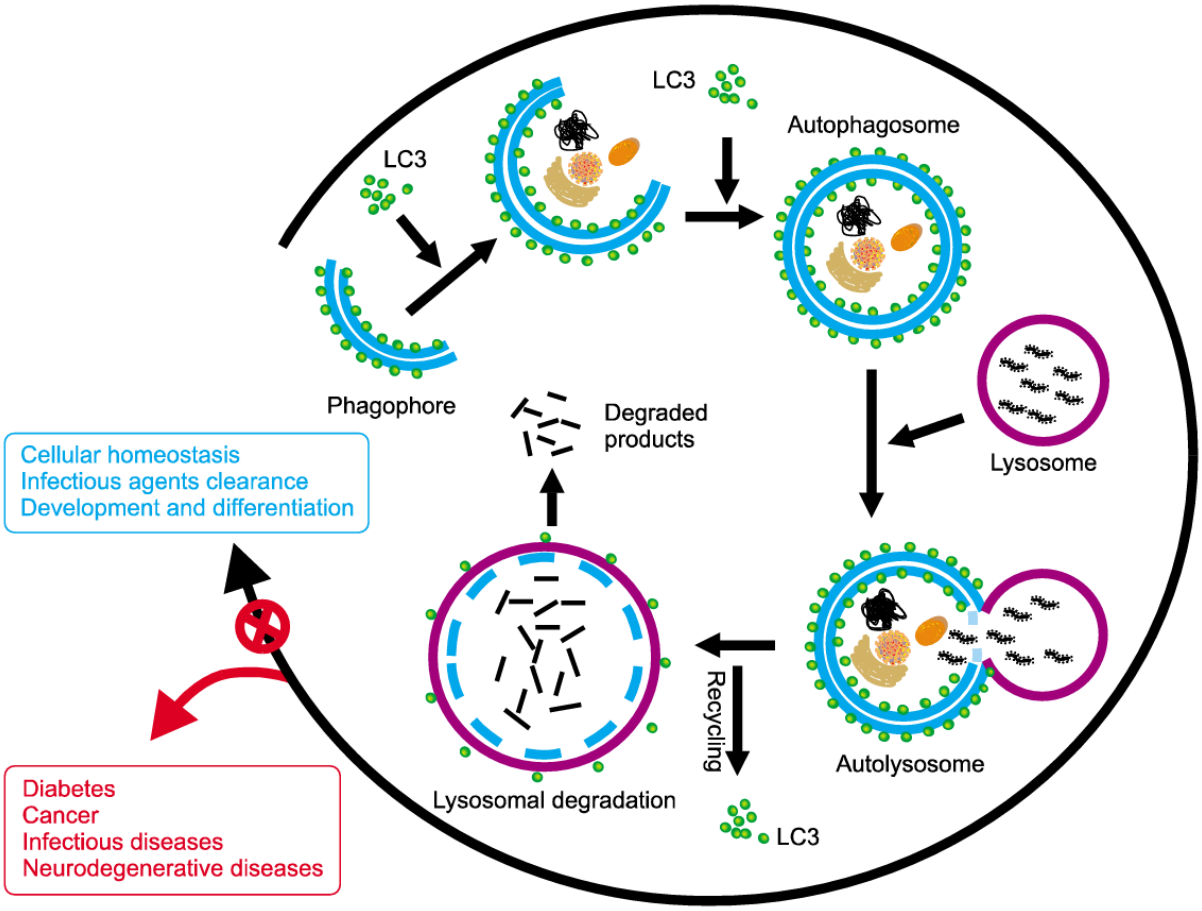

Figure 7: Schematic diagram of autophagy processes. Autophagy maintains cellular homeostasis by degrading damaged and unused proteins and organelles, while dysfunctional autophagy is associated with various diseases. During phagophore elongation LC3 is recruited to the membrane. The phagophore membrane engulfs cargo, building an autophagosome. Autophagosomes fuse with lysosomes for lysosomal cargo degradation. Adapted from (Jing & Lim, 2012).

3.4.1 Secretory Autophagy

In addition to its role in targeting proteins for lysosomal degradation, the autophagy machinery has been implicated in cellular secretion pathways, known as secretory autophagy. Autophagosomes fuse with the plasma membrane and thereby release the cargo into the extracellular space (Figure 8). Secretory autophagy enables the unconventional secretion of cytosolic cargo, including cytosolic proteins that lack N-terminal signal “leader” peptides. Unlike proteins with leader peptides, which can enter the conventional secretory pathway through the endoplasmic reticulum and Golgi apparatus, these cytosolic proteins require an alternative route for secretion. Secretory autophagy can serve as a release mechanism of such cargo by bypassing the conventional secretory pathway (Cavalli & Cenci, 2020; J. Kim et al., 2018; New & Thomas, 2019; Ponpuak et al., 2015; Rabouille et al., 2012). The connection between secretory autophagy and unconventional secretion was initially observed in yeast, where

specific ATG proteins were found to be required for the extracellular release of the acyl-CoA-binding protein Acb1 (Duran et al., 2010; Manjithaya et al., 2010) . Subsequent studies extended this functional link to mammalian systems and identified a diverse range of targets that are released via autophagy-dependent unconventional secretion. These include pro-inflammatory molecules such as IL-1β and IL-18 (Dupont et al., 2011), but also aggregate-prone proteins which are linked to neuronal diseases such as amyloid beta and hyperphosphorylated tau in Alzheimer's disease, mutant *huntingtin* in Huntington's disease, and *SOD1* and *TDP43* in ALS (Burbidge et al., 2022; Cruz-Garcia et al., 2017; Iguchi et al., 2016; Kang et al., 2019; Nilsson et al., 2013; Trajkovic et al., 2017). It is hypothesized that the secretion of these (toxic) protein aggregates might play an important role in prion-like propagation, disease progression and cell death (Ejlerskov et al., 2013; Sproviero et al., 2018). However, the molecular mechanisms and the disease relevance of UPS and secretory autophagy are not yet fully understood.

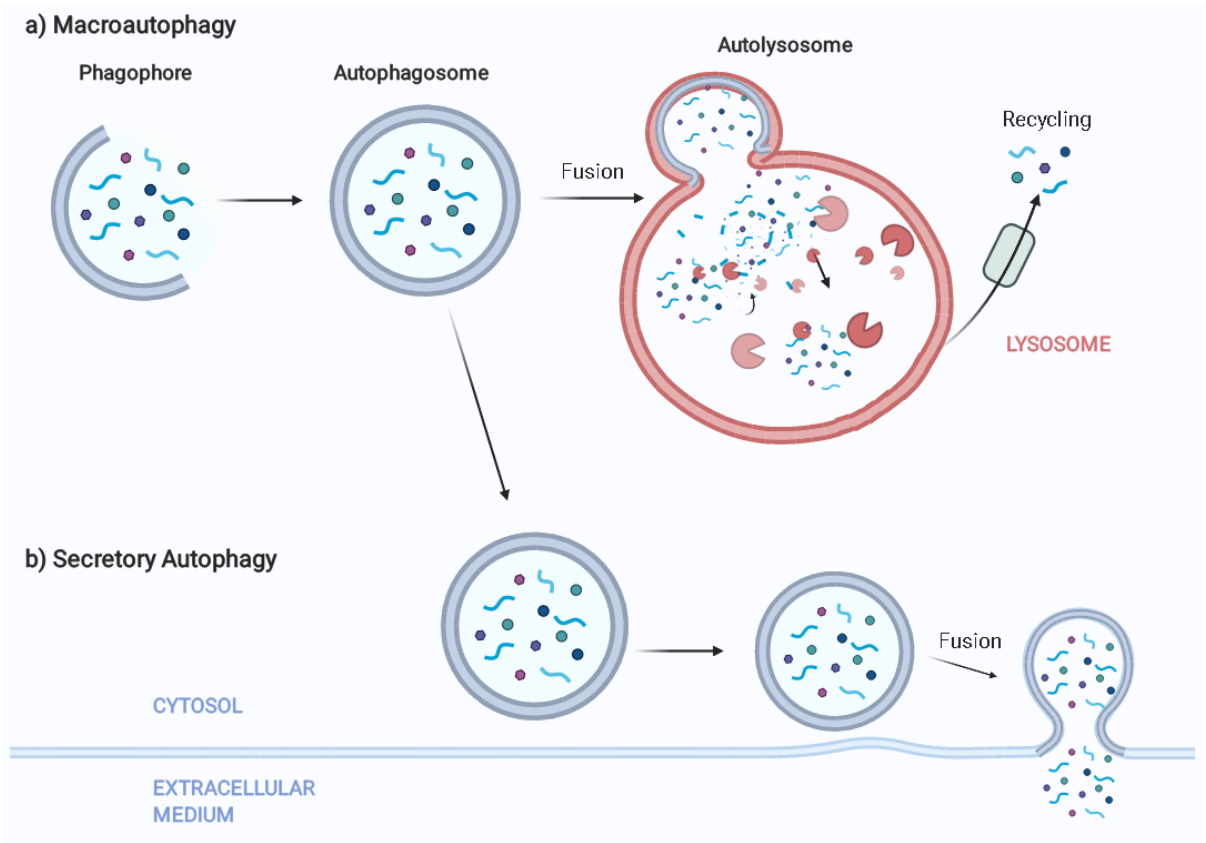

Figure 8: Schematic diagram of macroautophagy and secretory autophagy pathways. a) During macroautophagy, autophagosomes fuse with lysosomes for cargo degradation and recycling. b) In secretory autophagy processes, autophagosomes fuse with the cell membrane and release the cargo into the extracellular medium. Adapted from "Three Main Types of Autophagy", by BioRender.com (2021). Retrieved from https://app.biorender.com/biorender-templates.

3.4.2 Autophagy in neurodegenerative diseases

Dysregulation of autophagy has been closely associated with various diseases, including neurological disorders (Frake et al., 2015; Klionsky et al., 2021; Menzies et al., 2015, 2017).
In cultured neurons, the majority of autophagosomes are formed in the distal axon region, particularly in the vicinity of the presynaptic active zone and are retrogradely transported to the soma for autolysosomal degradation (Hollenbeck, 1993; Wang et al., 2015). The cargo degradation and biogenesis of axonal autophagosomes occur in a manner similar to non-neuronal cells, involving the ordered recruitment of ATG proteins and protein complexes (Maday et al., 2014; Maday & Holzbaur, 2014). Studies in mice have shown that alterations in the autophagy pathway by disruption of ATG proteins lead to progressive motor deficits and neurodegeneration (Hara et al., 2006; Komatsu et al., 2006). In these mice, polyubiquitinated proteins accumulate as inclusion bodies in neurons, which increase in size and number with age. Studies with *SOD1*^{G93A} ALS mice showed that MNs display enlarged autophagosomes with ubiquitinated aggregates, resulting in NMJ denervation. Inhibition of autophagy by ATG7 depletion in the mice accelerates the denervation of muscle fibers, indicating that autophagy plays an important and beneficial role in early disease stages (Rudnick et al., 2017). In a mouse model of a late-onset MND that exhibits features of ALS and CMT disease, impaired formation of autophagosomes in MNs has been described, significantly contributing to disease progression (Lüningschrör et al., 2017). These findings highlight the intricate relationship between autophagy dysfunction and the pathogenesis of various neurodegenerative diseases.
Under physiological conditions, polyubiquitinated proteins can be degraded through selective autophagy. The selectivity in autophagy is conferred by autophagy receptors that facilitate the tethering of cargo to the isolation membranes by simultaneously binding the cargo and LC3 (Zaffagnini & Martens, 2016). Various forms of selective autophagy contribute to the clearance of cytoplasmic materials such as aggregated proteins (Lamark & Johansen, 2012; Stolz et al., 2014), while dysregulation of selective autophagy is implicated in the pathogenesis of neurodegenerative diseases (Menzies et al., 2015).
Accumulation and aggregation of misfolded proteins are common features in many neurodegenerative diseases, particularly those with a late onset such as ALS, Alzheimer's disease and Parkinson's disease indicating that impaired protein degradation plays a role in the disease process (Lynch-Day et al., 2012; Ramesh & Pandey, 2017; Zare-Shahabadi et al., 2015). Unlike mitotic cells that can clear cytoplasmic protein aggregates during cell division, postmitotic neurons rely on autophagy for the degradation of long-lived proteins and protein aggregates. Mutated ALS-causing proteins, such as SOD1 or TDP43, particularly accumulate as cytosolic inclusions (Ramesh & Pandey, 2017). Further, it is noteworthy that many genes associated with neurodegenerative diseases are involved in the autophagy pathway. Among

the 34 major genes known to be implicated in ALS, six genes have been associated with autophagy (Hardiman et al., 2017; Suzuki et al., 2022).

4 Aims of the study

The main aim of this research was to investigate pathophysiological mechanisms in two different MNDs by using mouse models and human iPSC-based models.

The goal of the first part of this study was to develop new experimental strategies to analyze MND, specifically for ALS. To create complementary alternatives to animal models, we intended to improve existing cell culture techniques based on human iPSCs. For the investigation of MNDs and especially of functional synapses an innervating muscular target is necessary to enable the formation of NMJs. Therefore, the we wanted to establish and validate a human neuromuscular 3D co-culture system that can be used to model human ALS. iPSC derived MNs from healthy donors and ALS patients should be co-cultured in 3D conditions with skeletal muscle tissue derived from primary human myoblasts. Thereby the generation of contractile myofibers and adult NMJs *in vitro* should be supported. For this purpose, two control iPSC-lines and two ALS iPSC-lines with different mutations in the *SOD1* gene should be differentiated into MNs and co-cultured with primary myoblasts. Subsequently, we aimed to validate the functionality and maturation of the 3D muscle tissue and the 3D neuromuscular co-cultures. The last goal was to validate the application of this co-culture system to model aspects of human ALS pathophysiology by using MNs derived from ALS-lines.

The second part of this study examines the analysis of pathological mechanisms in Plekhg5-associated MND. Previous studies in Plekhg5-deficient mice show that dysregulation of Plekhg5-regulated presynaptic autophagy results in accumulation at swollen axon terminals in the spinal cord and MN terminals in skeletal muscle, causing the loss of motor function. However, these accumulations were not fully analyzed yet. Dysfunctional autophagy is associated with several MNDs and with pathological protein aggregates. Therefore, the first goal was to investigate if Sod1 is a cargo of these accumulations, since it is a leaderless cytosolic protein, which on the one hand accumulates in ALS-associated neurons, and on the other hand, which undergoes unconventional secretion involving secretory autophagy pathways. Further, we intended to investigate if Plekhg5 drives the UPS of Sod1 *in vitro*, by analyzing Sod1 secretion levels in Plekhg5 depleted mouse MNs and NSC34 cells. By interfering with autophagy pathways and exosome pathways, we intend to analyze involved pathways for Sod1 secretion. Lastly, we planned to investigate PLEKHG5-related pathological mechanisms in a human model by utilizing iPSC derived MNs from heathy donors and ALS patients with *SOD1* mutations. The aim was to investigate correlations between the two MND-associated proteins PLEKHG5 and SOD1 by analyzing SOD1 secretion in dependency of PLEKHG5.

5 Discussion and Summary

5.1 3D neuromuscular co-cultures

5.1.1 Generation of MNs and 3D muscle tissue

In the first part of our study, we present a human co-culture system based on human iPSC derived MNs and skeletal myoblasts. We adapted a previously described method to generate mature NMJs *in vitro* and showed the functional formation of NMJs after two weeks in co-cultures by glutamate-induced muscle contraction. We differentiated MNs from patient derived iPSCs harboring ALS-linked *SOD1* mutations and showed that ALS MNs functionally integrate into co-cultures but develop pathological signs of ALS at later stages. Our results show the successful generation of functional human NMJs in co-cultures, which can be used to study the NMJ physiology in healthy conditions and as a disease model for MNDs like ALS.

We generated human MNs from two iPSC-lines from healthy donors and validated the correct MN differentiation by morphological characterization and analysis of gene expression markers. By using an established differentiation protocol, we gained 75% MNs in our cultures. However, it was reported that iPSC derived MNs in monocultures recapitulate an immature state due to missing innervating targets (Sances et al., 2016). We propose that we could overcome this problem by co-culturing MNs with target muscle cells and thereby supporting MN maturation. Thus, we were able to generate co-cultures with a high ratio of pure MNs and muscle induced mature MNs.

Nevertheless, we tested whether muscle innervation could be improved by enriching the MN yield. For this purpose, MNs were transduced with an *HB9::GFP*-expressing lentivirus, which labeled the *HB9*-expressing MNs with GFP. Subsequently, the GFP expressing MNs were purified using Fluorescence Activated Cell Sorting (FACS), and co-cultured with muscle cells. These co-cultures, however, did not show improved contraction compared to the corresponding controls. This effect remained unchanged even after a longer cultivation period, indicating that muscle innervation and contraction are not enhanced by further enrichment of the MN.

We used primary human skeletal myoblasts from two biopsies to generate functional 3D muscle tissue. Although, both myoblast batches could be differentiated into functional muscle tissue with no morphological differences, we observed batch-to-batch variations in the strength of muscle contraction. Further, primary myoblasts displayed a limited cell source in our experiments due to limited passage numbers. Therefore iPSC derived myoblasts or myoblast cell lines might represent a suitable alternative as muscle cell starter population. Immortalized human myoblast cell lines were used in 2D culture experiments (Lathuiliere et al., 2022;

Mamchaoui et al., 2011) but are rarely utilized in experiments in 3D co-culture studies (Afshar Bakooshli et al., 2019). In a comprehensive study from 2020 the capability of the immortalized human myogenic cell line Hu5/KD3 was presented to generate contractile 3D muscle tissues. An intriguing avenue for future directions would involve the examination of Hu5/KD3 cells to assess their potential to generate functional muscle tissue that establishes connections with MNs. MNs and muscle cells derived from the same iPSCs with the same genetic background allow a more realistic recapitulation of disease conditions. The differentiation and co-culturing of iPSCs derived 3D muscle tissue with iPSC MNs was reported earlier, however muscle cells and MNs were differentiated from different iPSC lines (Osaki et al., 2018). The successful differentiation of myoblasts and MNs from the same iPSCs was shown in a recent study presenting a promising approach to address the limitations associated with primary myoblasts (Pinton et al., 2022). However, this advantage must be evaluated against the disadvantage that iPSC-derived muscle tissue typically displays an embryonic identity (Jiwlawat et al., 2018; Selvaraj et al., 2019).

5.1.2 *In vitro* NMJ formation and maturation

Human NMJs have thin pre-terminal axons, which branch numerous times as boutons at the postsynaptic muscle membrane, that in turn shows a high extent of postsynaptic folding. Although we observed functional NMJs in our neuromuscular co-cultures, we failed to show this characteristic and physiologically crucial NMJ morphology, appearing as nummular structures with coin-shaped patches (Boehm et al., 2020; Jones et al., 2017). To our knowledge, the hurdle to generate NMJs which recapitulate the *in vivo* morphology has not been cleared yet in co-culture studies with MNs and muscle cells (Afshar Bakooshli et al., 2019; Osaki et al., 2018; Steinbeck et al., 2016; Stoklund Dittlau et al., 2021). One decisive factor for poor NMJ formation could be the absence of terminal Schwann cells in these culture systems. *In vivo*, human NMJs comprise the presynaptic axon terminals of MNs, the postsynaptic muscle membrane and terminal Schwann cells. These contact sites are highly specialized structures and are capped by terminal Schwann cells, which function as protection layer. During embryonic and postnatal NMJ maturation, Schwann cells provide trophic support, thereby contributing to growth of the axon terminal, axon sprouting and NMJ formation and maturation (Alhindi et al., 2021; Castelnovo et al., 2017; Darabid et al., 2014; Hörner et al., 2021; Powell & Phillips, 2021; Santosa et al., 2018a, 2018b; Simon et al., 2010; Son et al., 1996). On the muscle side, Schwann cells support myotube development and the size and number of AChRs (Hörner et al., 2021). Additionally, dysfunction of terminal Schwann cells has been linked to the degeneration of MNs in ALS, highlighting this cell type as an important component for the investigation of pathogenic mechanisms (Santosa et al., 2018b). Therefore, the inclusion of terminal Schwann cells could improve the development and maturation of

NMJs *in vitro*. In future approaches, Schwann cell precursor cells could be differentiated from iPSCs and co-cultured in an advanced protocol with MNs and muscle cells (Powell & Phillips, 2021). So far, the differentiation, validation, and co-culturing of iPSC derived Schwann cells is not well investigated and might open new avenues for NMJ modeling.

Another aspect which could be considered to improve NMJ formation is a longer culturing period. Although embryonic NMJs display at nine weeks already functional structures, they do not show the typical NMJ morphology, yet (Hesselmans et al., 1993; Juntunen & Teräväinen, 1972). NMJs undergo several postnatal changes, including remarkable changes in the innervation structure and on molecular level. The size of the endplate, the numbers of AChRs, and the size of the active zones increases. Furthermore, junctional folds gradually became deeper and more prominent, postnatally (Sanes & Lichtman, 1999; Stifani, 2014). For the generation of co-cultures, we adapted a previously published method to generate NMJs by inducing the conversion of postsynaptic AChRs from an embryonic to an adult form (Afshar Bakooshli et al., 2019), and could show in our data viable and functional NMJs for up to six weeks. Due to the normally congruent coupling between presynaptic and postsynaptic morphology (Pratt et al., 2015), we suppose that adult postsynaptic structures support presynaptic development and thereby the general NMJ formation. However, we assume that these NMJs still represent an early developmental stage, and therefore a prolonged culture period could play a crucial role to ensure NMJ maturation. Furthermore, gene expression changes accompany the developmental progression of MNs, reflecting their functional maturation from embryonic to adult stages. In a recent study the transcriptional profiles of *in vivo* mouse spinal MNs were mapped from embryonic to adult stage and compared to transcriptional profiles of *in vitro* MNs. Profiling of *in vivo* MNs showed that gene expression and chromatin accessibility undergo dynamic changes for a period of four weeks, starting from MN specification until the third postnatal week. Subsequently, these changes stabilize and remain consistent throughout the lifespan. Interestingly, mouse embryonic stem cell derived MNs exhibited approximately 40% resemblance to the maturation expression program (Patel et al., 2022). The fact that MN gene expression changes during the first postnatal weeks supports our hypothesis that NMJs in co-culture still might not be fully matured. We validated the correct iPSC differentiation into MNs by analyzing expression patterns of several marker genes during MN differentiation and at two weeks of MN maturation. However, a more comprehensive transcriptional characterization of MNs and its comparison to transcriptional profiles of *in vivo* spinal MNs would be a necessary and interesting future approach to evaluate maturation processes. This approach is of particularly importance to determine the comparability to *in vivo* counterparts and to determine the overall presynaptic maturation stage of the NMJs in co-cultures. Specifically, transcriptional profiling over longer culture periods

would be necessary to address these questions. Longer culturing periods might lead to mature NMJ with adult MN transcriptional profile and improved NMJ functionality.
Lastly, another aspect to improve NMJ maturation and maintenance are defined medium components. We supplemented our co-culture medium with Agrin to support AChR clustering and NMJ formation in a 3D environment. However, several molecules, like fibroblast growth factor, HB-GAM/pleiotrophin, laminin beta 2, and midkine have been reported to promote NMJ formation in mouse and human cultures *in vitro* and could be tested in future *in vitro* approaches (Afshar Bakooshli et al., 2019; Sanes & Lichtman, 1999). Lastly, repeated co-culture stimulation could support NMJ maturation (Fukazawa et al., 2013; Lee et al., 2023). One possibility could be to enrich the culture medium with NMDA and/or AMPA receptor agonists.

5.1.3 Future directions for 3D co-cultures

We stimulated MNs with glutamate to induce muscle contraction in the co-cultures. Glutamate application in too high doses can induce toxicity and exposes the whole culture to glutamate, in contrast to locally activating NMJs as in the *in vivo* situation (Foran & Trotti, 2009; Sattler & Tymianski, 2001). A more sophisticated, precise strategy could be the optogenetic stimulation of MNs. However, we were not able to develop a co-culture system which can be optogenetically activated. We transduced MNs with a lentivirus construct expressing *Channelrhodopsin-2-YFP* (*ChR2-YFP*), a blue light sensitive Ion channel tagged to a fluorophore and could detect successful expression of ChR2 in 2D cultured MNs by staining (data not shown). Unfortunately, blue light stimulation of co-cultures generated with ChR2-YFP MNs did not result in muscle contraction. One possible reason might be that the yield of *ChR2* expressing MNs was too low to induce a detectable muscle contraction. In future experiments ChR2-YFP positive MNs could be purified by FACS prior co-culture generation, which might result in a more precisely inducible, robust muscle contraction.
To validate the functionality of bioengineered NMJs at different developmental stages, electrophysiological measurements are required to determine the physiological properties of the MNs and muscle cells. This approach is particularly important to determine the maturation stage of the NMJ. Electrophysiological changes during MN maturation included decreasing input resistance, increasing action potential firing frequency, spike frequency adaptation and rebound action potential firing (Faustino Martins et al., 2020; Takazawa et al., 2012). On the postsynaptic side, muscle maturation leads to spontaneous firing, independent from synaptic activity, and age-dependent enhancement of endplate potential (Vilmont et al., 2016). However, the size and 3D structure of the co-culture made it challenging to identify innervated muscle fibers and the corresponding MNs that build synaptic contact to them. The manual application of glutamate to the culture dish resulted in minor shifts of the co-culture which also

presented a problem for electrophysiological measurements. An approach in future experiments to detect randomly distributed NMJs in 3D co-cultures is the use of Rabies virus-based retrograde tracing (Bellmann et al., 2019). By using retrograde labeling with recombinant Rabies viruses, muscle innervating MNs can be specifically marked, enabling a selective examination of innervating and non-innervating MNs and target muscles. Utilizing such an approach could overcome the challenge of identifying MNs and innervated muscle fibers for electrophysiological measurements and help to analyze neuromuscular circuits.

Further, we tried to adapt the co-culture system into a 3D compartmentalized device. Compactization of co-culture models allows the local separation of cell types and a more realistic recapitulation of the human physiology. MN somata, axonal outgrowth and muscle formation are better detectable, which is an advantage for several readouts, especially in regard to immunochemical staining. Further, the local separation allows the establishment of microenvironments for the MNs and muscle cells for optimized culturing conditions. We used commercially available compartmentalized devices with two separate chambers for MN and muscle cell seeding and were able to culture MNs, which displayed axonal outgrowth through microchannels towards the muscle compartment (data not shown). However, we failed to generate contractile 3D muscle tissue in these chambers. These devices ensure compartmentalized culturing but miss a dumbbell-shaped chamber and Velcro hooks for 3D muscle culturing. Although we attached Velcro hooks before muscle cell seeding, adaption for 3D culturing was not possible, most likely because of the square shaped compartment instead of dumbbell-shaped compartment.

5.1.4 3D co-cultures for ALS modeling

Our findings that ALS MNs functionally integrate into the system but start to show signs of a pathological phenotype align with other studies that utilized sensorimotor organoids to model ALS *in vitro*. The authors showed that organoids carrying a specific *SOD1* ALS mutation present impairment at the NMJ level, as demonstrated by contraction and immunocytochemical measurements (Pereira et al., 2021). We maintained our co-cultures for six weeks and could see differences between control and ALS co-cultures in NMJ stability shown by decreasing muscle contraction and reduced axonal stability and coverage. These differences were significant when we pooled the data for both *SOD1* mutations. It was reported that $SOD1^{D90A}$ mutations present a less aggressive, slowly progressive form of ALS with early clinical and neurophysiological signs (Andersen, 2006; Berdyński et al., 2022; Luigetti et al., 2009). Therefore, we assume that longer culturing periods will result in more distinct differences between control and ALS co-cultures.

In addition to the pathological phenotypes that we observed in the ALS co-cultures, electrophysiological characterization of control and ALS co-cultures could reveal disease-

related mechanisms. Studies showed that iPSC derived ALS MNs recapitulate hyperexcitability, which is a pathophysiological hallmark in ALS (Burley et al., 2022; Wainger et al., 2014). It would be interesting to analyze this in our co-culture system and it would be a good readout for future directions. In addition, it would be from great interest to generate and validate co-cultures with patient derived MNs which harbor mutations associated to other MNDs.

Autophagy is an essential cellular quality control mechanism that plays a central role in the pathophysiology of ALS. Therefore, we investigated whether altered autophagy in axon terminals of ALS co-cultures could be detected compared to control co-cultures. MN were transduced with a lentivirus expressing *mRFP-LC3* prior to their use in co-cultures. This allowed the examination of autophagosomes using confocal microscopy. Although we could detect the expression of mRFP in 2D MN cultures, we were unable to detect autophagosomes in the 3D co-cultures due to the macroscopic structure of the cultures (data not shown). The autofluorescence of the hydrogel posed challenges in the analysis, making it difficult to detect weak fluorescence signals such as mRFP-LC3. So far, no solution has been found for this issue. One possibility could be to use higher-resolution microscopy or create cryosections of the 3D cultures for analysis.

The developed 3D neuromuscular co-culture system with myoblast derived muscle tissue and iPSC derived MNs provides a valuable tool for modeling NMJ-affecting human diseases and studying human NMJ development. Although we could not show the characteristic morphology of human NMJs *in vivo*, we could prove NMJ functionality, which could be maintained during the whole culture period. This system may aid in the development and validation of new mechanistic hypotheses for early pathogenesis in neuromuscular diseases, particularly ALS, where the NMJs are early and vulnerable targets, serving as important pathological and functional disease indicators (Fischer et al., 2004; Murray et al., 2010; Piotrkiewicz & Hausmanowa-Petrusewicz, 2013).

5.2 PLEKHG5-regulated SOD1 secretion

5.2.1 Mechanistic pathways

In the second part of this study, we analyzed pathological mechanisms linked to the lower MND-associated protein Plekhg5. We found that Plekhg5 drives the UPS of Sod1 by presynaptic autophagy, an essential cellular secretion pathway in neurons that contributes to the maintenance of global proteostasis. These findings highlight an unexpected

pathophysiological mechanism that converges two MND-associated proteins into a common pathway.

Our results demonstrate that the UPS of Sod1 depends on Atg9 and Atg5, but not on Atg2. This implies that the secretion of Sod1 relies on phagophore generation and LC3 lipidation, but not on phagophore extension and closure. We showed that Sod1 is sequestered into the intermembrane space of autophagosomes which fuse with secretory lysosomal-related organelles (LROs). LROs subsequently fuse with the plasma membrane and thereby release Sod1 into the extracellular milieu. This pathway was reported for the cytokine IL-1β, which is, similar to Sod1, integrated in the intermembrane space and might explain our findings (Zhang et al., 2015). Additionally, the observation that Sod1 is predominantly secreted as a free protein supports this idea. However, we could not address so far which exact role Plekhg5 plays in this pathway. To answer this question further experiments are necessary to explore the underlying mechanistical pathways and Plekhg5 interaction partners.

Plekhg5 is a GEF for the GTPases Rab26 and RhoA. Therefore, both are likely candidates to be involved in the UPS of Sod1 by autophagy. Rab26 plays a role in synaptic vesicle recruitment for autophagy by selectively delivering synaptic vesicles into pre-autophagosomes. It has been shown to be an important regulator of vesicular fusion and trafficking. (Binotti et al., 2015). Furthermore, depletion of Plekhg5 in mice results in accumulations of Rab26 positive synaptic vesicles at MN terminals (Lüningschrör et al., 2017). It might be that Rab26 also plays a role vesicle recruitment for secretory autophagy, representing a determining mechanism in the Sod1 secretion pathway. In ongoing experiments, we analyzed MNs from *Plekhg5*$^{-/-}$ mice which express a constitutive active form of *Rab26* (*Rab26-QL*). We could not detect a restorage of extracellular Sod1 levels by *Rab26-QL* expression in *Plekhg5*$^{-/-}$ MNs compared to controls MNs (data not shown). However, these are preliminary data with low numbers of experimental repetition which need to be further investigated. RhoA is involved in actin polymerization, actomyosin contractility, and microtubule dynamics. Thereby it regulates vesicular locomotion, intracellular transport, and exocytosis through reorganization of actin filaments (de Seze et al., 2023; A. Hall, 1998; Komuro et al., 1996; Kowluru et al., 1997). We assumed that these transport processes might be involved in Sod1 secretion and tested if Sod1 secretion is affected in primary MNs which express dominant negative *RhoA* (*RhoA-TN*). We found, to our surprise, an increase in extracellular Sod1 levels, indicating that RhoA is not involved in Plekhg5-dependent Sod1 secretion pathways (data not shown).

Another potential candidate which might be involved in Sod1 secretion is the GTPase RhoE. RhoE regulates RhoA activity by suppressing Plekhg5 and by preventing RhoA interaction with ROCK1 for the phosphorylation of downstream target pathways (Dempsey et al., 2012; Goh & Ed, 2010). Therefore, RhoE acts as a negative regulator of cytoskeletal organization which

might impair Sod1 secretion. In future *in vitro* experiments we would like to analyze the effect of RhoE-QL and of dominant negative RhoE-TN on the extracellular Sod1 secretion.
Our presented data strongly suggests that the GTPase Rab27 is required for the secretion of Sod1. Rab27 is involved in vesicular fusion and trafficking, exosome secretion pathways, and initiates multivesicular endosome docking at the plasma membrane (Underwood et al., 2020). Further Rab27 is marker for secretory LROs, but not for genuine lysosomes (Barral et al., 2022). In this study we show that Sod1 accumulations in mouse spinal cord MNs are positive for Rab27 and that expression of *Rab27-TN* in primary MNs results in a significant reduction of extracellular Sod1 levels. The data presented so far, along with future experiments, have the potential to uncover additional Sod1 secretion mechanisms.

5.2.2 ALS-linked SOD1 secretion in human iPSC MNs

To investigate the results in a disease model, which recapitulates the human genetic background and protein expression levels more realistically, we utilized the same two human control iPSC-lines and two ALS-linked *SOD1* iPSC-lines as in the 3D neuromuscular co-culture study. We found reduced SOD1 levels in the medium of ALS MNs compared to control MNs and concluded that SOD1 secretion is impaired in ALS MNs. Interestingly, the reduction in SOD1 secretion was more pronounced in the case of $SOD1^{D90A/D90A}$ compared to $SOD1^{+/R115G}$. MNs with homozygous D90A mutation showed significantly decreased secretion compared to wildtype *SOD1*, as analyzed in two control lines from healthy donors. To exclude that these effects are due to cell line variabilities we additionally used an isogenic control line. We could also show significantly reduced mutant *SOD1* secretion when we compared it to its corrected, isogenic counterpart, which further confirmed that SOD1 secretion in ALS MNs is impaired.
The different results of the *SOD1* mutations might be explained by their distinct structural properties. The R115G mutation in *SOD1* leads to structurally unstable proteins, whereas the $SOD1^{D90A/D90A}$ mutant protein is structurally stable and retains enzymatic activity comparable to wildtype SOD1 (Andersen, 2006; Marklund et al., 1997). However, the D90A mutation is located near the acidic amino acid stretch, which has been identified as an export signal and may impact the recognition of an unidentified binding partner, leading to impaired secretion. Furthermore, the double-substitution DE77/78AA within the acidic motif of *SOD1*, which was reported in a recent study to block SOD1 secretion, exhibits a similar increased mobility in SDS-PAGE as the ALS-linked D90A variant. In accordance with our findings this study also shows a reduced secretion of mutant ALS-linked $SOD1^{G93A}$ compared to its wildtype counterpart upon overexpression in Hela cells (Cruz-Garcia et al., 2017). This suggests that alterations in polypeptide properties may affect protein secretion.
The differences between both *SOD1* lines could also be based on the fact that $SOD1^{+/R115G}$ MNs harbor a heterozygous mutation instead of a homozygous mutation. Since cytosolic

SOD1 builds homodimers, the cell functionality might be maintained by a proportion of homodimers with wildtype SOD1 and a proportion of probably less severe heterodimers, while in *SOD1$^{D90A/D90A}$* MNs mutated SOD1 secretion cannot be compensated.

Additionally, we show that impaired secretion of SOD1$^{D90A/D90A}$ coincides with reduced protein expression of PLEKH5 in the lysates of *SOD1$^{D90A/D90A}$* MNs, supporting our hypothesis that SOD1 secretion depends on PLEKHG5. Strikingly, *PLEKHG5* depletion in control MNs resulted in reduced SOD1 secretion, which further confirmed the dependency between SOD1 and PLEKH5. However, we did not analyze PLEKHG5 protein expression in *SOD1$^{+/R115G}$* MNs. We assume that in these MNs PLEKHG5 expression is similar to control MNs which might explain the moderate decrease in extracellular SOD1 level. This needs to be confirmed in future experiments. Overall, these findings provide insights into the differential effects of ALS-linked *SOD1* mutations on SOD1 secretion and highlight potential structural and molecular mechanisms underlying these observations.

To support our findings on PLEKHG5 dependent SOD1 secretion in future experiments, we need to analyze SOD1 secretion after lentiviral overexpression of *PLEKHG5* in *SOD1$^{D90A/D90A}$* MNs. For this approach, MNs could be transduced with a lentiviral vector expressing *Flag-tagged PLEKHG5* followed by the quantification of SOD1 medium levels. We assume that restoring the *PLEKHG5* expression in *SOD1$^{D90A/D90A}$* MNs will rescue the SOD1 secretion.

In summary, the interplay between Plekhg5 and Sod1 connects two different facets of MNDs. These findings highlight an unexpected pathophysiological mechanism that converges two MND-associated proteins into a common pathway. The data provide important insights by using mouse models and human MNs. For future approaches the pressing question remains as to what insights can be gained using a human neuromuscular 3D model to analyze PLEKHG-regulated SOD1 secretion.

5.2.3 3D co-cultures for the analysis of PLEKHG5-associated MND

The human and the mouse NMJ share important features but also show differences in their morphology and at the molecular level which can result in distinct pathophysiological phenotypes. So far, we have not analyzed SOD1 accumulations in axons in a human system with *PLEKHG55*-depletion. This could be explored in more detail in our presented human neuromuscular system. It is tempting to assume that *PLEKHG5* depletion will result in a similar pathological phenotype with SOD^{+} accumulations and swollen axon terminals as in *Plekhg5* depleted mice. However, this needs to be deeper investigated. Furthermore, studying the effect of *PLEKHG5* depletion on wildtype and mutant SOD1 secretion in a more physiological, functional 3D human NMJ model would be of great interest. In 2D cultures we found impaired secretion of mutated SOD1. For these experiments we used the same cell lines as for the generation of ALS co-cultures with *SOD1* mutation. These ALS co-cultures showed degrading

muscle contraction and low axonal coverage compared to control co-cultures. One reason for this might be impaired SOD1 secretion which we saw in 2D MN cultures. To address this question, we need to analyze extracellular SOD1 levels in control and ALS co-cultures. Lastly, in co-culture systems with an innervating target, the impact on postsynaptic structures and muscle contraction would be interesting. In mice, *Plekhg5* depletion leads to motor deficits recapitulating a late onset MND. We propose that *PLEKHG5* depletion in the co-culture system will lead to progressive loss of muscle contraction, similar to the results that we reported for ALS co-cultures. The combination of *PLEKHG5* deficiency in ALS co-cultures remains elusive and needs to be investigated in future experiments.

In summary, for future perspectives the presented co-culture system in our first study could be utilized to analyze further pathophysiological mechanism associated to the two MND related proteins PLEKHG5 and SOD1.

6 References

Afshar Bakooshli, M., Lippmann, E. S., Mulcahy, B., Iyer, N., Nguyen, C. T., Tung, K., Stewart, B. A., van den Dorpel, H., Fuehrmann, T., Shoichet, M., Bigot, A., Pegoraro, E., Ahn, H., Ginsberg, H., Zhen, M., Ashton, R. S., & Gilbert, P. M. (2019). A 3D culture model of innervated human skeletal muscle enables studies of the adult neuromuscular junction. *ELife*, *8*. https://doi.org/10.7554/eLife.44530

Alhindi, A., Boehm, I., Forsythe, R. O., Miller, J., Skipworth, R. J. E., Simpson, H., Jones, R. A., & Gillingwater, T. H. (2021). Terminal Schwann cells at the human neuromuscular junction. *Brain Communications*, *3*(2). https://doi.org/10.1093/BRAINCOMMS/FCAB081

An, T., Shi, P., Duan, W., Zhang, S., Yuan, P., Li, Z., Wu, D., Xu, Z., Li, C., & Guo, Y. (2014). Oxidative stress and autophagic alteration in brainstem of SOD1-G93A mouse model of ALS. *Molecular Neurobiology*, *49*(3), 1435–1448. https://doi.org/10.1007/S12035-013-8623-3

Andersen, P. M. (2006). Amyotrophic lateral sclerosis associated with mutations in the CuZn superoxide dismutase gene. *Current Neurology and Neuroscience Reports*, *6*(1), 37–46. https://doi.org/10.1007/S11910-996-0008-9

Andersen, P. M., Nilsson, P., Ala-Hurula, V., Keränen, M. L., Tarvainen, I., Haltia, T., Nilsson, L., Binzer, M., Forsgren, L., & Marklund, S. L. (1995). Amyotrophic lateral sclerosis associated with homozygosity for an Asp90Ala mutation in CuZn-superoxide dismutase. *Nature Genetics*, *10*(1), 61–66. https://doi.org/10.1038/NG0595-61

Arbab, M., Baars, S., & Geijsen, N. (2014). Modeling motor neuron disease: the matter of time. *Trends in Neurosciences*, *37*(11), 642–652. https://doi.org/10.1016/J.TINS.2014.07.008

Azzedine, H., Zavadakova, P., Planté-Bordeneuve, V., Pato, M. V., Pinto, N., Bartesaghi, L., Zenker, J., Poirot, O., Bernard-Marissal, N., Gouttenoire, E. A., Cartoni, R., Title, A., Venturini, G., Médard, J. J., Makowski, E., Schö ls, L., Claeys, K. G., Stendel, C., Roos, A., … Chrast, R. (2013). PLEKHG5 deficiency leads to an intermediate form of autosomal-recessive Charcot–Marie–Tooth disease. *Human Molecular Genetics*, *22*(20), 4224–4232. https://doi.org/10.1093/HMG/DDT274

Barral, D. C., Staiano, L., Guimas Almeida, C., Cutler, D. F., Eden, E. R., Futter, C. E., Galione, A., Marques, A. R. A., Medina, D. L., Napolitano, G., Settembre, C., Vieira, O. V., Aerts, J. M. F. G., Atakpa-Adaji, P., Bruno, G., Capuozzo, A., De Leonibus, E., Di Malta, C., Escrevente, C., … Seabra, M. C. (2022). Current methods to analyze lysosome morphology, positioning, motility and function. *Traffic (Copenhagen, Denmark)*, *23*(5), 238–269. https://doi.org/10.1111/TRA.12839

Bart van der Worp, H., Howells, D. W., Sena, E. S., Porritt, M. J., Rewell, S., O'Collins, V., & Macleod, M. R. (2010). Can Animal Models of Disease Reliably Inform Human Studies? *PLoS Medicine*, *7*(3), 1–8. https://doi.org/10.1371/JOURNAL.PMED.1000245

Bellmann, J., Goswami, R. Y., Girardo, S., Rein, N., Hosseinzadeh, Z., Hicks, M. R., Busskamp, V., Pyle, A. D., Werner, C., & Sterneckert, J. (2019). A customizable microfluidic platform for medium-throughput modeling of neuromuscular circuits. *Biomaterials*, *225*, 119537. https://doi.org/10.1016/J.BIOMATERIALS.2019.119537

Berdyński, M., Miszta, P., Safranow, K., Andersen, P. M., Morita, M., Filipek, S., Żekanowski, C., & Kuźma-Kozakiewicz, M. (2022). SOD1 mutations associated with amyotrophic lateral sclerosis analysis of variant severity. *Scientific Reports 2022 12:1*, *12*(1), 1–11. https://doi.org/10.1038/s41598-021-03891-8

Bienfait, H. M. E., Verhamme, C., Van Schaik, I. N., Koelman, J. H. T. M., De Visser, B. W. O., De Haan, R. J., Baas, F., Van Engelen, B. G. M., & De Visser, M. (2006). Comparison of CMT1A and CMT2: Similarities and differences. *Journal of Neurology*, *253*(12), 1572–1580. https://doi.org/10.1007/S00415-006-0260-6/TABLES/2

Binotti, B., Pavlos, N. J., Riedel, D., Wenzel, D., Vorbrüggen, G., Schalk, A. M., Kühnel, K., Boyken, J., Erck, C., Martens, H., Chua, J. J. E., & Jahn, R. (2015). The GTPase Rab26 links synaptic vesicles to the autophagy pathway. *ELife*, *4*, e05597. https://doi.org/10.7554/ELIFE.05597

Bird, T. D. (2023). Charcot-Marie-Tooth Hereditary Neuropathy Overview. *GeneReviews®*. https://www.ncbi.nlm.nih.gov/books/NBK1358/

Birdsall, V., & Waites, C. L. (2019). Autophagy at the Synapse. *Neuroscience Letters*, *697*, 24. https://doi.org/10.1016/J.NEULET.2018.05.033

Boehm, I., Alhindi, A., Leite, A. S., Logie, C., Gibbs, A., Murray, O., Farrukh, R., Pirie, R., Proudfoot, C., Clutton, R., Wishart, T. M., Jones, R. A., & Gillingwater, T. H. (2020). Comparative anatomy of the mammalian neuromuscular junction. *Journal of Anatomy*, *237*(5), 827–836. https://doi.org/10.1111/JOA.13260

Bornstein, M., & Breitbart, L. (1964). Anatomical studies of mouse embryo spinal cord-skeletal muscle in long-term tissue culture. *ANATOMICAL RECORD*, 148–362. https://www.webofscience.com/wos/woscc/full-record/WOS:A19644143A00063?SID=EUW1ED0B80R14GnPnb3NdnM6GSyJH

Bosco, D. A., Morfini, G., Karabacak, N. M., Song, Y., Gros-Louis, F., Pasinelli, P., Goolsby, H., Fontaine, B. A., Lemay, N., McKenna-Yasek, D., Frosch, M. P., Agar, J. N., Julien, J. P., Brady, S. T., & Brown, R. H. (2010). Wild-type and mutant SOD1 share an aberrant conformation and a common pathogenic pathway in ALS. *Nature Neuroscience*, *13*(11), 1396–1403. https://doi.org/10.1038/NN.2660

Boya, P., Reggiori, F., & Codogno, P. (2013). Emerging regulation and functions of autophagy. *Nature Cell Biology*, *15*(7), 713–720. https://doi.org/10.1038/NCB2788

Brehm, P., & Henderson, L. (1988). Regulation of acetylcholine receptor channel function during development of skeletal muscle. *Developmental Biology*, *129*(1), 1–11. https://doi.org/10.1016/0012-1606(88)90156-X

Brenner, D., & Weishaupt, J. H. (2019). Update on amyotrophic lateral sclerosis genetics. *Current Opinion in Neurology*, *32*(5), 735–739. https://doi.org/10.1097/WCO.0000000000000737

Burbidge, K., Rademacher, D. J., Mattick, J., Zack, S., Grillini, A., Bousset, L., Kwon, O., Kubicki, K., Simon, A., Melki, R., & Campbell, E. M. (2022). LGALS3 (galectin 3) mediates an unconventional secretion of SNCA/α-synuclein in response to lysosomal membrane damage by the autophagic-lysosomal pathway in human midbrain dopamine neurons. *Autophagy*, *18*(5), 1020. https://doi.org/10.1080/15548627.2021.1967615

Burley, S., Beccano-Kelly, D. A., Talbot, K., Llana, O. C., & Wade-Martins, R. (2022). Hyperexcitability in young iPSC-derived C9ORF72 mutant motor neurons is associated with increased intracellular calcium release. *Scientific Reports 2022 12:1*, *12*(1), 1–8. https://doi.org/10.1038/s41598-022-09751-3

Carrasco, D. I., Bichler, E. K., Seburn, K. L., & Pinter, M. J. (2010). Nerve Terminal Degeneration Is Independent of Muscle Fiber Genotype in SOD1G93A Mice. *PLOS ONE*, *5*(3), e9802. https://doi.org/10.1371/JOURNAL.PONE.0009802

Cassina, P., Cassina, A., Pehar, M., Castellanos, R., Gandelman, M., De León, A., Robinson, K. M., Mason, R. P., Beckman, J. S., Barbeito, L., & Radi, R. (2008). Mitochondrial Dysfunction in SOD1G93A-Bearing Astrocytes Promotes Motor Neuron Degeneration: Prevention by Mitochondrial-Targeted Antioxidants. *The Journal of Neuroscience*, *28*(16), 4115. https://doi.org/10.1523/JNEUROSCI.5308-07.2008

Castelnovo, L. F., Bonalume, V., Melfi, S., Ballabio, M., Colleoni, D., & Magnaghi, V. (2017). Schwann cell development, maturation and regeneration: a focus on classic and emerging intracellular signaling pathways. *Neural Regeneration Research*, *12*(7), 1013. https://doi.org/10.4103/1673-5374.211172

Cavalli, G., & Cenci, S. (2020). Autophagy and Protein Secretion. *Journal of Molecular Biology*, *432*(8), 2525–2545. https://doi.org/10.1016/J.JMB.2020.01.015

Chen, Z., Maroofian, R., Başak, A. N., Shingavi, L., Karakaya, M., Efthymiou, S., Gustavsson, E. K., Meier, L., Polavarapu, K., Vengalil, S., Preethish-Kumar, V., Nandeesh, B. N., Gökçe Güneş, N., Akan, O., Candan, F., Schrank, B., Zuchner, S., Murphy, D., Kapoor, M., … Sarraf, P. (2021). Novel variants broaden the phenotypic spectrum of PLEKHG5-associated neuropathies. *European Journal of Neurology*, *28*(4), 1344–1355. https://doi.org/10.1111/ENE.14649

Chia, R., Chiò, A., & Traynor, B. J. (2018). Novel genes associated with amyotrophic lateral sclerosis: diagnostic and clinical implications. *The Lancet. Neurology*, *17*(1), 94–102. https://doi.org/10.1016/S1474-4422(17)30401-5

Crain, S. M., & Peterson, E. R. (1964). Complex bioelectric activity in organized tissue cultures of spinal cord (human, rat and chick). *Journal of Cellular and Comparative Physiology*, *64*(1), 1–13. https://doi.org/10.1002/JCP.1030640102

Cruz-Garcia, D., Brouwers, N., Duran, J. M., Mora, G., Curwin, A. J., & Malhotra, V. (2017). A diacidic motif determines unconventional secretion of wild-type and ALS-linked mutant SOD1. *The Journal of Cell Biology*, *216*(9), 2691. https://doi.org/10.1083/JCB.201704056

Darabid, H., Perez-Gonzalez, A. P., & Robitaille, R. (2014). Neuromuscular synaptogenesis: Coordinating partners with multiple functions. *Nature Reviews Neuroscience*, *15*(11), 703–718. https://doi.org/10.1038/NRN3821

Darras, B. T. (2011). Non-5q spinal muscular atrophies. *Neurology*, *77*(4), 312–314. https://doi.org/10.1212/WNL.0B013E3182267BD8

de Jongh, R., Spijkers, X. M., Pasteuning-Vuhman, S., Vulto, P., & Pasterkamp, R. J. (2021). Neuromuscular junction-on-a-chip: ALS disease modeling and read-out development in microfluidic devices. *Journal of Neurochemistry*, *157*(3), 393–412. https://doi.org/10.1111/JNC.15289

de Seze, J., Gatin, J., & Coppey, M. (2023). RhoA regulation in space and time. *FEBS Letters*, *597*(6), 836–849. https://doi.org/10.1002/1873-3468.14578

DeJesus-Hernandez, M., Mackenzie, I. R., Boeve, B. F., Boxer, A. L., Baker, M., Rutherford, N. J., Nicholson, A. M., Finch, N. C. A., Flynn, H., Adamson, J., Kouri, N., Wojtas, A., Sengdy, P., Hsiung, G. Y. R., Karydas, A., Seeley, W. W., Josephs, K. A., Coppola, G., Geschwind, D. H., … Rademakers, R. (2011). Expanded GGGGCC hexanucleotide repeat in non-coding region of C9ORF72 causes chromosome 9p-linked frontotemporal dementia and amyotrophic lateral sclerosis. *Neuron*, *72*(2), 245. https://doi.org/10.1016/J.NEURON.2011.09.011

Demestre, M., Orth, M., Föhr, K. J., Achberger, K., Ludolph, A. C., Liebau, S., & Boeckers, T. M. (2015). Formation and characterisation of neuromuscular junctions between hiPSC derived motoneurons and myotubes. *Stem Cell Research*, *15*(2), 328–336. https://doi.org/10.1016/J.SCR.2015.07.005

Dempsey, B. R., Rintala-Dempsey, A. C., Shaw, G. S., Zhu, Y. X., Stewart, A. K., Claudio, J. O., Runyan, C. E., Schnaper, H. W., King, P. D., Blunt, M. D., Ward, S. G., Reinhold, A., Schraven, B. L., Fukuda, M., Lee, J. R., Strebovsky, J., Dalpke, A. H., Mariniello, B., Ryan, K., … Horowitz, A. (2012). SYX/PLEKHG5, A Rhoa Guanine Exchange Factor Involved in Cell Migration and Angiogenesis. *Encyclopedia of Signaling Molecules*, 1827–1830. https://doi.org/10.1007/978-1-4419-0461-4_567

Deng, H. X., Hentati, A., Tainer, J. A., Iqbal, Z., Cayabyab, A., Hung, W. Y., Getzoff, E. D., Hu, P., Herzfeldt, B., Roos, R. P., Warner, C., Deng, G., Soriano, E., Smyth, C., Parge, H. E., Ahmed, A., Roses, A. D., Hallewell, R. A., Pericak-Vance, M. A., & Siddique, T. (1993). Amyotrophic Lateral Ssclerosis and Structural Defects in Cu,Zn Superoxide Dismutase. *Science*, *261*(5124), 1047–1051. https://doi.org/10.1126/SCIENCE.8351519

Devlin, A. C., Burr, K., Borooah, S., Foster, J. D., Cleary, E. M., Geti, I., Vallier, L., Shaw, C. E., Chandran, S., & Miles, G. B. (2015). Human iPSC-derived motoneurons harbouring TARDBP or C9ORF72 ALS mutations are dysfunctional despite maintaining viability. *Nature Communications*, *6*. https://doi.org/10.1038/NCOMMS6999

Donnelly, C. J., Zhang, P. W., Pham, J. T., Heusler, A. R., Mistry, N. A., Vidensky, S., Daley, E. L., Poth, E. M., Hoover, B., Fines, D. M., Maragakis, N., Tienari, P. J., Petrucelli, L., Traynor, B. J., Wang, J., Rigo, F., Bennett, C. F., Blackshaw, S., Sattler, R., & Rothstein, J. D. (2013). RNA Toxicity from the ALS/FTD C9ORF72

Expansion Is Mitigated by Antisense Intervention. *Neuron*, *80*(2), 415. https://doi.org/10.1016/J.NEURON.2013.10.015

Du, Z.-W., Chen, H., Liu, H., Lu, J., Qian, K., Huang, C.-L., Zhong, X., Fan, F., & Zhang, S.-C. (2015). Generation and expansion of highly pure motor neuron progenitors from human pluripotent stem cells. *Nature Communications*, *6*(1), 6626. https://doi.org/10.1038/ncomms7626

Dupont, N., Jiang, S., Pilli, M., Ornatowski, W., Bhattacharya, D., & Deretic, V. (2011). Autophagy-based unconventional secretory pathway for extracellular delivery of IL-1β. *The EMBO Journal*, *30*(23), 4701. https://doi.org/10.1038/EMBOJ.2011.398

Duran, J. M., Anjard, C., Stefan, C., Loomis, W. F., & Malhotra, V. (2010). Unconventional secretion of Acb1 is mediated by autophagosomes. *Journal of Cell Biology*, *188*(4), 527–536. https://doi.org/10.1083/JCB.200911154

Egawa, N., Kitaoka, S., Tsukita, K., Naitoh, M., Takahashi, K., Yamamoto, T., Adachi, F., Kondo, T., Okita, K., Asaka, I., Aoi, T., Watanabe, A., Yamada, Y., Morizane, A., Takahashi, J., Ayaki, T., Ito, H., Yoshikawa, K., Yamawaki, S., … Inoue, H. (2012). Drug screening for ALS using patient-specific induced pluripotent stem cells. *Science Translational Medicine*, *4*(145). https://doi.org/10.1126/SCITRANSLMED.3004052/SUPPL_FILE/4-145RA104_SM.PDF

Ejlerskov, P., Rasmussen, I., Nielsen, T. T., Bergström, A. L., Tohyama, Y., Jensen, P. H., & Vilhardt, F. (2013). Tubulin Polymerization-promoting Protein (TPPP/p25α) Promotes Unconventional Secretion of α-Synuclein through Exophagy by Impairing Autophagosome-Lysosome Fusion. *Journal of Biological Chemistry*, *288*(24), 17313–17335. https://doi.org/10.1074/JBC.M112.401174

Faustino Martins, J. M., Fischer, C., Urzi, A., Vidal, R., Kunz, S., Ruffault, P. L., Kabuss, L., Hube, I., Gazzerro, E., Birchmeier, C., Spuler, S., Sauer, S., & Gouti, M. (2020). Self-Organizing 3D Human Trunk Neuromuscular Organoids. *Cell Stem Cell*, *26*(2), 172-186.e6. https://doi.org/10.1016/j.stem.2019.12.007

Ferraiuolo, L., Kirby, J., Grierson, A. J., Sendtner, M., & Shaw, P. J. (2011). Molecular pathways of motor neuron injury in amyotrophic lateral sclerosis. *Nature Reviews. Neurology*, *7*(11), 616–630. https://doi.org/10.1038/NRNEUROL.2011.152

Fischer, L. R., Culver, D. G., Tennant, P., Davis, A. A., Wang, M., Castellano-Sanchez, A., Khan, J., Polak, M. A., & Glass, J. D. (2004). Amyotrophic lateral sclerosis is a distal axonopathy: evidence in mice and man. *Experimental Neurology*, *185*(2), 232–240. https://doi.org/10.1016/J.EXPNEUROL.2003.10.004

Foran, E., & Trotti, D. (2009). Glutamate Transporters and the Excitotoxic Path to Motor Neuron Degeneration in Amyotrophic Lateral Sclerosis. *Antioxidants & Redox Signaling*, *11*(7), 1587. https://doi.org/10.1089/ARS.2009.2444

Fujimori, K., Ishikawa, M., Otomo, A., Atsuta, N., Nakamura, R., Akiyama, T., Hadano, S., Aoki, M., Saya, H., Sobue, G., & Okano, H. (2018). Modeling sporadic ALS in iPSC-derived motor neurons identifies a potential therapeutic agent. *Nature Medicine*, *24*(10), 1579–1589. https://doi.org/10.1038/S41591-018-0140-5

Fukazawa, T., Matsumoto, M., Imura, T., Khalesi, E., Kajiume, T., Kawahara, Y., Tanimoto, K., & Yuge, L. (2013). Electrical stimulation accelerates neuromuscular junction formation through ADAM19/neuregulin/ErbB signaling in vitro. *Neuroscience Letters*, *545*, 29–34. https://doi.org/10.1016/J.NEULET.2013.04.006

Giovanni, J. Di, & Sheng, Z.-H. (2015). Regulation of synaptic activity by snapin-mediated endolysosomal transport and sorting. *The EMBO Journal*, *34*(15), 2059. https://doi.org/10.15252/EMBJ.201591125

Goh, L. L., & Ed, M. (2010). The RhoA GEF Syx is a target of Rnd3 and regulated via a Raf1-like ubiquitin-related domain. *PloS One*, *5*(8). https://doi.org/10.1371/JOURNAL.PONE.0012409

Goldstein, O., Kedmi, M., Gana-Weisz, M., Nefussy, B., Vainer, B., Fainmesser, Y., Drory, V. E., & Orr-Urtreger, A. (2020). A novel mutation in TARDBP segregates with amyotrophic lateral sclerosis in a large family with early onset and fast progression. *Amyotrophic Lateral Sclerosis & Frontotemporal Degeneration*, *21*(3–4), 280–285. https://doi.org/10.1080/21678421.2020.1747496

Gonzalez-Quereda, L., Pagola, I., Fuentes Prior, P., Bernal, S., Rodriguez, M. J., Torné, L., Salgado Garrido, J., Gallano, P., & Jericó, I. (2021). Novel PLEKHG5 mutations in a patient with childhood-onset lower motor neuron disease. *Annals of Clinical and Translational Neurology*, *8*(1), 294–299. https://doi.org/10.1002/ACN3.51265

Gundelfinger, E. D., Karpova, A., Pielot, R., Garner, C. C., & Kreutz, M. R. (2022). Organization of Presynaptic Autophagy-Related Processes. *Frontiers in Synaptic Neuroscience*, *14*, 2. https://doi.org/10.3389/FNSYN.2022.829354/BIBTEX

Guo, X., Das, M., Rumsey, J., Gonzalez, M., Stancescu, M., & Hickman, J. (2010). Neuromuscular Junction Formation Between Human Stem-Cell-Derived Motoneurons and Rat Skeletal Muscle in a Defined System. *Tissue Engineering. Part C, Methods*, *16*(6), 1347. https://doi.org/10.1089/TEN.TEC.2010.0040

Guo, X., Smith, V., Jackson, M., Tran, M., Thomas, M., Patel, A., Lorusso, E., Nimbalkar, S., Cai, Y., Mcaleer, C. W., Wang, Y., Long, C. J., Hickman, J. J., Guo, X., Smith, V., Jackson, M., Tran, M., Thomas, M., Patel, A., … Hickman, J. J. (2020). A Human-Based Functional NMJ System for Personalized ALS Modeling and Drug Testing. *Advanced Therapeutics*, *3*(11), 2000133. https://doi.org/10.1002/ADTP.202000133

Gurney, M. E., Pu, H., Chiu, A. Y., Dal Canto, M. C., Polchow, C. Y., Alexander, D. D., Caliendo, J., Hentati, A., Kwon, Y. W., Deng, H.-X., Chen, W., Zhai, P., Sufit, R. L., Siddique, T., Gurney, M. E., Pu, H., Alexander, D. D., Kwon, Y. W., Zhai, P., … Chen, W. (1994). Motor neuron degeneration in mice that express a human Cu,Zn superoxide dismutase mutation. *Science*, *264*(5166), 1772–1775. https://doi.org/10.1126/SCIENCE.8209258

Hall, A. (1998). Rho GTpases and the actin cytoskeleton. *Science*, *279*(5350), 509–514. https://doi.org/10.1126/SCIENCE.279.5350.509/ASSET/BA3BA44B-6EFA-45C0-9E4D-6F324E5F7690/ASSETS/GRAPHIC/SE0386202005.JPEG

Hall, Z. W., & Sanes, J. R. (1993). Synaptic structure and development: The neuromuscular junction. *Cell*, *72*(1001), 99–121. https://doi.org/10.1016/S0092-8674(05)80031-5

Hammond, C., & Esclapez, M. (2015). The chemical synapses. *Cellular and Molecular Neurophysiology: Fourth Edition*, 121–144. https://doi.org/10.1016/B978-0-12-397032-9.00006-6

Hanna, J., Cheng, A. W., Saha, K., Kim, J., Lengner, C. J., Soldner, F., Cassady, J. P., Muffat, J., Carey, B. W., & Jaenisch, R. (2010). Human embryonic stem cells with biological and epigenetic characteristics similar to those of mouse ESCs. *Proceedings of the National Academy of Sciences of the United States of America*, *107*(20), 9222–9227. https://doi.org/10.1073/PNAS.1004584107

Hardiman, O., Al-Chalabi, A., Chio, A., Corr, E. M., Logroscino, G., Robberecht, W., Shaw, P. J., Simmons, Z., & Van Den Berg, L. H. (2017). Amyotrophic lateral sclerosis. *Nature Reviews. Disease Primers*, *3*. https://doi.org/10.1038/NRDP.2017.71

Hayashi, Y., Homma, K., & Ichijo, H. (2016). SOD1 in neurotoxicity and its controversial roles in SOD1 mutation-negative ALS. *Advances in Biological Regulation*, *60*, 95–104. https://doi.org/10.1016/J.JBIOR.2015.10.006

Hesselmans, L. F. G. M., Jennekens, F. G. I., Van Den Oord, C. J. M., Veldman, H., & Vincent, A. (1993). Development of innervation of skeletal muscle fibers in man: Relation to acetylcholine receptors. *The Anatomical Record*, *236*(3), 553–562. https://doi.org/10.1002/AR.1092360315

Hirsch, N. P. (2007). Neuromuscular junction in health and disease. *British Journal of Anaesthesia*, *99*(1), 132–138. https://doi.org/10.1093/BJA/AEM144

Ho, R., Sances, S., Gowing, G., Amoroso, M. W., O'Rourke, J. G., Sahabian, A., Wichterle, H., Baloh, R. H., Sareen, D., & Svendsen, C. N. (2016). ALS disrupts spinal motor neuron maturation and aging pathways within gene co-expression networks. *Nature Neuroscience*, *19*(9), 1256. https://doi.org/10.1038/NN.4345

Hollenbeck, P. J. (1993). Products of endocytosis and autophagy are retrieved from axons by regulated retrograde organelle transport. *Journal of Cell Biology*, *121*(2), 305–315. https://doi.org/10.1083/JCB.121.2.305

Hörner, S. J., Couturier, N., Bruch, R., Koch, P., Hafner, M., & Rudolf, R. (2021). Hipsc-derived schwann cells influence myogenic differentiation in neuromuscular cocultures. *Cells*, *10*(12). https://doi.org/10.3390/CELLS10123292/S1

Iguchi, Y., Eid, L., Parent, M., Soucy, G., Bareil, C., Riku, Y., Kawai, K., Takagi, S., Yoshida, M., Katsuno, M., Sobue, G., & Julien, J. P. (2016). Exosome secretion is a key pathway for clearance of pathological TDP-43. *Brain : A Journal of Neurology*, *139*(Pt 12), 3187–3201. https://doi.org/10.1093/BRAIN/AWW237

Jablonka, S., & Sendtner, M. (2017). Developmental regulation of SMN expression: pathophysiological implications and perspectives for therapy development in spinal muscular atrophy. *Gene Therapy 2017 24:9*, *24*(9), 506–513. https://doi.org/10.1038/gt.2017.46

Jami, M. S., Salehi-Najafabadi, Z., Ahmadinejad, F., Hoedt, E., Chaleshtori, M. H., Ghatrehsamani, M., Neubert, T. A., Larsen, J. P., & Møller, S. G. (2015). Edaravone leads to proteome changes indicative of neuronal cell protection in response to oxidative stress. *Neurochemistry International*, *90*, 134–141. https://doi.org/10.1016/J.NEUINT.2015.07.024

Jerath, N. U., & Shy, M. E. (2015). Hereditary motor and sensory neuropathies: Understanding molecular pathogenesis could lead to future treatment strategies. *Biochimica et Biophysica Acta*, *1852*(4), 667–678. https://doi.org/10.1016/J.BBADIS.2014.07.031

Jing, K., & Lim, K. (2012). Why is autophagy important in human diseases? *Experimental & Molecular Medicine*, *44*(2), 69. https://doi.org/10.3858/EMM.2012.44.2.028

Jiwlawat, N., Lynch, E., Jeffrey, J., Van Dyke, J. M., & Suzuki, M. (2018). Current progress and challenges for skeletal muscle differentiation from human pluripotent stem cells using transgene-free approaches. *Stem Cells International*, *2018*. https://doi.org/10.1155/2018/6241681

Jones, R. A., Harrison, C., Eaton, S. L., Llavero Hurtado, M., Graham, L. C., Alkhammash, L., Oladiran, O. A., Gale, A., Lamont, D. J., Simpson, H., Simmen, M. W., Soeller, C., Wishart, T. M., & Gillingwater, T. H. (2017). Cellular and Molecular Anatomy of the Human Neuromuscular Junction. *Cell Reports*, *21*(9), 2348–2356. https://doi.org/10.1016/j.celrep.2017.11.008

Juntunen, J., & Teräväinen, H. (1972). Structural development of myoneural junctions in the human embryo. *Histochemie*, *32*(2), 107–112. https://doi.org/10.1007/BF00303726/METRICS

Kang, S., Son, S. M., Baik, S. H., Yang, J., Mook-Jung, I., & Kim, B. (2019). Autophagy-Mediated Secretory Pathway is Responsible for Both Normal and Pathological Tau in Neurons. *Journal of Alzheimer's Disease*, *70*(3), 667–680. https://doi.org/10.3233/JAD-190180

Kaur, S. J., McKeown, S. R., & Rashid, S. (2016). Mutant SOD1 mediated pathogenesis of Amyotrophic Lateral Sclerosis. *Gene*, *577*(2), 109–118. https://doi.org/10.1016/J.GENE.2015.11.049

Kiel, J. A. K. W. (2010). Autophagy in unicellular eukaryotes. *Philosophical Transactions of the Royal Society B: Biological Sciences*, *365*(1541), 819. https://doi.org/10.1098/RSTB.2009.0237

Kim, G., Gautier, O., Tassoni-Tsuchida, E., Ma, X. R., & Gitler, A. D. (2020). ALS Genetics: Gains, Losses, and Implications for Future Therapies. *Neuron*, *108*(5), 822–842. https://doi.org/10.1016/j.neuron.2020.08.022

Kim, H. J., Hong, Y. Bin, Park, J. M., Choi, Y. R., Kim, Y. J., Yoon, B. R., Koo, H., Yoo, J. H., Kim, S. B., Park, M., Chung, K. W., & Choi, B. O. (2013). Mutations in the PLEKHG5 gene is relevant with autosomal recessive intermediate Charcot-Marie-Tooth disease. *Orphanet Journal of Rare Diseases*, *8*(1), 1–11. https://doi.org/10.1186/1750-1172-8-104/FIGURES/5

Kim, J., Gee, H. Y., & Lee, M. G. (2018). Unconventional protein secretion - new insights into the pathogenesis and therapeutic targets of human diseases. *Journal of Cell Science*, *131*(12). https://doi.org/10.1242/JCS.213686

Komuro, R., Sasaki, T., Takaishi, K., Orita, S., & Takai, Y. (1996). Involvement of Rho and Rac small G proteins and Rho GDI in Ca2+-dependent exocytosis from PC12 cells. *Genes to Cells*, *1*(10), 943–951. https://doi.org/10.1046/J.1365-2443.1996.760276.X

Kowluru, A., Li, G., Rabaglia, M. E., Segu, V. B., Hofmann, F., Aktories, K., & Metz, S. A. (1997). Evidence for Differential Roles of the Rho Subfamily of GTP-Binding Proteins in Glucose- and Calcium-Induced Insulin Secretion from Pancreatic β Cells. *Biochemical Pharmacology*, *54*(10), 1097–1108. https://doi.org/10.1016/S0006-2952(97)00314-6

Kumar Jaiswal, M., & Jaiswal, K. (2019). Riluzole and edaravone: A tale of two amyotrophic lateral sclerosis drugs. *Medicinal Research Reviews*, *39*(2), 733–748. https://doi.org/10.1002/MED.21528

Lamark, T., & Johansen, T. (2012). Aggrephagy: Selective Disposal of Protein Aggregates by Macroautophagy. *International Journal of Cell Biology*, *2012*. https://doi.org/10.1155/2012/736905

Lamb, C. A., Yoshimori, T., & Tooze, S. A. (2013). The autophagosome: origins unknown, biogenesis complex. *Nature Reviews Molecular Cell Biology 2013 14:12*, *14*(12), 759–774. https://doi.org/10.1038/nrm3696

Lamptey, R. N. L., Chaulagain, B., Trivedi, R., Gothwal, A., Layek, B., & Singh, J. (2022). A Review of the Common Neurodegenerative Disorders: Current Therapeutic Approaches and the Potential Role of Nanotherapeutics. *International Journal of Molecular Sciences*, *23*(3). https://doi.org/10.3390/IJMS23031851

Landrieu, P., Baets, J., & De Jonghe, P. (2013). Hereditary motor-sensory, motor, and sensory neuropathies in childhood. *Handbook of Clinical Neurology*, *113*, 1413–1432. https://doi.org/10.1016/B978-0-444-59565-2.00011-3

Lathuiliere, A., Vernet, R., Charrier, E., Urwyler, M., Von Rohr, O., Belkouch, M. C., Saingier, V., Bouvarel, T., Guillarme, D., Engel, A., Salmon, P., Laumonier, T., Grogg, J., & Mach, N. (2022). Immortalized human myoblast cell lines for the delivery of therapeutic proteins using encapsulated cell technology. *Molecular Therapy - Methods and Clinical Development*, *26*, 441–458. https://doi.org/10.1016/j.omtm.2022.07.017

Lee, Y. il, Cacciani, N., Wen, Y., Zhang, X., Hedström, Y., Thompson, W., & Larsson, L. (2023). Direct electrical stimulation impacts on neuromuscular junction morphology on both stimulated and unstimulated contralateral soleus. *Journal of Cachexia, Sarcopenia and Muscle*, *14*(3), 1533. https://doi.org/10.1002/JCSM.13235

Luigetti, M., Conte, A., Madia, F., Marangi, G., Zollino, M., Mancuso, I., Dileone, M., Del Grande, A., Di Lazzaro, V., Tonali, P. A., & Sabatelli, M. (2009). Heterozygous SOD1 D90A mutation presenting as slowly progressive predominant upper motor neuron amyotrophic lateral sclerosis. *Neurological Sciences*, *30*(6), 517–520. https://doi.org/10.1007/S10072-009-0125-8/FIGURES/2

Lüningschrör, P., Binotti, B., Dombert, B., Heimann, P., Perez-Lara, A., Slotta, C., Thau-Habermann, N., Von Collenberg, C. R., Karl, F., Damme, M., Horowitz, A., Maystadt, I., Füchtbauer, A., Füchtbauer, E. M., Jablonka, S., Blum, R., Üçeyler, N., Petri, S., Kaltschmidt, B., … Sendtner, M. (2017). Plekhg5-regulated autophagy of synaptic vesicles reveals a pathogenic mechanism in motoneuron disease. *Nature Communications*, *8*(1). https://doi.org/10.1038/S41467-017-00689-Z

Lynch-Day, M. A., Mao, K., Wang, K., Zhao, M., & Klionsky, D. J. (2012). The role of autophagy in Parkinson's disease. *Cold Spring Harbor Perspectives in Medicine*, *2*(4). https://doi.org/10.1101/CSHPERSPECT.A009357

Maday, S., & Holzbaur, E. L. F. (2014). Autophagosome biogenesis in primary neurons follows an ordered and spatially regulated pathway. *Developmental Cell*, *30*(1), 71. https://doi.org/10.1016/J.DEVCEL.2014.06.001

Maday, S., Twelvetrees, A. E., Moughamian, A. J., & Holzbaur, E. L. F. (2014). AXONAL TRANSPORT: CARGO-SPECIFIC MECHANISMS OF MOTILITY AND REGULATION. *Neuron*, *84*(2), 292. https://doi.org/10.1016/J.NEURON.2014.10.019

Madden, D. R. (2002). Ion channel structure: The structure and function of glutamate receptor ion channels. *Nature Reviews Neuroscience*, *3*(2), 91–101. https://doi.org/10.1038/nrn725

Maffioletti, S. M., Sarcar, S., Henderson, A. B. H., Mannhardt, I., Pinton, L., Moyle, L. A., Steele-Stallard, H., Cappellari, O., Wells, K. E., Ferrari, G., Mitchell, J. S., Tyzack, G. E., Kotiadis, V. N., Khedr, M., Ragazzi, M., Wang, W., Duchen, M. R., Patani, R., Zammit, P. S., … Tedesco, F. S. (2018). Three-Dimensional Human iPSC-Derived Artificial Skeletal Muscles Model Muscular Dystrophies and Enable Multilineage Tissue Engineering. *Cell Reports*, *23*(3), 899. https://doi.org/10.1016/J.CELREP.2018.03.091

Mamchaoui, K., Trollet, C., Bigot, A., Negroni, E., Chaouch, S., Wolff, A., Kandalla, P. K., Marie, S., Di Santo, J., St Guily, J. L., Muntoni, F., Kim, J., Philippi, S., Spuler, S., Levy, N., Blumen, S. C., Voit, T., Wright, W. E., Aamiri, A., … Mouly, V. (2011). Immortalized pathological human myoblasts: Towards a universal tool for the study of neuromuscular disorders. *Skeletal Muscle*, *1*(1), 1–11. https://doi.org/10.1186/2044-5040-1-34/FIGURES/4

Manjithaya, R., Anjard, C., Loomis, W. F., & Subramani, S. (2010). Unconventional secretion of Pichia pastoris Acb1 is dependent on GRASP protein, peroxisomal functions, and autophagosome formation. *Journal of Cell Biology*, *188*(4), 537–546. https://doi.org/10.1083/JCB.200911149

Marino, M., Papa, S., Crippa, V., Nardo, G., Peviani, M., Cheroni, C., Trolese, M. C., Lauranzano, E., Bonetto, V., Poletti, A., DeBiasi, S., Ferraiuolo, L., Shaw, P. J., & Bendotti, C. (2015). Differences in protein quality control correlate with phenotype variability in 2 mouse models of familial amyotrophic lateral sclerosis. *Neurobiology of Aging*, *36*(1), 492–504. https://doi.org/10.1016/J.NEUROBIOLAGING.2014.06.026

Marklund, S. L., Andersen, P. M., Forsgren, L., Nilsson, P., Ohlsson, P. I., Wikander, G., & Öberg, A. (1997). Normal Binding and Reactivity of Copper in Mutant Superoxide Dismutase Isolated from Amyotrophic Lateral Sclerosis Patients. *Journal of Neurochemistry*, *69*(2), 675–681. https://doi.org/10.1046/J.1471-4159.1997.69020675.X

Martinou, J. C., & Merlie, J. P. (1991). Nerve-dependent modulation of acetylcholine receptor epsilon-subunit gene expression. *Journal of Neuroscience*, *11*(5), 1291–1299. https://doi.org/10.1523/JNEUROSCI.11-05-01291.1991

Marx, R., Henderson, J., Wang, J., & Baraban, J. M. (2005). Tech: a RhoA GEF selectively expressed in hippocampal and cortical neurons. *Journal of Neurochemistry*, *92*(4), 850–858. https://doi.org/10.1111/J.1471-4159.2004.02930.X

Massih, B., Veh, A., Schenke, M., Mungwa, S., Seeger, B., Selvaraj, B. T., Chandran, S., Reinhardt, P., Sterneckert, J., Hermann, A., Sendtner, M., & Lüningschrör, P. (2023). A 3D cell culture system for bioengineering human neuromuscular junctions to model ALS. *Frontiers in Cell and Developmental Biology*, *11*, 67. https://doi.org/10.3389/FCELL.2023.996952/BIBTEX

Maury, Y., Côme, J., Piskorowski, R. A., Salah-Mohellibi, N., Chevaleyre, V., Peschanski, M., Martinat, C., & Nedelec, S. (2014). Combinatorial analysis of developmental cues efficiently converts human pluripotent stem cells into multiple neuronal subtypes. *Nature Biotechnology*, *33*(1), 89–96. https://doi.org/10.1038/NBT.3049

Maystadt, I., Rezsöhazy, R., Barkats, M., Duque, S., Vannuffel, P., Remacle, S., Lambert, B., Najimi, M., Sokal, E., Munnich, A., Viollet, L., & Verellen-Dumoulin, C. (2007). The Nuclear Factor κB–Activator Gene PLEKHG5 Is Mutated in a Form of Autosomal Recessive Lower Motor Neuron Disease with Childhood Onset. *American Journal of Human Genetics*, *81*(1), 67. https://doi.org/10.1086/518900

McCord, J. M., & Fridovich, I. (1969). Superoxide Dismutase: AN ENZYMIC FUNCTION FOR ERYTHROCUPREIN (HEMOCUPREIN). *Journal of Biological Chemistry*, *244*(22), 6049–6055. https://doi.org/10.1016/S0021-9258(18)63504-5

McGonigle, P., & Ruggeri, B. (2014). Animal models of human disease: challenges in enabling translation. *Biochemical Pharmacology*, *87*(1), 162–171. https://doi.org/10.1016/J.BCP.2013.08.006

Mejzini, R., Flynn, L. L., Pitout, I. L., Fletcher, S., Wilton, S. D., & Akkari, P. A. (2019). ALS Genetics, Mechanisms, and Therapeutics: Where Are We Now? *Frontiers in Neuroscience*, *13*, 1310. https://doi.org/10.3389/FNINS.2019.01310/BIBTEX

Menzies, F. M., Fleming, A., & Rubinsztein, D. C. (2015). Compromised autophagy and neurodegenerative diseases. *Nature Reviews. Neuroscience*, *16*(6), 345–357. https://doi.org/10.1038/NRN3961

Mercuri, E., Darras, B. T., Chiriboga, C. A., Day, J. W., Campbell, C., Connolly, A. M., Iannaccone, S. T., Kirschner, J., Kuntz, N. L., Saito, K., Shieh, P. B., Tulinius, M., Mazzone, E. S., Montes, J., Bishop, K. M., Yang, Q., Foster, R., Gheuens, S., Bennett, C. F., … Finkel, R. S. (2018). Nusinersen versus Sham Control in Later-Onset Spinal Muscular Atrophy. *New England Journal of Medicine*, *378*(7), 625–635. https://doi.org/10.1056/NEJMOA1710504/SUPPL_FILE/NEJMOA1710504_DISCLOSURES.PDF

Missias, A. C., Chu, G. C., Klocke, B. J., Sanes, J. R., & Merlie, J. P. (1996). Maturation of the acetylcholine receptor in skeletal muscle: Regulation of the AChR γ-to-ε switch. *Developmental Biology*, *179*(1), 223–238. https://doi.org/10.1006/dbio.1996.0253

Mizushima, N. (2007). Autophagy: process and function. *Genes & Development*, *21*(22), 2861–2873. https://doi.org/10.1101/GAD.1599207

Mizushima, N., Yoshimori, T., & Ohsumi, Y. (2011). The Role of Atg Proteins in Autophagosome Formation. *Https://Doi.Org/10.1146/Annurev-Cellbio-092910-154005*, *27*, 107–132. https://doi.org/10.1146/ANNUREV-CELLBIO-092910-154005

Muppirala, A. N., Limbach, L. E., Bradford, E. F., & Petersen, S. C. (2021). Schwann cell development: From neural crest to myelin sheath. *Wiley Interdisciplinary Reviews: Developmental Biology*, *10*(5). https://doi.org/10.1002/WDEV.398

Murray, L. M., Talbot, K., & Gillingwater, T. H. (2010). Review: neuromuscular synaptic vulnerability in motor neurone disease: amyotrophic lateral sclerosis and spinal muscular atrophy. *Neuropathology and Applied Neurobiology*, *36*(2), 133–156. https://doi.org/10.1111/J.1365-2990.2010.01061.X

Naguib, M., Flood, P., McArdle, J. J., & Brenner, H. R. (2002). Advances in neurobiology of the neuromuscular junction: implications for the anesthesiologist. *Anesthesiology*, *96*(1), 202–231. https://doi.org/10.1097/00000542-200201000-00035

Natarajan, A., Sethumadhavan, A., & Krishnan, U. M. (2019). *Toward Building the Neuromuscular Junction: In Vitro Models To Study Synaptogenesis and Neurodegeneration*. https://doi.org/10.1021/acsomega.9b00973

New, J., & Thomas, S. M. (2019). Autophagy-dependent secretion: mechanism, factors secreted, and disease implications. *Autophagy*, *15*(10), 1682. https://doi.org/10.1080/15548627.2019.1596479

Nilsson, P., Loganathan, K., Sekiguchi, M., Matsuba, Y., Hui, K., Tsubuki, S., Tanaka, M., Iwata, N., Saito, T., & Saido, T. C. (2013). Aβ Secretion and Plaque Formation Depend on Autophagy. *Cell Reports*, *5*(1), 61–69. https://doi.org/10.1016/j.celrep.2013.08.042

Nishitoh, H., Kadowaki, H., Nagai, A., Maruyama, T., Yokota, T., Fukutomi, H., Noguchi, T., Matsuzawa, A., Takeda, K., & Ichijo, H. (2008). ALS-linked mutant SOD1 induces ER stress- and ASK1-dependent motor neuron death by targeting Derlin-1. *Genes & Development*, *22*(11), 1451. https://doi.org/10.1101/GAD.1640108

Numberger, M., Dürr, I., Kues, W., Koenen, M., & Witzemann, V. (1991). Different mechanisms regulate muscle-specific AChR gamma- and epsilon-subunit gene expression. *EMBO Journal*, *10*(10), 2957–2964.

Ogata, T. (1988). Structure of motor endplates in the different fiber types of vertebrate skeletal muscles. *Archives of Histology and Cytology*, *51*(5), 385–424. https://doi.org/10.1679/AOHC.51.385

Osaki, T., Uzel, S. G. M., & Kamm, R. D. (2018). Microphysiological 3D model of amyotrophic lateral sclerosis (ALS) from human iPS-derived muscle cells and optogenetic motor neurons. *Science Advances*, *4*(10). https://doi.org/10.1126/SCIADV.AAT5847

Osaki, T., Uzel, S. G. M., & Kamm, R. D. (2020). On-chip 3D neuromuscular model for drug screening and precision medicine in neuromuscular disease. *Nature Protocols*, *15*(2), 421–449. https://doi.org/10.1038/s41596-019-0248-1

Özoğuz, A., Uyan, Ö., Birdal, G., Iskender, C., Kartal, E., Lahut, S., Ömür, Ö., Agim, Z. S., Eken, A. G., Sen, N. E., Kavak, P., Saygi, C., Sapp, P. C., Keagle, P., Parman, Y., Tan, E., Koç, F., Deymeer, F., Oflazer, P., … Başak, A. N. (2015). The distinct genetic pattern of ALS in Turkey and novel mutations. *Neurobiology of Aging*, *36*(4), 1764.e9-1764.e18. https://doi.org/10.1016/j.neurobiolaging.2014.12.032

Pansarasa, O., Bordoni, M., Diamanti, L., Sproviero, D., Gagliardi, S., & Cereda, C. (2018). SOD1 in Amyotrophic Lateral Sclerosis: "Ambivalent" Behavior Connected to the Disease. *International Journal of Molecular Sciences*, *19*(5). https://doi.org/10.3390/IJMS19051345

Patel, T., Hammelman, J., Aziz, S., Jang, S., Closser, M., Michaels, T. L., Blum, J. A., Gifford, D. K., & Wichterle, H. (2022). Transcriptional dynamics of murine motor neuron maturation in vivo and in vitro. *Nature Communications*, *13*(1). https://doi.org/10.1038/S41467-022-33022-4

Peggion, C., Scalcon, V., Massimino, M. L., Nies, K., Lopreiato, R., Rigobello, M. P., & Bertoli, A. (2022). SOD1 in ALS: Taking Stock in Pathogenic Mechanisms and the Role of Glial and Muscle Cells. *Antioxidants*, *11*(4). https://doi.org/10.3390/ANTIOX11040614

Pereira, J. D., DuBreuil, D. M., Devlin, A. C., Held, A., Sapir, Y., Berezovski, E., Hawrot, J., Dorfman, K., Chander, V., & Wainger, B. J. (2021). Human sensorimotor organoids derived from healthy and amyotrophic lateral sclerosis stem cells form neuromuscular junctions. *Nature Communications 2021 12:1*, *12*(1), 1–17. https://doi.org/10.1038/s41467-021-24776-4

Perrin, S. (2014). Preclinical research: Make mouse studies work. *Nature 2014 507:7493*, *507*(7493), 423–425. https://doi.org/10.1038/507423a

Peterson, E. R., & Crain, S. M. (1970). Innervation in cultures of fetal rodent skeletal muscle by organotypic explants of spinal cord from different animals. *Zeitschrift Für Zellforschung Und Mikroskopische Anatomie*, *106*(1), 1–21. https://doi.org/10.1007/BF01027714/METRICS

Pinton, L., Khedr, M., Lionello, V. M., Maoletti, S. M., Khokhar, N., Counsell, J. R., Free, R., Andreia, H., Bernardo, S., & Tedesco, F. S. (2022). *3D Human Induced Pluripotent Stem Cell-derived Bioengineered Skeletal Muscles for Tissue, Disease and Therapy Modelling*. https://doi.org/10.21203/RS.3.PEX-2034/V1

Piotrkiewicz, M., & Hausmanowa-Petrusewicz, I. (2013). Amyotrophic lateral sclerosis: A dying motor unit? *Frontiers in Aging Neuroscience*, *5*(MAR), 7. https://doi.org/10.3389/FNAGI.2013.00007/BIBTEX

Ponpuak, M., Mandell, M. A., Kimura, T., Chauhan, S., Cleyrat, C., & Deretic, V. (2015). Secretory autophagy. *Current Opinion in Cell Biology*, *35*, 106. https://doi.org/10.1016/J.CEB.2015.04.016

Porras, M. A. G., Sieck, G. C., & Mantilla, C. B. (2018). Impaired Autophagy in Motor Neurons: A Final Common Mechanism of Injury and Death. *Physiology*, *33*(3), 211. https://doi.org/10.1152/PHYSIOL.00008.2018

Powell, R., & Phillips, J. B. (2021). Engineered Tissues Made from Human iPSC-Derived Schwann Cells for Investigating Peripheral Nerve Regeneration In Vitro. *Methods in Molecular Biology (Clifton, N.J.)*, *2269*, 245–254. https://doi.org/10.1007/978-1-0716-1225-5_17

Pratt, S. J. P., Valencia, A. P., Le, G. K., Shah, S. B., & Lovering, R. M. (2015). Pre- and postsynaptic changes in the neuromuscular junction in dystrophic mice. *Frontiers in Physiology*, *6*(SEP), 252. https://doi.org/10.3389/FPHYS.2015.00252

Puttonen, K. A., Ruponen, M., Naumenko, N., Hovatta, O. H., Tavi, P., & Koistinaho, J. (2015). Generation of functional neuromuscular junctions from human pluripotent stem cell lines. *Frontiers in Cellular Neuroscience*, *9*(DEC), 1–9. https://doi.org/10.3389/FNCEL.2015.00473/BIBTEX

Rabouille, C., Malhotra, V., & Nickel, W. (2012). Diversity in unconventional protein secretion. *Journal of Cell Science*, *125*(22), 5251–5255. https://doi.org/10.1242/JCS.103630

Rakhit, R., Robertson, J., Velde, C. Vande, Horne, P., Ruth, D. M., Griffin, J., Cleveland, D. W., Cashman, N. R., & Chakrabartty, A. (2007). An immunological epitope selective for pathological monomer-misfolded SOD1 in ALS. *Nature Medicine*, *13*(6), 754–759. https://doi.org/10.1038/NM1559

Ramesh, N., & Pandey, U. B. (2017). Autophagy Dysregulation in ALS: When Protein Aggregates Get Out of Hand. *Frontiers in Molecular Neuroscience*, *10*. https://doi.org/10.3389/FNMOL.2017.00263

Reinhardt, P., Glatza, M., Hemmer, K., Tsytsyura, Y., Thiel, C. S., Höing, S., Moritz, S., Parga, J. A., Wagner, L., Bruder, J. M., Wu, G., Schmid, B., Röpke, A., Klingauf, J., Schwamborn, J. C., Gasser, T., Schöler, H. R., & Sterneckert, J. (2013). Derivation and Expansion Using Only Small Molecules of Human Neural Progenitors for Neurodegenerative Disease Modeling. *PLoS ONE*, *8*(3), e59252. https://doi.org/10.1371/journal.pone.0059252

Renton, A. E., Majounie, E., Waite, A., Simón-Sánchez, J., Rollinson, S., Gibbs, J. R., Schymick, J. C., Laaksovirta, H., van Swieten, J. C., Myllykangas, L., Kalimo, H., Paetau, A., Abramzon, Y., Remes, A. M., Kaganovich, A., Scholz, S. W., Duckworth, J., Ding, J., Harmer, D. W., … Traynor, B. J. (2011). A hexanucleotide repeat expansion in C9ORF72 is the cause of chromosome 9p21-linked ALS-FTD. *Neuron*, *72*(2), 257. https://doi.org/10.1016/J.NEURON.2011.09.010

Rodríguez-Muela, N. (2020). Autophagy in motor neuron diseases. *Progress in Molecular Biology and Translational Science*, *172*, 157–202. https://doi.org/10.1016/BS.PMBTS.2020.03.009

Rosen, D. R., Siddiquet, T., Pattersont, D., Figlewicz, D. A., Sapp, P., Hentatit, A., Donaldsont, D., Goto, J., O, J. P., Dengt, H.-X., Rahmanit, Z., Krizus, A., McKenna-Yasek, D., Cayabyabt, A., Gaston, S. M., Bergert, R., Tanzi, R. E., Halperin, J. J., Herzfeldtt, B., … Brown Jr, R. H. (1993). *Mutations in Cu/Zn superoxide dismutase gene are associated with familial amyotrophic lateral sclerosis*.

Rudnick, N. D., Griffey, C. J., Guarnieri, P., Gerbino, V., Wang, X., Piersaint, J. A., Tapia, J. C., Rich, M. M., & Maniatis, T. (2017). Distinct roles for motor neuron autophagy early and late in the SOD1G93A mouse model of ALS. *Proceedings of the National Academy of Sciences of the United States of America*, *114*(39), E8294–E8303. https://doi.org/10.1073/PNAS.1704294114

Sances, S., Bruijn, L. I., Chandran, S., Eggan, K., Ho, R., Klim, J. R., Livesey, M. R., Lowry, E., Macklis, J. D., Rushton, D., Sadegh, C., Sareen, D., Wichterle, H., Zhang, S. C., & Svendsen, C. N. (2016). Modeling ALS using motor neurons derived from human induced pluripotent stem cells. *Nature Neuroscience*, *19*(4), 542. https://doi.org/10.1038/NN.4273

Sanes, J. R., & Lichtman, J. W. (1999). DEVELOPMENT OF THE VERTEBRATE NEUROMUSCULAR JUNCTION. In *Annu. Rev. Neurosci* (Vol. 22). www.annualreviews.org

Santhanam, N., Kumanchik, L., Guo, X., Sommerhage, F., Cai, Y., Jackson, M., Martin, C., Saad, G., McAleer, C. W., Wang, Y., Lavado, A., Long, C. J., & Hickman, J. J. (2018). Stem cell derived phenotypic human neuromuscular junction model for dose response evaluation of therapeutics. *Biomaterials*, *166*, 64. https://doi.org/10.1016/J.BIOMATERIALS.2018.02.047

Santosa, K. B., Keane, A. M., Jablonka-Shariff, A., Vannucci, B., & Snyder-Warwick, A. K. (2018a). Clinical Relevance of Terminal Schwann Cells: An Overlooked Component of the Neuromuscular Junction. *Journal of Neuroscience Research*, *96*(7), 1125. https://doi.org/10.1002/JNR.24231

Santosa, K. B., Keane, A. M., Jablonka-Shariff, A., Vannucci, B., & Snyder-Warwick, A. K. (2018b). Clinical relevance of terminal Schwann cells: An overlooked component of the neuromuscular junction. In *Journal of Neuroscience Research* (Vol. 96, Issue 7, pp. 1125–1135). John Wiley and Sons Inc. https://doi.org/10.1002/jnr.24231

Sattler, R., & Tymianski, M. (2001). Molecular mechanisms of glutamate receptor-mediated excitotoxic neuronal cell death. *Molecular Neurobiology 2001 24:1*, *24*(1), 107–129. https://doi.org/10.1385/MN:24:1-3:107

Schenke, M., Schjeide, B. M., Püschel, G. P., & Seeger, B. (2020). Analysis of motor neurons differentiated from human induced pluripotent stem cells for the use in cell-based botulinum neurotoxin activity assays. *Toxins*, *12*(5). https://doi.org/10.3390/TOXINS12050276

Schuetze, S. M., & Role, L. W. (2003). Developmental Regulation of Nicotinic Acetylcholine Receptors. *Http://Dx.Doi.Org/10.1146/Annurev.Ne.10.030187.002155*, *Vol. 10*, 403–457. https://doi.org/10.1146/ANNUREV.NE.10.030187.002155

Selvaraj, S., Mondragon-Gonzalez, R., Xu, B., Magli, A., Kim, H., Lainé, J., Kiley, J., McKee, H., Rinaldi, F., Aho, J., Tabti, N., Shen, W., & Perlingeiro, R. C. (2019). Screening identifies small molecules that enhance the maturation of human pluripotent stem cell-derived myotubes. *ELife*, *8*. https://doi.org/10.7554/ELIFE.47970

Senderek, J. (2021). PLEKHG5: Merging phenotypes and disease mechanisms in Charcot-Marie-Tooth neuropathy and lower motor neuron disease. *European Journal of Neurology*, *28*(4), 1106–1107. https://doi.org/10.1111/ENE.14752

Sharma, V., Verma, S., Seranova, E., Sarkar, S., & Kumar, D. (2018). Selective Autophagy and Xenophagy in Infection and Disease. *Frontiers in Cell and Developmental Biology*, *6*(NOV). https://doi.org/10.3389/FCELL.2018.00147

Shelby, E.-S., & Mirea, A. (2021). INNOVATIVE THERAPIES IN GENETIC DISEASES: SPINAL MUSCULAR ATROPHY. *Romanian Journal of Pediatrics*, *70*(2), 108–113. https://doi.org/10.37897/RJP.2021.2.4

Shi, Y., Inoue, H., Wu, J. C., & Yamanaka, S. (2017). Induced pluripotent stem cell technology: a decade of progress. *Nature Reviews. Drug Discovery*, *16*(2), 115. https://doi.org/10.1038/NRD.2016.245

Simon, C. M., Jablonka, S., Ruiz, R., Tabares, L., & Sendtner, M. (2010). Ciliary neurotrophic factor-induced sprouting preserves motor function in a mouse model of mild spinal muscular atrophy. *Human Molecular Genetics*, *19*(6), 973–986. https://doi.org/10.1093/HMG/DDP562

Slater, C. R. (2017). The structure of human neuromuscular junctions: Some unanswered molecular questions. *International Journal of Molecular Sciences*, *18*(10). https://doi.org/10.3390/ijms18102183

Smith, A. S. T., Passey, S. L., Martin, N. R. W., Player, D. J., Mudera, V., Greensmith, L., & Lewis, M. P. (2016). Creating Interactions between Tissue-Engineered Skeletal Muscle and the Peripheral Nervous System. *Cells, Tissues, Organs*, *202*(3–4), 143. https://doi.org/10.1159/000443634

Son, Y. J., Trachtenberg, J. T., & Thompson, W. J. (1996). Schwann cells induce and guide sprouting and reinnervation of neuromuscular junctions. *Trends in Neurosciences*, *19*(7), 280–285. https://doi.org/10.1016/S0166-2236(96)10032-1

Sproviero, D., La Salvia, S., Giannini, M., Crippa, V., Gagliardi, S., Bernuzzi, S., Diamanti, L., Ceroni, M., Pansarasa, O., Poletti, A., & Cereda, C. (2018). Pathological proteins are transported by extracellular vesicles of sporadic amyotrophic lateral sclerosis patients. *Frontiers in Neuroscience*, *12*(JUL), 487. https://doi.org/10.3389/FNINS.2018.00487/BIBTEX

Stavrou, M., Kagiava, A., Sargiannidou, I., Georgiou, E., & Kleopa, K. A. (2023). Charcot–Marie–Tooth neuropathies: Current gene therapy advances and the route toward translation. *Journal of the Peripheral Nervous System*, *28*(2), 150–168. https://doi.org/10.1111/JNS.12543

Steinbeck, J. A., Jaiswal, M. K., Calder, E. L., Kishinevsky, S., Weishaupt, A., Toyka, K. V., Goldstein, P. A., & Studer, L. (2016). Functional Connectivity under Optogenetic Control Allows Modeling of Human Neuromuscular Disease. *Cell Stem Cell*, *18*(1), 134–143. https://doi.org/10.1016/J.STEM.2015.10.002

Stifani, N. (2014). Motor neurons and the generation of spinal motor neuron diversity. *Frontiers in Cellular Neuroscience*, *8*(OCT), 293. https://doi.org/10.3389/FNCEL.2014.00293/BIBTEX

Stojkovic, T. (2016). Hereditary neuropathies: An update. *Revue Neurologique*, *172*(12), 775–778. https://doi.org/10.1016/J.NEUROL.2016.06.007

Stoklund Dittlau, K., Krasnow, E. N., Fumagalli, L., Vandoorne, T., Baatsen, P., Kerstens, A., Giacomazzi, G., Pavie, B., Rossaert, E., Beckers, J., Sampaolesi, M., Van Damme, P., & Van Den Bosch, L. (2021). Human motor units in microfluidic devices are impaired by FUS mutations and improved by HDAC6 inhibition. *Stem Cell Reports*, *0*(0). https://doi.org/10.1016/j.stemcr.2021.03.029

Stolz, A., Ernst, A., & Dikic, I. (2014). Cargo recognition and trafficking in selective autophagy. *Nature Cell Biology*, *16*(6), 495–501. https://doi.org/10.1038/NCB2979

Suzuki, N., Nishiyama, A., Warita, H., & Aoki, M. (2022). Genetics of amyotrophic lateral sclerosis: seeking therapeutic targets in the era of gene therapy. *Journal of Human Genetics 2022 68:3*, *68*(3), 131–152. https://doi.org/10.1038/s10038-022-01055-8

Takahashi, K., Tanabe, K., Ohnuki, M., Narita, M., Ichisaka, T., Tomoda, K., & Yamanaka, S. (2007). Induction of pluripotent stem cells from adult human fibroblasts by defined factors. *Cell*, *131*(5), 861–872. https://doi.org/10.1016/J.CELL.2007.11.019

Takahashi, K., & Yamanaka, S. (2006). Induction of pluripotent stem cells from mouse embryonic and adult fibroblast cultures by defined factors. *Cell*, *126*(4), 663–676. https://doi.org/10.1016/J.CELL.2006.07.024

Takazawa, T., Croft, G. F., Amoroso, M. W., Studer, L., Wichterle, H., & MacDermott, A. B. (2012). Maturation of Spinal Motor Neurons Derived from Human Embryonic Stem Cells. *PLOS ONE*, *7*(7), e40154. https://doi.org/10.1371/JOURNAL.PONE.0040154

Tanida, I., Ueno, T., & Kominami, E. (2008). LC3 and Autophagy. *Methods in Molecular Biology (Clifton, N.J.)*, *445*, 77–88. https://doi.org/10.1007/978-1-59745-157-4_4

Tintignac, L. A., Brenner, H. R., & Rüegg, M. A. (2015). Mechanisms regulating neuromuscular junction development and function and causes of muscle wasting. *Physiological Reviews*, *95*(3), 809–852. https://doi.org/10.1152/PHYSREV.00033.2014/ASSET/IMAGES/LARGE/Z9J0031527310007.JPEG

Tortarolo, M., Grignaschi, G., Calvaresi, N., Zennaro, E., Spaltro, G., Colovic, M., Fracasso, C., Guiso, G., Elger, B., Schneider, H., Seilheimer, B., Caccia, S., & Bendotti, C. (2006). Glutamate AMPA receptors change in motor neurons of SOD1G93A transgenic mice and their inhibition by a noncompetitive antagonist ameliorates the progression of amytrophic lateral sclerosis-like disease. *Journal of Neuroscience Research*, *83*(1), 134–146. https://doi.org/10.1002/JNR.20715

Trajkovic, K., Jeong, H., & Krainc, D. (2017). Mutant Huntingtin Is Secreted via a Late Endosomal/Lysosomal Unconventional Secretory Pathway. *The Journal of Neuroscience*, *37*(37), 9000. https://doi.org/10.1523/JNEUROSCI.0118-17.2017

Underwood, R., Wang, B., Carico, C., Whitaker, R. H., Placzek, W. J., & Yacoubian, T. A. (2020). The GTPase Rab27b regulates the release, autophagic clearance, and toxicity of alpha-synuclein. *Journal of Biological Chemistry*, *295*(23), 8005–8016. https://doi.org/10.1074/JBC.RA120.013337/ATTACHMENT/AFAD3E97-D4BD-4AFC-9B96-EC3E165CB53E/MMC1.PDF

Valentine, J. S., & Hart, P. J. (2003). Bioinorganic Chemistry Special Feature: Misfolded CuZnSOD and amyotrophic lateral sclerosis. *Proceedings of the National Academy of Sciences of the United States of America*, *100*(7), 3617. https://doi.org/10.1073/PNAS.0730423100

Vilmont, V., Cadot, B., Ouanounou, G., & Gomes, E. R. (2016). A system for studying mechanisms of neuromuscular junction development and maintenance. *Development (Cambridge, England)*, *143*(13), 2464. https://doi.org/10.1242/DEV.130278

Wainger, B. J., Kiskinis, E., Mellin, C., Wiskow, O., Han, S. S. W., Sandoe, J., Perez, N. P., Williams, L. A., Lee, S., Boulting, G., Berry, J. D., Brown, R. H., Cudkowicz, M. E., Bean, B. P., Eggan, K., & Woolf, C. J. (2014). Intrinsic membrane hyperexcitability of amyotrophic lateral sclerosis patient-derived motor neurons. *Cell Reports*, *7*(1), 1–11. https://doi.org/10.1016/J.CELREP.2014.03.019

Wang, T., Martin, S., Papadopulos, A., Harper, C. B., Mavlyutov, T. A., Niranjan, D., Glass, N. R., Cooper-White, J. J., Sibarita, J. B., Choquet, D., Davletov, B., & Meunier, F. A. (2015). Control of Autophagosome Axonal Retrograde Flux by Presynaptic Activity Unveiled Using Botulinum Neurotoxin Type A. *The Journal of Neuroscience*, *35*(15), 6179. https://doi.org/10.1523/JNEUROSCI.3757-14.2015

Wee, C. D., Kong, L., & Sumner, C. J. (2010). The genetics of spinal muscular atrophies. *Current Opinion in Neurology*, *23*(5), 450–458. https://doi.org/10.1097/WCO.0B013E32833E1765

Wilson, D. M., Cookson, M. R., Van Den Bosch, L., Zetterberg, H., Holtzman, D. M., & Dewachter, I. (2023). Hallmarks of neurodegenerative diseases. *Cell*, *186*(4), 693–714. https://doi.org/10.1016/J.CELL.2022.12.032

Woodhoo, A., Alonso, M. B. D., Droggiti, A., Turmaine, M., D'Antonio, M., Parkinson, D. B., Wilton, D. K., Al-Shawi, R., Simons, P., Shen, J., Guillemot, F., Radtke, F., Meijer, D., Feltri, M. L., Wrabetz, L., Mirsky, R., & Jessen, K. R. (2009). Notch controls embryonic Schwann cell differentiation, postnatal myelination and adult plasticity. *Nature Neuroscience*, *12*(7), 839–847. https://doi.org/10.1038/NN.2323

Yamashita, S., & Ando, Y. (2015). Genotype-phenotype relationship in hereditary amyotrophic lateral sclerosis. *Translational Neurodegeneration*, *4*(1). https://doi.org/10.1186/S40035-015-0036-Y

Zaffagnini, G., & Martens, S. (2016). Mechanisms of Selective Autophagy. *Journal of Molecular Biology*, *428*(9 Pt A), 1714–1724. https://doi.org/10.1016/J.JMB.2016.02.004

Zarei, S., Carr, K., Reiley, L., Diaz, K., Guerra, O., Altamirano, P. F., Pagani, W., Lodin, D., Orozco, G., & Chinea, A. (2015). A comprehensive review of amyotrophic lateral sclerosis. *Surgical Neurology International*, *6*(1). https://doi.org/10.4103/2152-7806.169561

Zare-Shahabadi, A., Masliah, E., Johnson, G. V. W., & Rezaei, N. (2015). Autophagy in Alzheimer's disease. *Reviews in the Neurosciences*, *26*(4), 385–395. https://doi.org/10.1515/REVNEURO-2014-0076

Zhang, M., Kenny, S. J., Ge, L., Xu, K., & Schekman, R. (2015). Translocation of interleukin-1β into a vesicle intermediate in autophagy- mediated secretion. *ELife*, *4*(NOVEMBER2015). https://doi.org/10.7554/ELIFE.11205.001

Zou, Z. Y., Zhou, Z. R., Che, C. H., Liu, C. Y., He, R. L., & Huang, H. P. (2017). Genetic epidemiology of amyotrophic lateral sclerosis: A systematic review and meta-analysis. *Journal of Neurology, Neurosurgery and Psychiatry*, *88*(7), 540–549. https://doi.org/10.1136/JNNP-2016-315018

7 Manuscripts

7.1 Manuscript I: A 3D cell culture system for bioengineering human neuromuscular junctions to model ALS

frontiers | Frontiers in Cell and Developmental Biology

TYPE Brief Research Report
PUBLISHED 14 February 2023
DOI 10.3389/fcell.2023.996952

OPEN ACCESS

EDITED BY
Xianming Wang,
Institute of Diabetes and Regeneration Research, Germany

REVIEWED BY
Stefano Stifani,
McGill University, Canada Liam C. Hunt,
Rhodes College, United States

*CORRESPONDENCE
Patrick Lüningschrör, lueningsch_p@ukw.de

†Present address:
Peter Reinhardt, AbbVie Deutschland GmbH & Co. KG, Neuroscience Discovery, Ludwigshafen am Rhein, Germany

SPECIALTY SECTION
This article was submitted to Stem Cell Research,
a section of the journal
Frontiers in Cell and Developmental Biology

RECEIVED 18 July 2022
ACCEPTED 16 January 2023
PUBLISHED 14 February 2023

CITATION
Massih B, Veh A, Schenke M, Mungwa S, Seeger B, Selvaraj BT, Chandran S, Reinhardt P, Sterneckert J, Hermann A, Sendtner M and Lüningschrör P (2023), A 3D cell culture system for bioengineering human neuromuscular junctions to model ALS.
Front. Cell Dev. Biol. 11:996952. doi: 10.3389/fcell.2023.996952

A 3D cell culture system for bioengineering human neuromuscular junctions to model ALS

Bita Massih[1], Alexander Veh[1], Maren Schenke[2], Simon Mungwa[1], Bettina Seeger[2], Bhuvaneish T. Selvaraj[3,4,5], Siddharthan Chandran[3,4,5], Peter Reinhardt[6†], Jared Sterneckert[6,7], Andreas Hermann[8,9,10], Michael Sendtner[1] and Patrick Lüningschrör[1]*

[1]Institute of Clinical Neurobiology, University Hospital Würzburg, Würzburg, Germany, [2]Institute for Food Quality and Safety, Research Group Food Toxicology and Alternative/Complementary Methods to Animal Experiments, University of Veterinary Medicine Hannover, Hannover, Germany, [3]Centre for Clinical Brain Sciences, University of Edinburgh, Edinburgh, United Kingdom, [4]UK Dementia Research Institute at University of Edinburgh, University of Edinburgh, Edinburgh, United Kingdom, [5]Anne Rowling Regenerative Neurology Clinic, University of Edinburgh, Edinburgh, United Kingdom, [6]Center for Regenerative Therapies Dresden, Technische Universität Dresden, Dresden, Germany, [7]Medical Faculty Carl Gustav Carus of TU Dresden, Dresden, Germany, [8]Translational Neurodegeneration Section "Albrecht-Kossel", Department of Neurology, University Medical Center Rostock, Rostock, Germany, [9]Center for Transdisciplinary Neurosciences Rostock, University Medical Center Rostock, Rostock, Germany, [10]Deutsches Zentrum für Neurodegenerative Erkrankungen (DZNE) Rostock/Greifswald, Rostock, Germany

The signals that coordinate and control movement in vertebrates are transmitted from motoneurons (MNs) to their target muscle cells at neuromuscular junctions (NMJs). Human NMJs display unique structural and physiological features, which make them vulnerable to pathological processes. NMJs are an early target in the pathology of motoneuron diseases (MND). Synaptic dysfunction and synapse elimination precede MN loss suggesting that the NMJ is the starting point of the pathophysiological cascade leading to MN death. Therefore, the study of human MNs in health and disease requires cell culture systems that enable the connection to their target muscle cells for NMJ formation. Here, we present a human neuromuscular co-culture system consisting of induced pluripotent stem cell (iPSC)-derived MNs and 3D skeletal muscle tissue derived from myoblasts. We used self-microfabricated silicone dishes combined with Velcro hooks to support the formation of 3D muscle tissue in a defined extracellular matrix, which enhances NMJ function and maturity. Using a combination of immunohistochemistry, calcium imaging, and pharmacological stimulations, we characterized and confirmed the function of the 3D muscle tissue and the 3D neuromuscular co-cultures. Finally, we applied this system as an *in vitro* model to study the pathophysiology of Amyotrophic Lateral Sclerosis (ALS) and found a decrease in neuromuscular coupling and muscle contraction in co-cultures with MNs harboring ALS-linked *SOD1* mutation. In summary, the human 3D neuromuscular cell culture system presented here recapitulates aspects of human physiology in a controlled *in vitro* setting and is suitable for modeling of MND.

KEYWORDS

NMJ–neuromuscular junction, motoneuron (MN), skeletal muscle, iPSC (induced pluripotent stem cells), 3D cell culture

Introduction

Motoneurons (MNs) coordinate and control vertebrate movement by patterned electrical activity transmitted to skeletal muscle fibers to trigger their contraction. At neuromuscular junctions (NMJs), the MN axon terminates and interacts *via* chemical neurotransmitters with their target muscle cell. During neuromuscular transmission, MN activity causes the release of neurotransmitters from its terminals, which bind to postsynaptic receptors on the surface of their target cells to trigger a localized depolarization leading to muscle contraction (Li et al., 2018). NMJs have a unique morphology with a high degree of complexity on their presynaptic site. MN axons profoundly branch at their target site to contact many muscle fibers. These contact sites are highly specialized structures. The thin ending of the MN axon terminates as boutons from where the neurotransmitter is released (Li et al., 2018).

Although the principal organization of NMJs follows a similar blueprint, there are considerable inter-species differences (Jones et al., 2017; Boehm et al., 2020). A systematic comparative analysis between mouse and human NMJs revealed morphological differences, distinct synaptic proteomes, and distinct localization of the active zone proteins such as SNAP-25 (Jones et al., 2017). Compared to other vertebrate species, human NMJs are among the smallest known but with the most deeply infolded postsynaptic membrane (Jones et al., 2017; Slater, 2017; Boehm et al., 2020). From these morphological differences unique physiological properties arise, which need to be considered when studying pathological processes affecting the NMJ (Slater, 2017). In motoneuron diseases (MNDs) such as amyotrophic lateral sclerosis (ALS), NMJs become an early and vulnerable target, which represents the starting point of the pathological cascade leading to muscle atrophy and MN loss (Murray et al., 2010). This may explain the difficulty in translating studies based on ALS mouse models to clinical progress (Perrin, 2014; Clerc et al., 2016).

Thus, there is an urgent need to create cell culture models that reflect the human *in vivo* physiology as close as possible. So far, several approaches in generating models of neuromuscular circuits have been utilized (de Jongh et al., 2021). Initially, myofibers and induced pluripotent stem cell (iPSC)-derived MNs were co-cultured under 2D conditions to form NMJs (Demestre et al., 2015; Steinbeck et al., 2016). This was followed by work using compartmentalized 2D culture systems to ensure the maintenance of cell-type-specific microenvironments (Bellmann et al., 2019; Stoklund Dittlau et al., 2021). Such cell culture systems reflect the spatial separation of MN soma and axon terminal, which occurs *in vivo*. A more sophisticated 3D co-culture system was used to drive the maturation of the contractile apparatus reflected in the upregulation of the epsilon acetylcholine receptor (AChR) subunit (Afshar Bakooshli et al., 2019). The use of 3D muscle tissue in a compartmentalized system has also been described, but with a simplified protocol for creating muscle fibers (Osaki et al., 2018). Taken together, these studies show significant progress in the generation of 2D and 3D co-culture systems. However, the reproducibility of these methods and adaptation for MNs derived from different iPSC lines has not been shown.

The presented study aimed at establishing a 3D neuromuscular system with iPSC-derived MNs and myoblast-derived human skeletal muscle tissue. We decided to adopt the method described by Bakooshli et al. since it was the only study so far that provided evidence for adult NMJs *in vitro* (Afshar Bakooshli et al., 2019). We show an *in vitro* model that reproducibly generates the growth of MN axons within a 3D hydrogel resulting in the connection with myotubes and the formation of NMJs. Human skeletal myoblasts differentiate after 14 days to mature 3D muscle tissue. We confirmed muscle function by acetylcholine (ACh)-induced contraction and calcium imaging. Furthermore, we confirmed NMJ function by MN-induced muscle contraction with four different iPSC-lines. Using MNs derived from ALS patient iPSCs we generated co-cultures that showed a decrease in muscle contraction over time. These data demonstrated the applicability of this system to study human diseases that affect the NMJ. In summary, we present a human *in vitro* model to study NMJ physiology and dysfunction in the context of NMJ-affecting diseases like ALS.

Materials and methods

Human myoblast and human fibroblast culture

Primary human skeletal muscle myoblasts were purchased from Lonza (#CC-2580) and cultured according to Afshar Bakooshli et al. (2019) with minor modifications. Briefly, myoblasts were cultured in growth medium containing F-10 media (Gibco, #11550043), 20% fetal bovine serum (Gibco), 5 ng/mL basic fibroblast growth factor (bFGF) (PeproTech, #100-18B) and 100 µg/mL penicillin-streptomycin (Gibco, #15-140-122). Cells were cultured until 80%–90% confluency and used between passages 4–10 for the experiments. Primary human fibroblasts (Thermo Fisher, #C0045C) were cultured in growth medium until confluency. Myoblast and fibroblast medium was changed every other day.

iPSC differentiation into neuronal progenitor cells (NPCs)

For the generation of 3D neuromuscular co-cultures, we used a previously reported human iPSC-line 34D6 (control iPSC-line #1) (Selvaraj et al., 2018), which was kindly provided by Prof. Chandran (University of Edinburgh). MNs were differentiated according to Reinhardt et al. (2013) or Kroehne et al. (2017) with some modifications. Briefly, iPSCs were expanded in mTeSR Plus (Stemcell Technologies, #05825) on Matrigel-coated (1:100) (Corning, 356234) dishes. 80%–90% confluent cells were split 1:5 using ReLeSR reagent (Stemcell Technologies, #05872). ROCK Inhibitor (10 µM) (StemMACS™ Y27632, Miltenyi Biotec, #130-106-538) was added for 24 h after splitting. For neuronal induction, mTeSR Plus medium was supplemented with 10 µM SB431542 (AdooQ BioScience, #A10826-50), 1 µM dorsomorphin homolog 1 (DMH1) (R&D Systems, #4126), 3 µM CHIR99021 (Cayman Chemical Company, #13122), and 0.5 µM Purmorphamine (PMA) (Cayman Chemical Company, #10009634). On day 2, the medium was changed to neuronal medium supplemented with the same small molecule supplements. Neuronal medium consisted of Neurobasal medium (Gibco, #21103049), Dulbecco's modified Eagle's medium F-12 (DMEM/F-12) (Gibco, #21331046), MACS NeuroBrew-21 (Miltenyi Biotech, #130-097-263), N-2 Supplement (Gibco, #17502048), 100 µg/mL Penicillin/Streptomycin/Glutamax (Gibco, #10378016). On day 4, the medium was changed to expansion medium consisting of neuronal medium supplemented with 3 µM CHIR99021, 0.5 µM PMA, and 150 µM Ascorbic acid (AA) (Sigma, #A92902). 80%–90% confluent cells were split and kept in suspension on uncoated dishes. Embryoid Bodies (EBs) formed

from day 6 on in suspension and were selected and dissociated with a 1 mL pipette. Subsequently, cells were seeded on Matrigel-coated dishes. The resulting NPCs were split about once every week with Accutase (Thermo Fisher, #07920) and expanded for at least 15 passages to achieve pure NPC cultures. The medium was changed every other day.

MN differentiation according to Reinhardt et al.

For ALS disease modeling, neuromuscular co-cultures were generated with the two previously reported human ALS iPSC-lines with a heterozygous R115G mutation and with a homozygous D90A mutation, respectively (Naujock et al., 2016; Gunther et al., 2022). ALS lines were kindly provided at NPC stage by Prof. Hermann (University Medical Center Rostock).
NPCs were cultured in expansion medium on Matrigel-coated dishes. For NPC differentiation into MNs, cells were cultured for 9 days in neuronal medium supplemented with 1 µM PMA. On day 2, 1 µM Retinoic acid (Stemcell Technologies, #72264) was added to the medium. The medium was changed every other day. For MN differentiation, the medium was switched after 9 days to neuronal medium supplemented with 10 ng/mL glia-derived neurotrophic factor (GDNF) (Alomone Labs, #G-240), 10 ng/mL brain-derived neurotrophic factor (BDNF) (PeproTech, #450-02), and 500 µM dibutyryl-cAMP (dbcAMP) (Stemcell Technologies, #73886).

MN differentiation according to Kroehne et al.

NPCs were cultured for 10 passages in expansion medium with 0.5 µM smoothened agonist (SAG) (EMD Millipore, #566660) instead of 0.5 µM PMA on Matrigel-coated dishes. For NPC differentiation, cells were cultured for 6 days in neuronal medium supplemented with 0.5 µM SAG, 1 µM RA, 1 ng/mL GDNF, and 2 ng/mL BDNF. For MN differentiation, the medium was switched after 6 days to neuronal medium supplemented with 200 µM AA, 2 ng/mL GDNF and BDNF, 1 ng/mL transforming growth factor beta (TGFß3) (Sigma, #SRP3171), 200 µM dbcAMP, and 10 µM tert-Butyl(2S)-2-[[(2S)-2-[[2-(3,5-difluorophenyl)acetyl]amino]propanoyl]-amino]-2 phenylacetate (DAPT) (Cayman Chemical Company, #13197) for at least 14 days.
For a subset of co-culture experiments, we used MNs derived from the iPSC-line IMR90-4 (control iPSC-line #2), originally purchased from WiCell (Yu et al., 2007). Differentiation was performed as previously described (Schenke et al., 2020), based on protocols established by Kroehne et al. (2017). MNs were differentiated until day 6, cryopreserved, thawed and cultured as described above (on Matrigel dishes in neuronal medium supplemented with 200 µM AA, 2 ng/mL GDNF and BDNF, 1 ng/mL TGFß3, 200 µM dbcAMP and 10 µM DAPT) for at least 14 days.

Self-manufactured 3D co-culture dishes

Polydimethylsiloxane (PDMS) (Sigma, #761036-5 EA) dishes were fabricated as described by Afshar Bakooshli et al. (2019) with some modifications. 3.5 cm Petri dishes (Sarstedt) were coated with 1.25 mL liquid PDMS and kept at 65°C for at least 3 h. Next, 1.75 mL PDMS were added, and two dumbbell shaped acrylic templates (middle channel dimensions = 14 mm by 2.75 mm; side chamber dimensions = 5.7 mm by 2.5 mm) (Figure 1A) were pressed into the PDMS next to each other. Air bubbles were removed within a vacuum chamber if necessary. After curing, acryl pieces were removed and 5.7 mm by 2.5 mm Velcro pieces were anchored on each channel side with liquid PDMS and cured again. Dishes were sterilized with 70% ethanol for 30 min and subsequently with 15 min UV light. Afterwards, the dishes were wrapped in parafilm and stored at room temperature (RT). PDMS dumbbell shape molds were incubated with 5% Pluronic acid (Thermo Fisher, #P6866) for at least 4 h at 4°C before applying the hydrogel.

Generation of 3D skeletal muscle tissue

3D muscle tissues were generated as described by Afshar Bakooshli et al. (2019) with some modifications with two independent biopsies of skeletal myoblasts from Lonza (#CC-2580). For the hydrogel, 1500000 skeletal myoblasts, 75000 fibroblasts, 20% Geltrex (Gibco, #A1413302), 4 mg/mL Fibrinogen, 0.8 U Thrombin and DMEM/F- 12 were mixed in a total volume of 200 µL, and filled into the PDMS channels completely covering the Velcro hooks. The hydrogel was incubated for 5 min at 37°C in the incubator prior to adding medium. 3D differentiation medium consisted of neuronal medium supplemented with 2% horse serum (Sigma, #H1138), 10 ng/mL Insulin (Merck, # I9278), 2 mg/mL 6-aminocaproic acid (ACA) (Sigma, #A2504), 2.5 µg/ mL Amphotericin B (Sigma, #15290-026) and 50 ng/mL Agrin (R&D Systems, # 550-AG-100). The medium was changed every other day.

3D neuromuscular co-cultures

For the generation of 3D neuromuscular co-cultures, the hydrogel was prepared as described above and 500000 MNs were added to the hydrogel.
For neuromuscular co-cultures with MNs differentiated according to Reinhardt et al., MNs were used from day 9 of differentiation. 3D differentiation medium was supplemented with 10 ng/mL GDNF and BDNF and 500 µM dbcAMP. After 2 days, GDNF and BDNF concentrations were increased to 20 ng/mL. For neuromuscular co-cultures with MNs differentiated according to Kroehne et al. (control iPSC-line #1 derived MNs and control iPSC-line #2 derived MNs), MNs from differentiation day 6 were used and cultured in 3D differentiation medium supplemented with 200 µM AA, 2 ng/mL GDNF, 2 ng/mL CNTF (PeproTech, #450-13), and 2 ng/mL BDNF, 1 ng/mL TGFß3, 200 µM dbcAMP and 10 µM DAPT. After 2 days GDNF, CNTF, and BDNF concentrations were increased to 4 ng/mL.
The medium was changed every other day and co-cultures were cultured until the indicated time points for experiments.

RNA isolation, cDNA synthesis, and quantitative real-time PCR (RT qPCR)

Total RNA was isolated with the NucleoSpin® RNA kit (Macherey Nagel, #REF 740955.50). RNA was treated with DNase I (Thermo Fisher, #EN0521) to ensure the removal of genomic DNA. 100 ng total RNA was used for cDNA synthesis using the First Strand cDNA Synthesis Kit (Thermo Fisher, #K1612). For cDNA synthesis, random oligos were used.

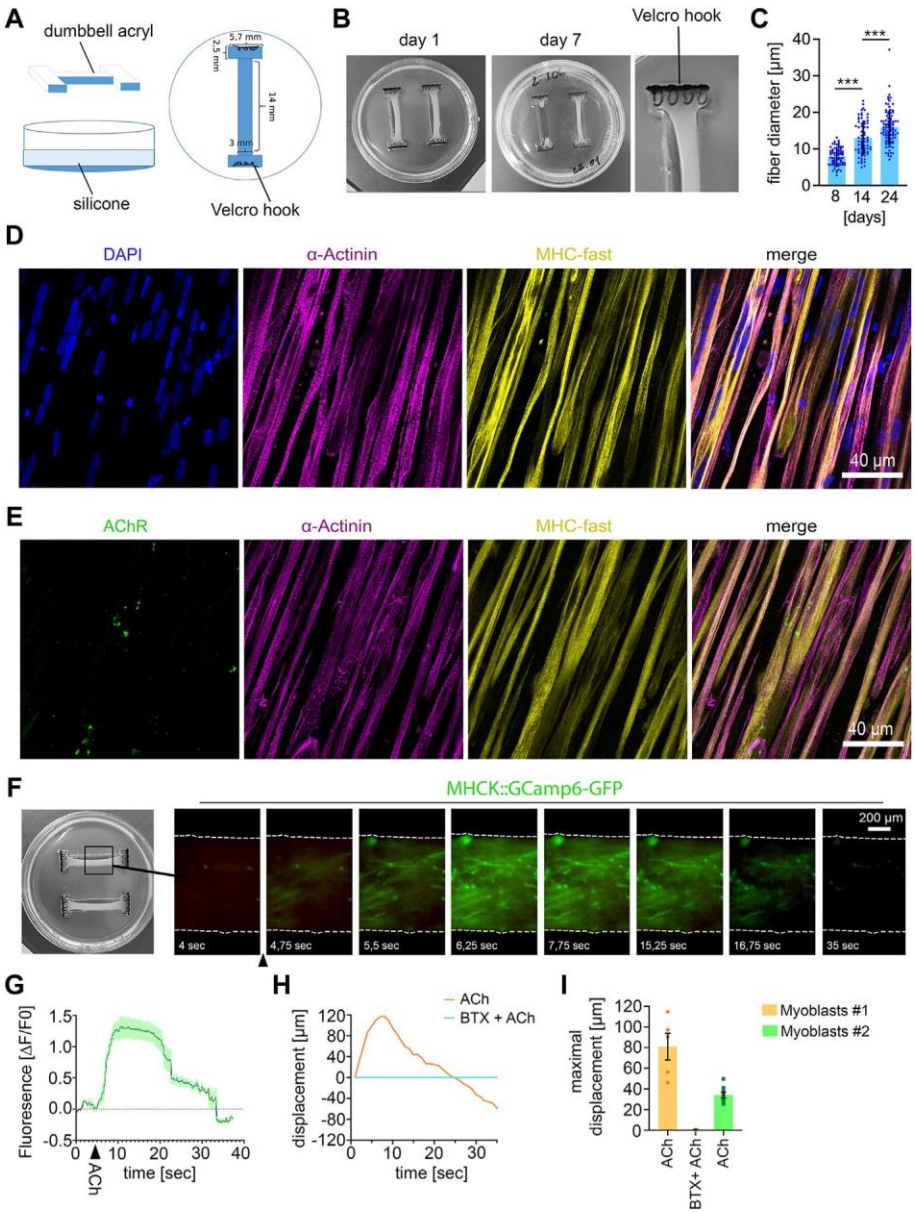

FIGURE 1
Establishing 3D human muscle tissue (A) Scheme of dumbbell-shaped template for microfabrication of the 3D culture dish. (B) Macroscopic images of the human muscle tissue with 1500000 myoblasts at the indicated culture time. The use of too high cell numbers (2000000 cells) lead to tearing of muscle fiber tissue (muscle tissue on the right side in the middle image). (C) Quantification of muscle fiber diameter. 8 days, *n* = 72; 14 days, *n* = 70; 24 days, *n* = 85; Mean ± SEM; each data point represents the diameter of an individual muscle fiber. One-way ANOVA, Tukey's multiple comparisons test. (D) Immunocytochemical stainings of 21 days-old muscle fiber tissue against α-Actinin, Myosin Heavy Chain (MHC)- fast and DAPI. Scale bar: 40 µm. (E) Immunocytochemical stainings of 21 days-old muscle fiber tissue against Acetylcholine Receptors (AChR), α-Actinin and MHC fast. Scale bar: 40 µm. (F) Time lapse images of a representative calcium transient. Arrowhead indicates timepoint of ACh stimulation. (G) Representative calcium transient upon ACh treatment, each data point represents the mean of six ROIs. Mean ± SEM. (H) Quantification of the muscle fiber contraction. A representative curve for the muscle tissue displacement upon ACh treatment and upon pretreatment with BTX, followed by ACh stimulation is shown. (I) Quantification of the maximal muscle fiber displacement. Each data point represents the maximal displacement of an individual muscle fiber tissue. Myoblasts #1: ACh, *n* = 5; BTX + ACh, *n* = 2. Myoblasts #2: ACh, *n* = 8.

To ensure genomic DNA removal, for each sample set a control reaction was prepared without reverse transcriptase. cDNA was diluted 1:5 with water, and 1 µL was used for each qPCR reaction using the Thermo Scientific™ Luminaris HiGreen qPCR Master Mix (Thermo Fisher, # K0993) on a LightCycler 1.5 thermal cycler (Roche). The following primers were used: *HB9*: 5′-GCACCAGTTCAAGCTCAACA-3´ (Forward), 5′-TTCTGTTTCTCCGCTTCCTG-3´ (Reverse), *CHAT*: 5′-GAAGACTGGTGCCCACCTAC-3´ (Forward), 5′-GCATCCTTC AGGAGCAGAA-3´ (Reverse), *SOX2* 5′-AACCCCAAGATGCAC AACTC-3´ (Forward), 5′-CGGGGCCGGTATTTATAATC-3´ (Reverse), *GAPDH* 5′-CTTCGCTCTCTGCTCCTCCTGTTCG-3´ (Forward), 5′-ACCAGGCGCCCAATACGACCAAAT-3´ (Reverse). For detection of *LHX3*, *HOXA2,* and *HOXA4* previously published primers were used (Reinhardt et al., 2013; Maury et al., 2015).

Immunocytochemical staining

Neuromuscular tissues and muscle tissues were transferred from 3D dishes to Eppendorf tubes, washed with phosphate-buffered saline (PBS), and fixed in 4% paraformaldehyde for 15 min at RT. Tissues were washed three times with PBS and incubated for 30 min in blocking solution containing 15% donkey serum and 0.3% Triton X-100 in TBS-Tween (TBST). After three washes with TBST, tissues were incubated with α-Bungarotoxin-Alexa-488 (α-BTX) (1:500) (Invitrogen, #B1601) for 30 min at RT and washed with TBST. Tissues were incubated overnight with primary antibodies diluted in 1:10 diluted blocking solution at 4°C. The next day, tissues were washed three times with TBST and incubated with appropriate fluorophore-conjugated secondary antibodies diluted 1:800 in 1:10 diluted blocking solution for 1 h at RT. Subsequently, tissues were washed three times with PBS and nuclei were counterstained with DAPI for 10 min and washed quickly with PBS. Squeeze preparations of the neuromuscular tissues and muscle tissue were mounted on glass slides with Aqua-Poly/Mount (Polysciences, #18606-20).

The same protocol was applied to stain iPSC-derived MNs differentiated according to Reinhardt et al. cultured for 14 days on Matrigel-coated coverslips.

16-bit images with 800 × 800-pixel or 1,024 × 1024-pixel resolution were acquired using an Olympus Fluoview 1,000 confocal microscope equipped with 20×, 40×, and 60× objectives. Images were processed with ImageJ.

The following primary antibodies were used: Anti-α-Actinin 2 (1:1,000, Sigma-Aldrich, ZRB1169, clone 1E11), anti-α-Actinin (1:1,000, Sigma-Aldrich, A7811, clone EA-53), anti-Myosin heavy chain human fast fibers (1:100, Developmental Studies Hybridoma Bank, A4.74, clone), anti-Tuj1 (1:1,000, Neuromics, MO15013), anti-Neurofilament heavy polypeptide antibody (1:1,000, Abcam, ab4680), anti-Synaptophysin-1 (1:1,000, Synaptic Systems, 101,004), anti-Islet-1 (1:500, Synaptic Systems, 406,003). Alexa-647-, Alexa-488- and Alexa-546-conjugated secondary antibodies were purchased from Jackson Immuno-Research Laboratories.

Axon outgrowth measurements

To evaluate the axon stability in the neuromuscular co-cultures, the axon outgrowth in co-cultures was analyzed on day 9, day 21, and day 42. Co-cultures were fixed at the indicated time points as described above and stained with an anti-Neurofilament-H antibody (NF-H) (1:1,000, Abcam, ab4680). 16-bit images with 1,024 × 1024-pixel resolution were acquired using an Olympus Fluoview 1,000 confocal microscope with a 10× objective. At least four areas with an average size of 1.4 mm^2 per sample were analyzed with ImageJ. To analyze the axon outgrowth, we determined the area covered with axons as visualized by the NF-H staining.

Myofiber size analysis

For measuring the muscle fiber diameter, images of α-Actinin stained 3D muscle tissues were acquired with a 20x objective using an Olympus Fluoview 1,000 confocal microscope. The diameter of individual myofibers was manually measured using ImageJ.

Muscle displacement measurements

Muscle contraction of 3D muscle tissue was imaged using an Olympus CKX41 microscope equipped with a LED illumination system (pE excitation system CoolLED) and an Olympus EP50 camera. 3 min videos were recorded with 10× magnification at 30 frames per second at 37°C. For stimulating muscle contraction, 100 µM ACh or 500 µM glutamate was directly applied to the culture dish as batch application. For control experiments, 10 min prior stimulation 1 µM BTX (Invitrogen, #B1601) or 60 nM tetrodotoxin (TTX) (Sigma, #T8024) were added, or 48 h prior stimulation 2 pM botulinum toxin (BoTN) (Miprolab, #3101-0010) was added. The muscle displacement was analyzed using ImageJ. At least two separate positions with highest contraction per muscle were individually measured. Fiber contraction at each position was traced per second and recorded as displacement per second. Longitudinal displacement was measured from the initial starting frame and displayed as movement in µm. Co-cultures derived from ALS iPSCs were evaluated in a blinded manner.

Calcium imaging

For calcium imaging experiments a subset of myoblasts was transduced twice during expansion with an MHCK:GCamp6-GFP expressing lentivirus (pRRL-MHCK7-GCaMP6 was purchased from Addgene #65042) (Madden et al., 2015). 3 min videos were recorded using an Olympus CKX41 microscope equipped with a LED illumination system (pE excitation system CoolLED) and an Olympus EP50 camera with 10× magnification at eight frames per second at 37°C. Fluorescence changes over time were analyzed with ImageJ.

Lentivirus production

Lentivirus was produced as previously described (Luningschror et al., 2017). Briefly, HEK 293T cells were transfected with the pRRL-MHCK7-GCaMP6 plasmid and the packaging plasmids using calcium phosphate. The medium was replaced 24 h after transfection and collected 24 h later. Subsequently, the virus was concentrated by ultracentrifugation.

Statistics

Statistical analysis was performed in GraphPad Prism eight and statistical significance was considered at $p < 0.05$. Significance is designated as *, $p < 0.05$; **, $p < 0.01$, and ***, $p < 0.001$. The statistical test used to determine significant differences is described in the corresponding figure legend.

Results

Establishing 3D human muscle tissue

For microfabrication of the 3D muscle tissue culture dishes, we produced dumbbell-shaped acryl pieces as a first step (Figures 1A, B).

Two of these acryl pieces were placed in a 3.5 cm cell culture dish and PDMS was poured into the dish to fabricate the dumbbell-shaped 3D muscle culture dishes. As anchoring points for the muscle tissue formation, Velcro pieces with nylon hooks were fixed on each end of the dumbbell-shaped channel with PMDS (Figure 1B).

For muscle tissue formation, myoblasts and fibroblasts were mixed with a fibrinogen/Geltrex hydrogel and seeded into the 3D dish. For optimization of muscle tissue formation, we tested different hydrogel to myoblast ratios (Supplementary Table S1). We observed that no muscle tissue was formed when cell numbers were too low in the hydrogel, whereas too many cells within the hydrogel lead to tearing of the muscle tissue (Figure 1B). 14 days after seeding the hydrogel-myoblast mixture, we observed the formation of 3D muscle tissue macroscopically. Next, we analyzed the fiber diameter and detected an increase over time suggesting the maturation of the muscle tissue (Figure 1C). Overall, myofibers aligned along the axes of the dish generating continuous muscle tissue. By immunostaining we could detect the muscle-specific markers sarcomeric α-Actinin, revealing the characteristic striated pattern, and expression of the fast myosin heavy chain (MHC). Furthermore, we detected the morphological formation of multinuclear myofibrils and AChRs clustering as visualized by α- Bungarotoxin (BTX) staining (Figures 1D, E).

To demonstrate the 3D muscle function, we analyzed the cytosolic calcium influx upon ACh stimulation (Figures 1F, G). Myoblasts were transduced with a lentivirus encoding the calcium sensor GCamp6-GFP under the muscle-specific MHCK7 promoter and subsequently used for muscle tissue formation. Upon stimulation with ACh, we detected a rapid fluorescence increase, which demonstrates a calcium influx into the cytosol (Figures 1F, G). Next, we analyzed muscle contraction by quantifying the tissue movement upon stimulation with ACh using live-cell imaging. ACh stimulation induced a fast contraction of the muscle tissue, which could be completely inhibited by blocking AChRs with BTX (Supplementary Video S1) (Figures 1H, I).

Given the limited passage number of primary myoblasts, we wondered if 3D muscle tissue can be reproducibly generated with myoblasts derived from a different muscle biopsy. Macroscopically, we did not observe any difference between both samples. Upon stimulation with ACh, we also observed a robust contraction of muscle tissue derived from the second batch of primary myoblasts (Figure 1I). However, quantification of the tissue movement revealed that the maximal muscle displacement caused by ACh was lower compared to the first batch of myoblasts.

NMJ functionality in 3D neuromuscular co-cultures

Next, we generated 3D neuromuscular co-cultures by adding iPSC-derived MNs to the hydrogel-myoblast mixture. For MN differentiation we utilized the previously established protocol by Reinhardt et al. (2013). To confirm a proper MN induction and differentiation, we performed RT-qPCR and immunocytochemical stainings (Figure 2). For RT-qPCR, samples were collected at different time points during differentiation. We analyzed the expression of *MNX1*, *ChAT*, *POU5F1*, *SOX2*, *HOXA2,* and *HOXA4* at the iPSC- and neural progenitor stage, and in MNs, 18 days after maturation (Figure 2A).

According to the ΔΔCT method we detected the following average fold changes in NPCs and MNs relative to the iPSC stage. The expression of the pluripotency marker *POU5F1* was reduced by 147 -fold in NPCs and 154-fold in MNs. The *SOX2* expression increased by 2.7-fold in NPCs but showed a downregulation by 10.7-fold from NPCs to MNs. The expression of the MN-specific transcription factor *MNX-1* was increased by 2.5-fold in NPCs, and by 120.7-fold in MNs. The expression of *CHAT* was not detectable in iPSCs. When normalized to NPCs, the *CHAT* expression increased by 226-fold in MNs. The expression of *HOX2A* increased by 339-fold from iPSCs to NPCs but deceased by 2.2-fold from NPCs to MNs. In contrast, during differentiation from iPSC to NPCs we detected a 604- fold increase in the expression of H*OX4A*, which further increased to 8800-fold from iPSCs to MNs. In summary, the data confirm neural induction and differentiation into spinal MNs. To examine the efficiency of MN differentiation, we stained MN cultures 14 days after maturation for Tuj1 and Islet-1. On average, roughly 75% of the cells stained positive for the MN marker Islet-1 (Figures 2B, C). MNs showed the expected polarity with one long axon and 3- 4 dendrites as shown by Islet-1 and NF-H staining (Figure 2D).

After 14 days of co-culturing, we observed axons growing in between muscle fibers as shown by Tuj1 and α-Actinin staining (Figure 3A). Furthermore, we detected MN terminals close to AChR$^+$ clusters, indicating the formation of NMJs (Figure 3B). NMJ formation was further confirmed by Synaptophysin-1 and AChR staining as pre- and post-synapse marker (Figure 3C). Pre- synaptic structures co-localized at MN axons (branches) shown by Synaptophysin-1 and NF-H staining (Figure 3C).

To test the functionality of the NMJs, we stimulated co-cultures with glutamate to induce MN activity. Upon firing ACh is released from the MN terminals which triggers depolarization on the postsynaptic side in the muscle cells. Using GCamp6-GFP- expressing muscle tissue we observed an increase of free calcium in the cytosol of muscle cells upon glutamate stimulation (Figure 3D), suggesting functional signal transduction from MN to muscle. Next, we analyzed the muscle contraction upon glutamate stimulation in co- cultures generated with MNs derived from two independent iPSC- lines (Figure 3F). Glutamate treatment triggered a muscle tissue contraction (Supplementary Video S2) (Figures 3E, F), that could be completely abolished by blocking the activity of voltage-gated sodium channels using TTX (Figures 3E, F). To confirm that the muscle contraction was induced by presynaptic MN activity, and not by activation of postsynaptic glutamate receptors (Mays et al., 2009), we specifically inhibited the presynaptic activity with BoTN. Indeed, pretreatment of co-cultures with BoTN blocked the glutamate- induced muscle contraction (Figure 3F). Moreover, we did not detect any significant glutamate-induced contraction in muscle tissues grown without MNs (Figure 3F). Taken together, these data show that functional NMJs are generated between iPSC-derived MNs and muscle tissue.

Next, we wondered about the stability of this system and maintained MNs and muscle tissue for up to 6 weeks in culture (Figures 3G–I). We analyzed the axon growth after 9, 21, and 42 days by NF-H staining (Figures 3G, H). We found that the axon growth peaked at day 21. From day 21–42 axon growth stagnated, but the axon integrity remained stable, suggesting that they reached their target during this period (Figures 3G, H). To analyze whether the functionality of connections between MNs and muscle tissue remained stable, we stimulated the co-cultures with glutamate at

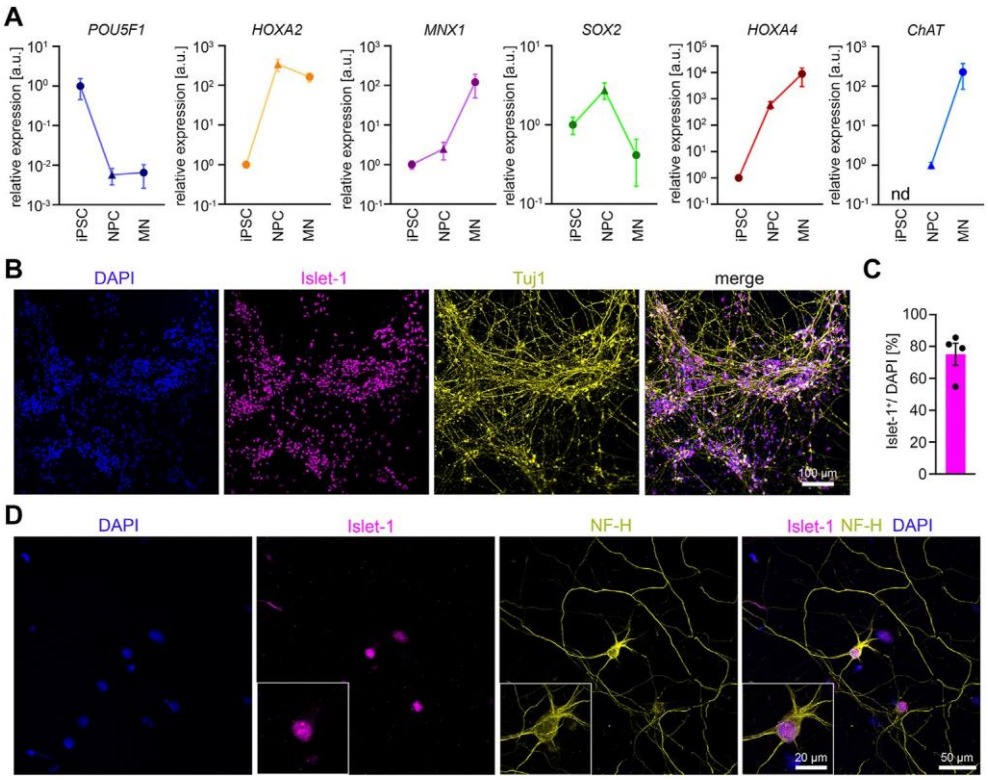

FIGURE 2
Differentiation of iPSCs into MNs (A) RT-qPCR analysis of the expression pattern of several marker genes during MN differentiation $n = 5$. Mean ± SEM. n.d., not detectable. (B) Representative low magnification image of iPSC-derived MNs stained for Islet-1 and Tuj1 after 14 days of maturation. (C) Quantification of Islet-1 positive cells. $n = 5$. Mean ± SEM. (D) Representative image of an individual iPSC-derived MN stained for Neurofilament Heavy Chain (NF-H) and Islet-1 after 14 days of maturation.

different time points for up to 6 weeks (Figure 3I). The glutamate-induced muscle contraction peaked at 21 days and started to decline up to 42 days. However, these differences were minor and statistically not significant, indicating that the connections between muscle and MNs remained stable during the investigated period.

ALS disease modeling

To demonstrate that the co-culture system is applicable as a disease model, we differentiated two iPSC lines derived from ALS patients with *SOD1* mutations to MNs, which were subsequently co- cultured with muscle tissue (Figure 4A). One of the patients carried a heterozygous R115G mutation. The other patient carried a homozygous D90A mutation. Both iPSC lines have previously been characterized (Naujock et al., 2016; Gunther et al., 2022). Macroscopically, co-cultures with ALS MNs were indistinguishable from healthy controls. After 14 days in culture, co-cultures with MNs derived from ALS iPSCs showed a similar glutamate-induced muscle contraction to control cultures, indicating a functional integration of the ALS MNs (Figures 4B, C). Interestingly, we observed a decrease in muscle contraction in co-cultures generated with ALS MNs after 21 days. This effect was observed with both *SOD1* mutations (Figure 4B) and reached statistical significance when the results from both controls and the ALS cultures were pooled (Figure 4C). After 21 days, the co-cultures were fixed and stained for NF-H to analyze the axon stability (Figures 4D–F). In correlation with the decrease in muscle contraction, we detected a reduced axonal coverage of the muscle tissues in ALS co-cultures (Figures 4E, F). Taken together, these data suggest that MNs carrying SOD1 mutation successfully integrate into the system, but start to display a pathological phenotype at a later time point.

Discussion

Here we adapted, validated, and applied a previously described method to co-culture 3D human skeletal muscle tissues together with human iPSC-derived MNs. We used this system to generate co-cultures with MNs harboring ALS-linked *SOD1* mutations and found that these MNs were able to functionally integrate into the culture but started to show signs of a pathological phenotype at a later stage. Our results show the successful generation of functional human NMJs *in vitro,* which can be used as a disease model to study the pathophysiology of MNDs like ALS.

In this study, we generated functional muscle tissue with primary myoblasts derived from two different biopsies. Whereas both batches of primary myoblasts robustly formed well-structured contractile muscle tissue, we observed a batch-to-batch variability in the strength of muscle contraction. These data show that biopsy- derived myoblasts are a reliable source for 3D muscle tissue generation that is capable to form functional connections with

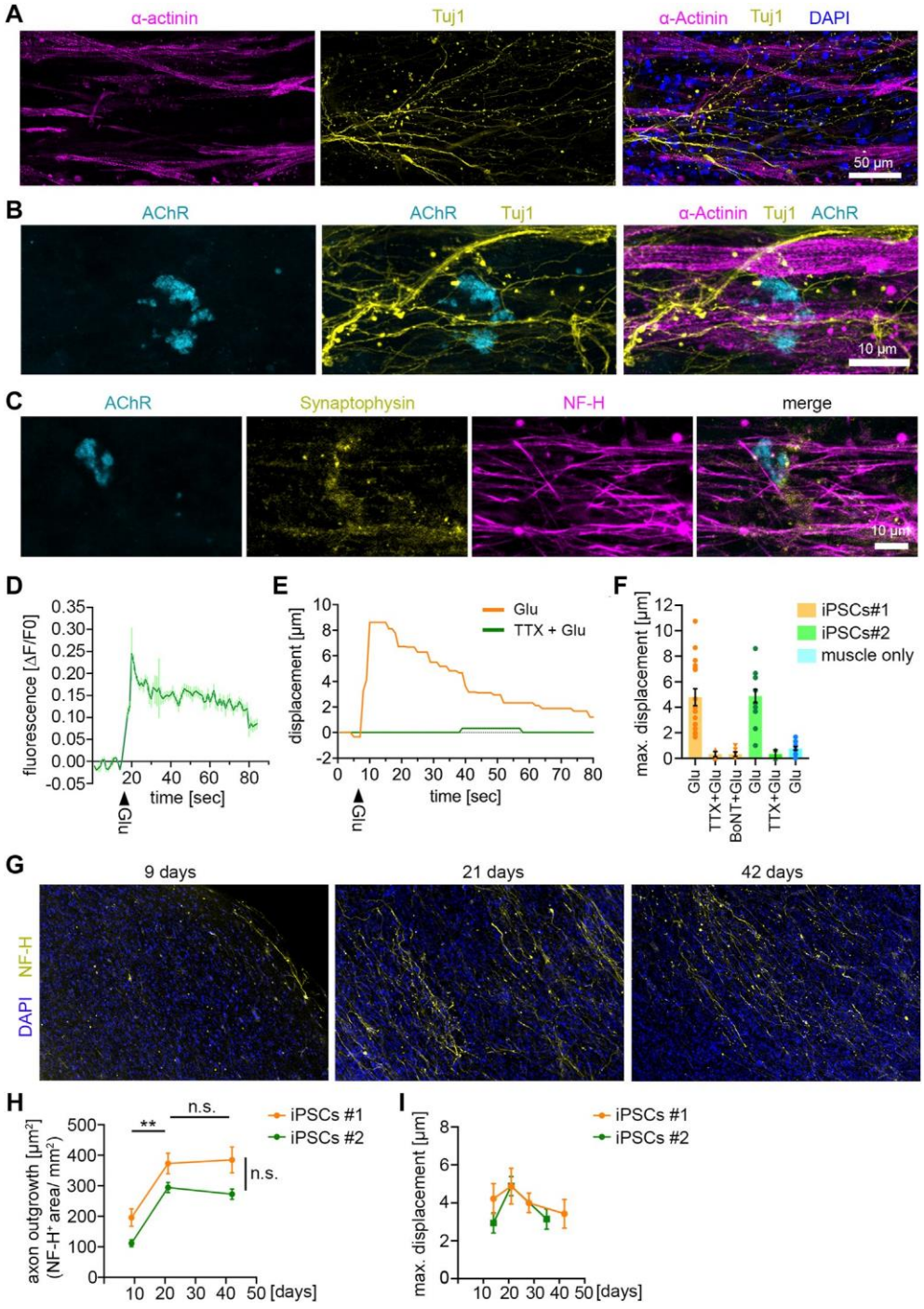

FIGURE 3
NMJ functionality in 3D neuromuscular co-cultures (A) Immunocytochemical stainings of a 21 days-old neuromuscular co-culture against Tuj1, α-Actinin and DAPI. Co-cultures were generated with MNs derived from control iPSC-line #1. MNs were differentiated according to Reinhardt et al. (B) Immunocytochemical stainings of a 21 days-old neuromuscular co-culture against AChR, Tuj1 and α-Actinin. (C) Immunocytochemical stainings of a 21 days-old neuromuscular co-culture against AChR, Synaptophysin-1 and NF-H. (D) Representative calcium transient upon glutamate treatment. Each data point represents the mean of seven ROIs. Mean ± SEM. Glu, glutamate. (E) Quantification of the muscle fiber contraction. A representative curve for the muscle tissue displacement upon glutamate treatment is shown. A second curve shows the muscle displacement after pretreatment with TTX, followed by glutamate stimulation. TTX, tetrodotoxin. Glu, glutamate. (F) Quantification of the maximal muscle fiber displacement after 21 days. Two independent iPSC lines were used to generate MNs, which were subsequently used for the co-cultures. Each data point represents the maximal displacement of an individual muscle fiber tissue. Mean ± SEM. iPSCs#1: Glu, $n = 17$; TTX + Glu, $n = 4$; BoNT + Glu, $n = 6$. iPSCs#2: Glu, $n = 15$; TTX + Glu, $n = 2$. Muscle only, $n = 13$. (G) Representative low magnification images of co-cultures stained for NF-H and DAPI at the time points indicated. (H) Quantification of the axon outgrowth. Two independent iPSC lines were used to generate MNs, which were subsequently used for the co-cultures. iPSCs#1: Day 9, $n = 7$; Day 21, $n = 4$; Day 42, $n = 11$. iPSCs#2: Day 9, $n = 7$; Day 21, $n = 8$; Day 42, $n = 10$. (I) Quantification of the maximal muscle fiber displacement. Co-cultures were stimulated with glutamate and the tissue movement was analyzed at the time points indicated. iPSCs#1: Day 14, $n = 13$; Day 21, $n = 10$; Day 28, $n = 16$; Day 42, $n = 7$. iPSCs#2: Day 14, $n = 5$; Day 21, $n = 15$; Day 35, $n = 6$.

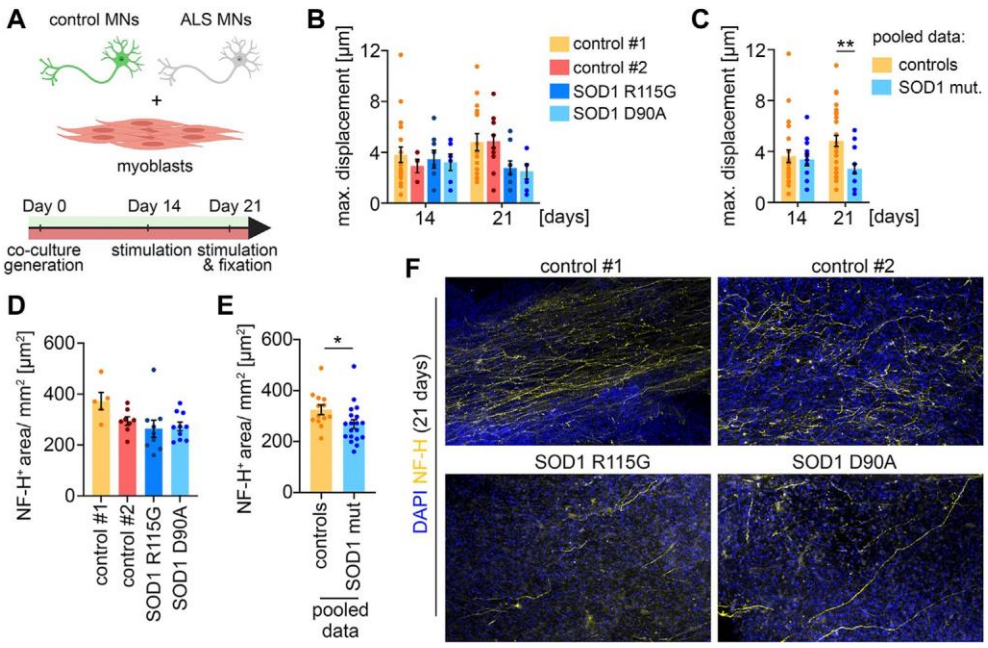

FIGURE 4
ALS disease modeling (A) Scheme of the experimental setup. (B) Quantification of the maximal muscle fiber displacement. Co-cultures were stimulated with glutamate after 14 and 21 days in culture and the tissue movement was analyzed. Control#1: Day 14, $n = 20$; Day 21, $n = 17$. Control#2: Day 14, $n = 5$; Day 21, $n = 15$. *SOD1*$^{+/R115G}$: Day 14, $n = 8$; Day 21, $n = 9$. *SOD1* $^{D90A/D90A}$: Day 14, $n = 6$; Day 21, $n = 8$. (C) Pooled data of the quantifications shown in (B). Controls (control#1 & control#2): Day 14, $n = 25$; Day 21, $n = 32$. SOD1 mut. (*SOD1*$^{+/R115G}$ & *SOD1* $^{D90A/D90A}$): Day 14, $n = 22$; Day 21, $n = 17$. Two-tailed *t*-test. (D) Quantification of the axon outgrowth after 21 days. Control#1: $n = 5$. Control#2: $n = 8$. *SOD1*$^{+/R115G}$: $n = 10$. *SOD1* $^{D90A/D90A}$: $n = 10$. (E) Pooled data of the quantifications shown in (D). Controls (control#1 & control#2): $n = 13$. SOD1 mut. (*SOD1*$^{+/R115G}$ & *SOD1* $^{D90A/D90A}$): $n = 20$. Two-tailed *t*-test. (F) Representative low magnification images of co-cultures stained for NF-H and DAPI after 21 days.

MNs in neuromuscular co-cultures. However, the limited passage number and batch—to-batch variability represent disadvantages of primary myoblasts as the starting cell population. Nagashima et al. (2020) recently employed the human immortalized human myogenic cell line Hu5/KD3 to generate contractile muscle tissues. Testing Hu5/KD3 cells for their capability to form muscle tissue that functionally connects with MNs will be an interesting future direction to overcome the limitation of primary myoblasts.

When co-cultured with MNs, we observed a robust contraction of the muscle tissue upon glutamate stimulation. This contraction could be completely abolished by TTX and BoNT. Moreover, glutamate did not induce any contraction in muscle tissue cultured without MNs. Thus, glutamate induces muscle contraction by triggering MN activity, and not by activation of postsynaptic glutamate receptors on the surface of muscle cells (Mays et al., 2009). In summary, these data demonstrate the functional connection between MNs and muscle tissue.

However, on the morphological level, bioengineered human NMJs differ from their *in vivo* counterparts. Two recent comparative studies characterized human NMJs *in vivo* (Jones et al., 2017; Boehm et al., 2020). Compared to other vertebrate species human NMJs are small, with thinner pre-terminal axons, more rudimentary nerve terminals, and distinctive endplates formed like coin-shaped patches (referred to as "nummular") (Jones et al., 2017; Boehm et al., 2020). However, they show the highest extent of postsynaptic folding among vertebrate species (Slater, 2008). In contrast, *in vitro* only contacts between MN axons and muscle fibers without any typical "NMJ-like" morphology have been described so far (Steinbeck et al., 2016; Osaki et al., 2018; Afshar Bakooshli et al., 2019; Bellmann et al., 2019; Stoklund Dittlau et al., 2021). We also observed this phenomenon in our study. To the best of our knowledge, NMJs with typical morphological features such as the postsynaptic folding have not been reported yet.

Several aspects could be considered to improve NMJ maturation. During embryonic development initial connections between MNs and myotubes are unspecialized without showing typical NMJ morphology, yet. However, these first contacts are capable of rudimentary synaptic transmission (Sanes and Lichtman, 1999). During maturation, the NMJ morphology undergoes dramatic changes. If *in vitro* generated NMJs represent an early developmental stage, a prolonged culture period could play a crucial role to ensure NMJ maturation. Our data indicate that neuromuscular co-cultures are viable and functional for at least up to 6 weeks. Especially when considering the different time periods for embryonic development of most model organisms compared to humans, it will be an exciting future direction to test whether longer culture periods contribute to NMJ maturation.

In addition to the culture period, repeated stimulation is most likely required to support NMJ maturation. This could be achieved by enriching the culture medium with e.g., NMDA and/or AMPA receptor agonists. A different strategy could be a repeated optogenetic or electrical stimulation of MNs and/or muscle tissue.

Another important aspect to improve NMJ maturation and maintenance are defined medium components to co-culture different cell types in 3D. Besides Agrin, several other molecules like fibroblast growth factor, HB-GAM/pleitrophin, laminin beta 2,

and midkine have been reported to promote NMJ formation (Sanes and Lichtman, 1999).

During embryonic and postnatal NMJ maturation *in vivo*, terminal Schwann cells play a fundamental role in addition to MNs and muscle cells. In a recent publication with self-organizing human neuromuscular organoids (Faustino Martins et al., 2020) the differentiation of terminal Schwann cells at NMJs was reported, pointing to the importance of this cell type. Schwann cells cap the nerve terminal, supporting its morphology and maintenance (Alvarez-Suarez et al., 2020; Faustino Martins et al., 2020). On the muscle side, Schwann cells enhance myotube growth and size and number of AChRs (Horner et al., 2021). Therefore, the inclusion of Schwann cells in the co-culture would be an interesting approach for the improvement of this system.

To validate the developmental stage of bioengineered NMJs, electrophysiological measurements are needed to determine the physiological properties of the MNs. However, the size and 3D structure of the co-culture make it difficult to identify innervated muscle fibers and the corresponding MNs that make synaptic contact to them. MNs and muscle fibers are randomly mixed, and fluorescent-labeled MNs can only get precisely identified at the confocal microscope. Recently, an elegant Rabies virus-based retrograde tracing approach has been applied to a neuromuscular co-culture system (Bellmann et al., 2019). Utilizing such an approach could overcome the challenge of identifying innervated muscle fibers.

To test the applicability of this system, we generated and analyzed co-cultures with MNs derived from ALS patient iPSCs. We show that these MNs functionally integrate into the system but start to show signs of a pathological phenotype at 21 days of culture. These data demonstrate that the neuromuscular co- culture system presented here is suitable for human *in vitro* disease modeling of the NMJ. Our data are in agreement with a recent study with utilized sensorimotor organoids to model ALS *in vitro*. Among different ALS mutations, organoids carrying a $SOD1^{G85R}$ mutation were analyzed and an impairment at the NMJ level was identified, as shown by contraction and immunocytochemical measurements (Pereira et al., 2021). Future studies employing human *in vitro* models of NMJs may help to develop and validate new mechanistic hypotheses for early pathogenesis in neuromuscular diseases. For ALS in particular, NMJs appear as an early and vulnerable target and provide the most important pathological and functional disease readouts (Murray et al., 2010).

Taken together, we report the generation of a functional 3D neuromuscular co-culture system using myoblast-derived muscle tissue and iPSC-derived MNs. This co-culture represents a valuable tool for modeling NMJ-affecting human diseases, but also for studying human NMJ development.

Data availability statement

The raw data supporting the conclusion of this article will be made available by the authors, without undue reservation.

Author contributions

PL and BM conceived the study. BM performed all the experiments. BTS and SC provided human iPSC-line 34D6 (control iPSC-line #1). BM and SM performed differentiation of human iPSC- line 34D6. MSch performed MN differentiation from iPSC-line IMR90-4 (control iPSC-line #2). BM and AV analyzed data. AH, PR and JS provided the human ALS iPSC lines and critically information on MN differentiation. BS and MS provided critical comments on the manuscript. PL and BM assembled data and wrote the manuscript. All authors approved the final draft of the manuscript.

Funding

PL was supported by the BMBF grant VORAN, 161L0150 and VORAN-2, 16LW066. This publication was supported by the Open Access Publication Fund of the University of Wuerzburg. AH is supported by Hermann and Lilly Schilling Stiftung für Medizinische Forschung im Stifterverband.

Acknowledgments

We thank Hildegard Troll for lentivirus production. We are grateful to Janina Dix and Nicole Rachor for excellent technical assistance. We thank Penney Gilbert for sharing critical information.

Conflict of interest

The authors declare that the research was conducted in the absence of any commercial or financial relationships that could be construed as a potential conflict of interest.

Publisher's note

Supplementary material

The Supplementary Material for this article can be found online at: https://www.frontiersin.org/articles/10.3389/fcell.2023.996952/full#supplementary-material

SUPPLEMENTARY VIDEO S1
3D muscle conraction upon 100 µM ACh stimulation.

SUPPLEMENTARY VIDEO S2
3D co-culture contraction upon 500 µM glutamate stimulation.

References

Afshar Bakooshli, M., Lippmann, E. S., Mulcahy, B., Iyer, N., Nguyen, C. T., Tung, K., et al. (2019). A 3D culture model of innervated human skeletal muscle enables studies of the adult neuromuscular junction. *Elife* 8. e44530. doi:10.7554/eLife.44530

Alvarez-Suarez, P., Gawor, M., and Proszynski, T. J. (2020). Perisynaptic schwann cells - the multitasking cells at the developing neuromuscular junctions. *Semin. Cell Dev. Biol.* 104, 31–38. doi:10.1016/j.semcdb.2020.02.011

Bellmann, J., Goswami, R. Y., Girardo, S., Rein, N., Hosseinzadeh, Z., Hicks, M. R., et al. (2019). A customizable microfluidic platform for medium-throughput modeling of neuromuscular circuits. *Biomaterials* 225, 119537. doi:10.1016/j.biomaterials.2019.119537

Boehm, I., Alhindi, A., Leite, A. S., Logie, C., Gibbs, A., Murray, O., et al. (2020). Comparative anatomy of the mammalian neuromuscular junction. *J. Anat.* 237 (5), 827–836. doi:10.1111/joa.13260

Clerc, P., Lipnick, S., and Willett, C. (2016). A look into the future of ALS research. *Drug Discov. Today* 21 (6), 939–949. doi:10.1016/j.drudis.2016.02.002

de Jongh, R., Spijkers, X. M., Pasteuning-Vuhman, S., Vulto, P., and Pasterkamp, R. J. (2021). Neuromuscular junction-on-a-chip: ALS disease modeling and read-out development in microfluidic devices. *J. Neurochem.* 157 (3), 393–412. doi:10.1111/jnc.15289

Demestre, M., Orth, M., Fohr, K. J., Achberger, K., Ludolph, A. C., Liebau, S., et al. (2015). Formation and characterisation of neuromuscular junctions between hiPSC derived motoneurons and myotubes. *Stem Cell Res.* 15 (2), 328–336. doi:10.1016/j.scr.2015.07.005

Faustino Martins, J. M., Fischer, C., Urzi, A., Vidal, R., Kunz, S., Ruffault, P. L., et al. (2020). Self-organizing 3D human trunk neuromuscular organoids. *Cell Stem Cell* 27 (3), 172–186. doi:10.1016/j.stem.2019.12.007

Gunther, R., Pal, A., Williams, C., Zimyanin, V. L., Liehr, M., von Neubeck, C., et al. (2022). Alteration of mitochondrial integrity as upstream event in the pathophysiology of SOD1-ALS. *Cells* 11 (7), 1246. doi:10.3390/cells11071246

Horner, S. J., Couturier, N., Bruch, R., Koch, P., Hafner, M., and Rudolf, R. (2021). hiPSC-derived schwann cells influence myogenic differentiation in neuromuscular cocultures. *Cells* 10 (12), 3292. doi:10.3390/cells10123292

Jones, R. A., Harrison, C., Eaton, S. L., Llavero Hurtado, M., Graham, L. C., Alkhammash, L., et al. (2017). Cellular and molecular anatomy of the human neuromuscular junction. *Cell Rep.* 21 (9), 2348–2356. doi:10.1016/j.celrep.2017.11.008

Kroehne, V., Tsata, V., Marrone, L., Froeb, C., Reinhardt, S., Gompf, A., et al. (2017). Primary spinal OPC culture system from adult zebrafish to study oligodendrocyte differentiation *in vitro*. *Front. Cell Neurosci.* 11, 284. doi:10.3389/fncel.2017.00284

Li, L., Xiong, W. C., and Mei, L. (2018). Neuromuscular junction formation, aging, and disorders. *Annu. Rev. Physiol.* 80, 159–188. doi:10.1146/annurev-physiol-022516-034255

Luningschror, P., Binotti, B., Dombert, B., Heimann, P., Perez-Lara, A., Slotta, C., et al. (2017). Plekhg5-regulated autophagy of synaptic vesicles reveals a pathogenic mechanism in motoneuron disease. *Nat. Commun.* 8 (1), 678. doi:10.1038/s41467-017-00689-z

Madden, L., Juhas, M., Kraus, W. E., Truskey, G. A., and Bursac, N. (2015). Bioengineered human myobundles mimic clinical responses of skeletal muscle to drugs. *Elife* 4, e04885. doi:10.7554/eLife.04885

Maury, Y., Come, J., Piskorowski, R. A., Salah-Mohellibi, N., Chevaleyre, V., Peschanski, M., et al. (2015). Combinatorial analysis of developmental cues efficiently converts human pluripotent stem cells into multiple neuronal subtypes. *Nat. Biotechnol.* 33 (1), 89–96. doi:10.1038/nbt.3049

Mays, T. A., Sanford, J. L., Hanada, T., Chishti, A. H., and Rafael-Fortney, J. A. (2009). Glutamate receptors localize postsynaptically at neuromuscular junctions in mice. *Muscle Nerve* 39 (3), 343–349. doi:10.1002/mus.21099

Murray, L. M., Talbot, K., and Gillingwater, T. H. (2010). Review: Neuromuscular synaptic vulnerability in motor neurone disease: Amyotrophic lateral sclerosis and spinal muscular atrophy. *Neuropathol. Appl. Neurobiol.* 36 (2), 133–156. doi:10.1111/j.1365- 2990.2010.01061.x

Nagashima, T., Hadiwidjaja, S., Ohsumi, S., Murata, A., Hisada, T., Kato, R., et al. (2020). *In vitro* model of human skeletal muscle tissues with contractility fabricated by immortalized human myogenic cells. *Adv. Biosyst.* 4 (11), e2000121. doi:10.1002/adbi. 202000121

Naujock, M., Stanslowsky, N., Bufler, S., Naumann, M., Reinhardt, P., Sterneckert, J., et al. (2016). 4-Aminopyridine induced activity rescues hypoexcitable motor neurons from amyotrophic lateral sclerosis patient-derived induced pluripotent stem cells. *Stem Cells* 34 (6), 1563–1575. doi:10.1002/stem.2354

Osaki, T., Uzel, S. G. M., and Kamm, R. D. (2018). Microphysiological 3D model of amyotrophic lateral sclerosis (ALS) from human iPS-derived muscle cells and optogenetic motor neurons. *Sci. Adv.* 4 (10), eaat5847. doi:10.1126/sciadv.aat5847

Pereira, J. D., DuBreuil, D. M., Devlin, A. C., Held, A., Sapir, Y., Berezovski, E., et al. (2021). Human sensorimotor organoids derived from healthy and amyotrophic lateral sclerosis stem cells form neuromuscular junctions. *Nat. Commun.* 12 (1), 4744. doi:10.1038/s41467-021-24776-4

Perrin, S. (2014). Preclinical research: Make mouse studies work. *Nature* 507 (7493), 423–425. doi:10.1038/507423a

Reinhardt, P., Glatza, M., Hemmer, K., Tsytsyura, Y., Thiel, C. S., Hoing, S., et al. (2013). Derivation and expansion using only small molecules of human neural progenitors for neurodegenerative disease modeling. *PLoS One* 8 (3), e59252. doi:10.1371/journal.pone.0059252

Sanes, J. R., and Lichtman, J. W. (1999). Development of the vertebrate neuromuscular junction. *Annu. Rev. Neurosci.* 22, 389–442. doi:10.1146/annurev.neuro.22.1.389

Schenke, M., Schjeide, B. M., Puschel, G. P., and Seeger, B. (2020). Analysis of motor neurons differentiated from human induced pluripotent stem cells for the use in cell-based botulinum neurotoxin activity assays. *Toxins (Basel)* 12 (5), 276. doi:10.3390/ toxins12050276

Selvaraj, B. T., Livesey, M. R., Zhao, C., Gregory, J. M., James, O. T., Cleary, E. M., et al. (2018). C9ORF72 repeat expansion causes vulnerability of motor neurons to Ca(2+)-permeable AMPA receptor-mediated excitotoxicity. *Nat. Commun.* 9 (1), 347. doi:10.1038/s41467-017-02729-0

Slater, C. R. (2008). Structural factors influencing the efficacy of neuromuscular transmission. *Ann. N. Y. Acad. Sci.* 1132, 1–12. doi:10.1196/annals.1405.003

Slater, C. R. (2017). The structure of human neuromuscular junctions: Some unanswered molecular questions. *Int. J. Mol. Sci.* 18 (10), 2183. doi:10.3390/ijms18102183

Steinbeck, J. A., Jaiswal, M. K., Calder, E. L., Kishinevsky, S., Weishaupt, A., Toyka, K. V., et al. (2016). Functional connectivity under optogenetic control allows modeling of human neuromuscular disease. *Cell Stem Cell* 18 (1), 134–143. doi:10.1016/j.stem.2015. 10.002

Stoklund Dittlau, K., Krasnow, E. N., Fumagalli, L., Vandoorne, T., Baatsen, P., Kerstens, A., et al. (2021). Human motor units in microfluidic devices are impaired by FUS mutations and improved by HDAC6 inhibition. *Stem Cell Rep.* 16, 2213–2227. doi:10.1016/j.stemcr.2021.03.029

Yu, J., Vodyanik, M. A., Smuga-Otto, K., Antosiewicz-Bourget, J., Frane, J. L., Tian, S., et al. (2007). *Induced pluripotent stem cell lines derived from human somatic cells*. New York, NY: Science, 318 (5858), 1917–1920. doi:10.1126/science.1151526

7.2 Manuscript II: Plekhg5 regulates the unconventional secretion of Sod1 by presynaptic secretory autophagy

Plekhg5 regulates the unconventional secretion of Sod1 by presynaptic secretory autophagy

Amy-Jayne Hutchings[1*], Bita Massih[1*], Alexander Veh[1*], Neha Jadhav Giridhar[1], Christina Angerer[1], Thorben Ohnesorge[1], Maren Schenke[2, 3], Bhuvaneish T. Selvaraj[4], Siddharthan Chandran[4], Jared Sterneckert[5,6], Susanne Petri[7], Bettina Seeger[2], Michael Briese[1], Christian Stigloher[8], Andreas Hermann[9,10,11], Markus Damme[12], Michael Sendtner[1], Patrick Lüningschrör[1, 13]

[1] Institute of Clinical Neurobiology, University Hospital Würzburg, Germany
[2] Institute for Food Quality and Safety, Research Group Food Toxicology and Alternative/Complementary Methods to Animal Experiments, University of Veterinary Medicine Hannover, Hannover, Germany
[3] Bloomberg School of Public Health, Center for Alternatives to Animal Testing, Johns Hopkins University, Baltimore, MD, United States
[4] Centre for Clinical Brain Sciences, University of Edinburgh, Edinburgh EH16 4SB, UK; UK Dementia Research Institute at University of Edinburgh, University of Edinburgh, Edinburgh EH16 4SB, UK; Anne Rowling Regenerative Neurology Clinic, University of Edinburgh, Edinburgh EH16 4SB, UK
[5] Center for Regenerative Therapies TU Dresden, Fetscherstr. 105, 01307, Dresden, Germany
[6] Medical Faculty Carl Gustav Carus of TU Dresden, Dresden, Germany
[7] Department of Neurology, Hannover Medical School, Hannover, Germany
[8] Imaging Core Facility, Biocenter, University of Würzburg, 97074 Würzburg, Germany
[9] Translational Neurodegeneration Section Albrecht-Kossel, Department of Neurology, University Medical Center Rostock, Germany
[10] Center for Transdisciplinary Neurosciences Rostock, University Medical Center Rostock, Rostock, Germany
[11] Deutsches Zentrum für Neurodegenerative Erkrankungen (DZNE) Rostock/Greifswald, 18147 Rostock, Germany
[12] Institute of Biochemistry, Christian-Albrechts-University Kiel, Olshausenstr. 40, 24098, Kiel, Germany
[13] Lead contact
* These authors contributed equally

Correspondence: Lueningsch_P@ukw.de

Abstract

Increasing evidence suggests an essential function for autophagy in unconventional protein secretion (UPS). However, despite its relevance for the secretion of aggregate-prone proteins, the mechanisms of secretory autophagy in neurons have remained elusive. Here we show that the lower motoneuron disease-associated protein Plekhg5 drives the UPS of Sod1. Mechanistically, Sod1 is sequestered into the intermembrane space of autophagosomes which fuse with secretory lysosomal-related organelles (LROs). Deletion of *Plekhg5* in mice disrupts the secretion of these LROs causing Sod1 accumulation at swollen presynaptic sites. A reduced secretion of toxic ALS-linked $SOD1^{G93A}$ following deletion of *Plekhg5* in $SOD1^{G93A}$ mice accelerated disease onset while prolonging survival due to an attenuated microglia activation. Using human isogenic iPSC-derived motoneurons we show an impaired secretion of ALS-linked $SOD1^{D90A}$, which coincided with a reduced PLEKHG5 expression. Our findings highlight an unexpected pathophysiological mechanism that converges two motoneuron disease-associated proteins into a common pathway.

Introduction

Autophagy is an essential cellular degradation pathway. In neurons, autophagy contributes to the maintenance of global proteostasis [1, 2] but is also tightly linked to activity-related pre- and postsynaptic processes [3-6]. Besides its well-characterized role in feeding lysosomes with cargo material for degradation, there is an emerging role of autophagy in unconventional protein secretion (UPS) [7]. Cytosolic proteins that do not contain an N-terminal signal sequence for conventional secretion via the ER and Golgi are released from cells by UPS [8]. During secretory autophagy, autophagosomes serve as vesicle carriers to deliver these proteins to the extracellular milieu [7]. However, before fusing with the plasma membrane, the autophagosomes may transit through the endo/lysosomal pathway and fuse with multi-vesicular bodies, endosomes or lysosomes, possibly generating a vast diversity of secretory vesicle carriers. [9]. Recent work has linked the UPS to the secretion of aggregate-prone proteins, such as amyloid beta and hyperphosphorylated tau in Alzheimer's disease, mutant huntingtin in Huntington's disease, and superoxide dismutase 1 (SOD1) and TDP43 in Amyotrophic Lateral Sclerosis (ALS) [10-15]. However, the molecular mechanisms and the disease relevance of UPS and secretory autophagy are poorly understood.

Pleckstrin homology domain-containing family member 5 (PLEKHG5) is a guanine exchange factor (GEF) predominantly expressed in the nervous system [16]. Plekhg5 regulates the autophagy of synaptic vesicles by activating Rab26, a small GTPase enriched on synaptic vesicles [17, 18]. Mutations in the human *PLEKHG5* gene have been linked to several forms of motoneuron disease (MND) [19-27]. Initially, a single homozygous missense mutation had been identified in an individual extended consanguineous African family diagnosed with a unique form of autosomal recessive lower MND with

childhood-onset (distal spinal muscular atrophy, DSMA4) [24]. More recently, additional *PLEKHG5* mutations were frequently identified in patients suffering from autosomal recessive intermediate Charcot-Marie-Tooth disease (CMT), DSMA, and distal hereditary motor neuropathy (dHMN) [25-27]. Moreover, a variant in the *PLEKHG5* gene was identified as a disease modifier in a family with *TARDBP*-linked ALS, which had a rapidly progressing disease with early onset [28]. Taken together, *PLEKHG5* has emerged as a critical factor in preserving the integrity and function of motoneurons (MNs) and the peripheral nervous system. However, besides its role in synaptic vesicle autophagy, not much is known about the function of Plekhg5.

Here, we present an unexpected link between Plekhg5 and Sod1, one of the most frequently mutated proteins in familial ALS [29]. We show that Sod1 accumulates within axons terminals in the spinal cord and MN terminals in skeletal muscle of Plekhg5-deficient mice. Plekhg5 depletion in cultured MNs and NSC-34 cells resulted in a reduced secretion of Sod1. Mechanistically, our data suggest that Sod1 is translocated into an autophagosomal vesicle intermediate, which transients through the endo/lysosomal system before fusion with the plasma membrane. Depletion of Plekhg5 leads to an enrichment of Sod1 in vesicle carriers indicating that the translocation into the carrier is independent of Plekhg5. Based on confocal-, high-resolution and immunoelectron microscopy (iEM) we conclude that Sod1 accumulates in the intermembrane space of autophagic carriers in Plekhg5-deficient mice. To study the relevance of this mechanism for the pathophysiology of MND, we crossed Plekhg5-deficent mice with $SOD1^{G93A}$ ALS mice. Depletion of Plekhg5 from $SOD1^{G93A}$ mice resulted in prolonged survival but an accelerated disease onset. Using RNAseq and histology, we identified an attenuated microglial activation in Plekhg5-depleted $SOD1^{G93A}$ due to the reduced binding of extracellular mutant $SOD1^{G93A}$ to microglia. Moreover, we used ALS-patient derived induced pluripotent stem cells (iPSCs) to study the secretion of mutant ALS-linked SOD1 expressed at physiological levels. We found that $SOD1^{D90A}$ MNs displayed a reduced secretion of SOD1 compared to their corrected isogenic wildtype counterpart. Notably, the reduced secretion coincided with reduced expression levels of PLEKHG5.

In summary, we provide evidence for an unexpected pathophysiological mechanism involving secretory autophagy. Disruption of this pathway by Plekhg5 depletion results in deleterious vesicle accumulation including Sod1. The interplay between Plekhg5 and Sod1 connects two different facets of MNDs into one coherent pathway.

Results

Plekhg5 depletion results in intracellular Sod1 accumulation due to impaired secretion

Previous work found that Plekhg5 depletion in mice leads to synaptic vesicle accumulations in MN terminals and peripheral nerves of Plekhg5-deficient mice [17, 30]. However, it has not been explored whether synaptic vesicles are the only cargo material which is affected by Plekhg5-dependent autophagy.

We analyzed the vesicle accumulations in Plekhg5-deficient mice in more detail, and found, to our surprise, intracellular accumulations of endogenous Sod1 in spinal cord cross section of Plekhg5-deficient mice (Fig. 1 A, B). Notably, these accumulations appeared without overexpression of human ALS-linked mutant SOD1. Sod1 accumulations were present throughout the different areas of the spinal cord, including the ventral horn (Fig. 1 A). We also detected clustering of Sod1 within axon terminals of MNs at neuromuscular junctions (NMJs) (Fig. 1 C). However, Sod1 accumulations were absent from somata of neurons (Fig. 1 D). To confirm the neuronal origin of the Sod1 accumulations within the spinal cord, we crossed Plekhg5-deficient mice with Thy1::YFP mice to label individual neurons. Using this strategy, we detected Sod1 accumulation in proximal and distal parts of YFP-labeled axons, confirming the intracellular localization of these accumulations in axons (Fig. 1 E, F). To assess whether the Sod1 accumulations represent an insoluble aggregated species of Sod1, we biochemically separated the insoluble proteins from the Triton-X 100 soluble fraction and analyzed the Sod1 levels in both fractions by Western blot (Fig.1 G). We detected significantly elevated levels of Sod1 in Triton-X 100 soluble fractions of spinal cord lysates, but not in the insoluble fractions (Fig.1 H).

Next, we investigated how Plekhg5 depletion affects the turnover of Sod1. Previous studies showed that Sod1 is sequestered by the autophagosomal/lysosomal pathways, but also by the proteosome [31-34]. However, Sod1 is a cleavage-resistant protein, which appeared stable in lysosomes compared to carbonic anhydrase III, another cytosolic protein [34]. Furthermore, Sod1 can be secreted from cells [14, 35]. We therefore analyzed the levels of Sod1 in cell lysates and medium of both cultured primary MNs and NSC34 cells upon sh-RNA-mediated depletion of Plekhg5 (Fig. 1 I-K). We observed significantly reduced levels of secreted SOD1, and correspondingly elevated Sod1 levels in cell lysates in both cell types. (Fig. 1 L). Taken together, these results suggest that Plekhg5 regulates the secretion of Sod1. Disruption of this pathway *in vivo* causes Sod1 accumulations predominantly within axons.

The secretion of Sod1 in motoneurons is autophagy dependent.

Previously, different pathways for the secretion of overexpressed wildtype and mutant ALS-linked Sod1 have been proposed [14, 35, 36]. It has been suggested that Sod1 is secreted in an exosome-dependent manner [35, 36], or via UPS following a similar pathway as Acb1 [14]. Due to its stability in lysosomes [33, 34], we hypothesized that Sod1 might be released by secretory autophagy to prevent the accumulation in lysosomes and to maintain the proteostasis as recently suggested [37].

Treatment with the autophagy inhibitor 3-MA caused a significant reduction of the basal Sod1 secretion in NSC-34 cells (Fig. 2 A, C). Inhibition of exosome release using the neutral sphingomyelinase inhibitor GW4869 had no effects on the Sod1 secretion (Fig. 2 B, C). In agreement with previous results, we detected a marked increase in the Sod1 secretion upon starvation-induced autophagy using HBSS (Fig.2 D) [14].

To determine whether Sod1 secretion requires fully formed autophagosomes we blocked different steps during autophagy biogenesis in primary MNs (Fig. 2 E-Q). Previous work showed that depletion of

Atg9 blocks the generation of the isolation membrane [38]. Lentiviral knockdown of Atg9 in cultured MNs resulted in reduced medium levels of Sod1, without affecting the levels of LC3-II under basal conditions, which is in agreement with previous work (Fig. 2 E-H). We also detected significantly reduced Sod1 medium levels upon Cre-mediated depletion of Atg5 from cultured MNs (Fig. 2 I - L). Depletion of Atg5 resulted in a significant reduction of lipidated LC3-II (Fig. 2 I, J), which indicates that the Sod1 secretion also requires later steps in the autophagosome biogenesis up to the lipidation of LC3. To analyze whether sealing of the autophagosomal membranes is also required for the secretion of Sod1, we simultaneously knocked down Atg2a and Atg2b (Fig. 2 M - Q), which play an essential role in phagophore closure [39]. We tested four combinations of two different sh-RNAs for Atg2a and Atg2b (Fig.2 M). Subsequently, we used two combinations which generated a rather mild (a2+b1) and very efficient (a1+b2) knockdown. Depletion of Atg2a/b in primary MNs caused a slight increase in the LC3-II levels (Fig. 2 N, O). However, to our surprise Atg2a/b depletion did not reduce the Sod1 medium levels (Fig. 2 P, Q), indicating that sealing of the autophagosome is not necessary for the Sod1 secretion. To further examine if autophagy directly drives Sod1 secretion, we applied a membrane fractionation procedure to enrich autophagosomal membranes as described previously (Fig. 2 R) [40]. First, we performed a differential centrifugation to obtain 3K, 25K and 100k membrane pellet fractions (Fig. 2 S). Both, Sod1 and the lipidated form of LC3 (LC3-II) were mainly enriched in the 25k fraction along with Lamp1 (Fig. 2 S). Further separation of the 25k membrane fraction through a sucrose step gradient ultracentrifugation showed that both Sod1 and LC3-II co-distributed in the L fraction at the boundary between the 0.25 M and 1.1 M sucrose layers (Fig. 2 T). Using an OptiPrep gradient we further fractionated the L fraction and observed a co-fractionation of Sod1 and LC3-II (Fig. 2 U). However, Sod1 also co-fractionated with membranes of the endosomal/ lysosomal marker as shown by Rab5 and Lamp1 immunoreactivity (Fig. 2 U). To confirm the presence of Sod1 in autophagosomes, we expressed 3xFlag-LC3 in NSC34 cells and immunoisolated autophagosomes from the 25k fraction by immunoprecipitation (IP). Subsequently, we analyzed the input, flowthrough and IP by Western blot and found that Sod1 co-sedimented with autophagosomes as shown by immunoreactivity for LC3-II (Fig. 2 V). Taken together, these data suggest that a fraction of intracellular Sod1 directly associates with autophagosomes.

Since the Sod1 secretion appears to be unaffected upon depletion of Atg2a/b, Sod1 seems to localize to the phagophore in the absence of completed autophagosome formation. Possible explanations for this phenomenon are either the direct translocation into the phagophore at an early stage by heat shock proteins as shown for IL-1β [40], or by fusion of the outer autophagosomal membrane with an endosome or lysosome. In both cases Sod1 should be secreted as a free protein instead of being secreted in membrane-bound organelles. Indeed, differential centrifugation of the media revealed that the majority of Sod1 is present as a free protein (Fig. 2 W, X). As a control, we used Tsg101, which is present on extracellular vesicles and enriched in the 100k pellet (Fig. 2 X).

Sod1 accumulates in the intermembrane space of autophagic carriers in Plekhg5-deficient mice

The vesicular-like staining pattern of Sod1 in Plekhg5-deficient mice suggests that the accumulated fraction of Sod1 is membrane-bound. To validate this hypothesis, we performed subcellular fractionation experiments (Fig. 3 A). We separated the cytosol from membranes by a three-step membrane fractionation procedure and detected an increase of the Sod1 levels in the 25k membrane pellet, but not in the cytosolic Sod1 levels (Fig. 3 A, B).

To characterize the identity of the compartment in which Sod1 accumulates in more detail, we analyzed the $Sod1^+$ vesicle cluster within the spinal cord of Plekhg5-deficient mice by immunohistochemistry using markers for auto- and endolysosomal vesicles. This approach revealed that the majority of Sod1 accumulations stained positive for the late endosomal/ lysosomal marker Lamp1 (Fig. 3 C). A subset of the $Sod1^+$ vesicle clusters also stained double positive for Lamp1 and CathD (Fig. 3 D). We crossed Plekhg5-deficient mice with mRFP-GFP-LC3 reporter mice to examine the presence of the autophagosomal membranes at the Sod1 accumulations (Fig. 3 E). This strategy also allows to discriminate between autophagosomes which appear positive for mRFP and GFP, and autolysosomes, which are only positive for mRFP due to the acidic pH of lysosomes. While the majority of the Sod1 accumulations overlapped with mRFP (Fig. 3 E, F), GFP was only present at a subset of the vesicle clusters (Fig. 3 E, F). From these data we conclude that Sod1 is sequestered into an autophagosomal carrier, which subsequently fuses with late-endosomes and/or lysosomal-related organelles, thereby generating a hybrid organelle. The presence of CathD and the absence of GFP at a subset of the accumulations also suggests that some of these vesicles underwent at least a certain degree of acidification, which is sufficient to quench the GFP signal.

On the ultrastructural level these accumulations appeared as a densely packed, heterogenous vesicle population with mostly double-, but also single-membraned organelles with an uncompacted cytoplasmic material content (Fig. 3 G). The vesicle clusters appeared in direct contact to dendritic spines (Fig. 3 G, highlighted in yellow), which further supports the idea that the vesicle accumulations represent swollen presynaptic terminals as previously reported [17].

Next, we aimed to determine the localization of Sod1 within individual vesicles using high resolution structured illumination microscopy (SIM) (Fig. 3 H-L). To visualize the limiting membrane of the vesicles, we co-stained Sod1 with Lamp1, which resulted in a ring-like staining pattern of Lamp1 (Fig. 3 H, I). As a quantitative readout, we determined the fluorescent intensity of Sod1 surrounded by a $Lamp1^+$ ring structure and the overlapping with Lamp1 itself (Fig. 3 J). Notably, the majority of the Sod1 signal overlapped with the Lamp1 signal itself (Fig. 3 J, K). However, to a lesser extent, we also detected Sod1 punctae within $Lamp1^+$ ring structures (Fig 3 J, L). This observation suggests that Sod1 was mostly absent from the lumen of the vesicles, but rather overlapped with the membrane. To confirm these results, we performed immunoelectron microscopy (iEM) of spinal cord cross-sections and analyzed the localization of Sod1 on the ultrastructural level (Fig. 3 M; Sup. Fig. 1). As observed by

SIM microscopy, Sod1 was absent from the lumen of the autophagic vesicles but localized to the membranes of individual vesicles in Plekhg5-deficient mice (Fig. 3 M). Taken together, these data indicate that Sod1 accumulates in the intermembrane space of an autophagosomal carrier in Plekhg5-deficient mice. This is in agreement with our biochemical data which shows that Sod1 localizes to the phagophore in the absence of phagophore closure and that Sod1 is mostly secreted as a free protein.

Sod1 accumulates in Plekhg5-deficient mice due to an impaired secretion of lysosomal related organelles, but not due to lysosomal dysfunction

It has recently been reported that secretory autophagy maintains the proteostasis upon lysosomal dysfunction [37]. We hypothesized that Sod1 might be emitted by secretory autophagy to prevent the accumulation in lysosomes due to its resistance against enzymatic cleavage [34]. Therefore, we analyzed the secretion of Sod1 in NSC34 cells upon lysosomal disruption by the V-ATPase inhibitor Bafilomycin or a combination of the aspartic protease inhibitor Pepstatin A and the cysteine protease inhibitor E64D (Fig. 4 A, B). Indeed, we detected an enhanced Sod1 secretion upon blockage of lysosomal acidification or inhibition of lysosomal proteolysis, which indicates that Sod1 is secreted in response to lysosomal dysfunction, but not by the lysosomes itself (Fig. 4 C). To exclude that the Sod1 accumulations build-up due to an impaired lysosomal function in Plekhg5-deficient mice we measured the activity of the lysosomal enzymes β-hexosaminidase, β-galactosidase and β-glucuronidase in spinal cord lysates of Plekhg5-deficient mice, but detected no difference compared to lysates from control animals (Fig. 4 D). Furthermore, p62 and Ubiquitin were absent from the $Lamp1^+$ vesicle cluster suggesting that the global proteostasis is unaffected by depletion of Plekhg5 (Fig. 4 E, F). We therefore concluded that the vesicle cluster do not represent dysfunctional autolysosomes which cause the accumulation of Sod1. Instead, we hypothesized that the $Sod1^+Lamp1^+$ vesicles might represent lysosomal-related organelles (LROs), which represent cell-type specific secretory organelles [41]. While the contents and morphology of LROs appears very diverse, and cell type-specific, the small GTPase Rab27 is a common molecule found on the membrane of LROs, but not on genuine lysosomes [41]. Therefore, we co-stained Rab27b, Lamp1 and ChAT to analyze the presence of Rab27b at the membrane of the $Lamp1^+$ vesicles (Fig. 4 G). Indeed, we found that the vesicle cluster stained positive for Rab27b, which was absent from the somata of MNs, confirming that Rab27b is not detectable at conventional lysosomes. To explore the functional involvement of Rab27b in the secretion of Sod1, we expressed mutant variants of Rab27b that interfere with the GTP hydrolysis (Q78L, GTP-locked; constitutive active) and GDP/GTP exchange (T23N, GDP-locked; dominant negative) in NSC-34 and analyzed the levels of Sod1 in the lysate and medium (Fig. 4 H). Whereas no differences in the Sod1 secretion became apparent upon expression of EGFP-Rab27b-QL, we found reduced levels of Sod1 in the medium after expression of EGFP-Rab27b-TN (Fig. 4 I). Taken together, these data suggest that Rab27b is present on the membrane of secretory LROs and its activity is required for the secretion of Sod1.

Plekhg5-depletion in SOD1^{G93A} mice accelerates the disease onset, but extends the survival

To study the effect of Plekkhg5-depletion on the secretion of disease-relevant mutant ALS-linked SOD1, we crossed Plekhg5-deficient mice with the "low copy" SOD1^{G93A} model of ALS. These SOD1^{G93A} mice show a slow disease progression over several months and survive up to 10 months [42]. At that age, Plekhg5-deficient mice do not show any disease symptoms, but vesicle accumulations are already histologically detectable [17].

To determine any changes in the disease course, we measured the disease onset and the survival of *Plekhg5*$^{+/+}$ *SOD1*^{G93A} and *Plekhg5*$^{-/-}$ *SOD1*^{G93A} mice as previously described (Fig. 5 A-E) [43]. We found that depletion of Plekhg5 in *SOD1*^{G93A} mice accelerated the disease onset by 4 weeks (Fig. 4 A), but also extended the survival for 4 weeks (Fig. 5 B). In *SOD1*^{G93A} mice the disease onset became apparent at a mean age of 36 weeks. *Plekhg5* deficiency accelerated the disease onset to a mean age of 32 weeks (Fig. 5 C). Remarkably, the median age of survival was extended from 44 weeks in *SOD1*^{G93A} mice to 48 weeks in *SOD1*^{G93A} *Plekhg5*$^{-/-}$ *SOD1*^{G93A} mice (Fig. 5 D). As a result, the average disease duration was extended from 8 to 16 weeks (Fig. 5 E).

Next, we asked whether Plekhg5 had any effects on the accumulation of the mutant SOD1^{G93A} protein. At the disease onset, we already observed a striking clustering of SOD1^{G93A} in *Plekhg5*$^{-/-}$ *SOD1*^{G93A} mice, whereas *Plekhg5*$^{+/+}$ *SOD1*^{G93A} animals only displayed a sparse accumulation of SOD1^{G93A} (Fig. 5 F). However, with disease progression the number of SOD1^{G93A} clusters increased in *Plekhg5*$^{+/+}$ *SOD1*^{G93A} mice. In contrast, the number of SOD1^{G93A} clusters in *Plekhg5*$^{-/-}$ *SOD1*^{G93A} did not increase anymore. At the endstage, we detected comparable numbers of SOD1^{G93A} accumulations in both genotypes (Fig. 5 F, G). These data suggest that the mutant, ALS-linked SOD1^{G93A} is affected in a similar way by depletion of Plekhg5 than the endogenous wildtype Sod1.

A major pathological hallmark in SOD1^{G93A} mice is the presence of p62^{+} aggregates caused by an impaired global proteostasis [43]. In line with our finding that p62 and Ubiquitin were absent from the Lamp1^{+}Sod1^{+} vesicle cluster in Plekhg5-deficient mice, the depletion of Plekhg5 in SOD1^{G93A} mice did not affect the number of p62 aggregates within the spinal cord (Sup. Fig. 2). Furthermore, p62 was not detectable at Sod1 accumulations in *Plekhg5*$^{-/-}$ SOD1^{G93A} mice (Fig 5 H), but the Sod1 accumulations stained positive for Lamp1 (Fig. 5 I). This data set confirms that the Sod1 accumulations caused by depletion of Plekhg5 are distinct from p62^{+} protein aggregates.

To characterize the effect of Plekhg5 depletion on the *SOD1*^{G93A} model in more detail, we analyzed the MN survival by quantifying the number of ChAT-positive neurons in the ventral horn of the lumbar spinal cord and the denervation and morphology of the NMJs (Sup. Fig. 3, 4). Whereas no change in the MN number was detectable at disease onset (Sup. Fig. 3 A), a loss of MNs became apparent at the endstage (Sup. Fig. 3 B). In *Plekhg5*$^{-/-}$ *SOD1*^{G93A} mice the survival of MNs was slightly, but significantly improved compared to *Plekhg5*$^{+/+}$ *SOD1*^{G93A} mice (Sup. Fig. 3 C). Next, we examined the effect of Plekhg5 depletion on the NMJ degeneration (Sup. Fig. 4). We measured the number of denervated NMJs and the number of swollen, "balloon-like" NMJs, a characteristic phenotype of Plekhg5-deficient mice

(Sup. Fig. 4 A-C) [17]. We found a progressive denervation of the gastrocnemius muscle in *SOD1*^{G93A} during the disease course (Sup. Fig. 4 A, C). At the disease endstage, *Plekhg5*$^{-/-}$ *SOD1*^{G93A} animals retained a higher number of innervated NMJs than their *Plekhg5*$^{+/+}$ *SOD1*^{G93A} counterparts. When we analyzed the morphology of the NMJs in more detail, we detected an age-dependent increase of balloon-like NMJs in *Plekhg5*$^{-/-}$ animals (Sup. Fig. 4 B, C). In addition, *SOD1*^{G93A} mice deficient for Plekhg5 also acquired this phenotype, but surprisingly to a significantly lesser extend as compared to *Plekhg5*$^{-/-}$ animals (Sup. Fig. 4 B, C). In summary, Plekhg5 depletion in *SOD1*^{G93A} mice preserves NMJ innervation at late disease stages. On the other hand, NMJs denervation due to SOD1^{G93A} expression also results in pruning of "balloon-like" terminals.

Plekhg5-depletion in SOD1^{G93A} ameliorates microglial neuroinflammation.

Previous work demonstrated that secreted, mutant ALS-linked SOD1 protein acts as danger-associated molecular patterns (DAMPs) and binds as a ligand to TLR2 receptors driving microglia activation. [44, 45]. We therefore hypothesized that an impaired Sod1 secretion leads to an attenuated microglial neuroinflammation. During disease progression microglia from *SOD1*^{G93A} mice acquire a unique gene-expression signature [46]. To study whether depletion of Plekhg5 in *SOD1*^{G93A} mice caused any changes in this signature, we utilized an unbiased approach and performed RNAseq of total spinal cord RNA (Fig. 5 J).

We compared the transcripts differentially expressed in *SOD1*^{G93A} mice versus wildtype mice, with transcripts differentially expressed in *Plekhg5*$^{-/-}$ *SOD1*^{G93A} mice versus SOD1^{G93A} mice (Fig 5 J). We found a total number of 40 transcripts that were differently expressed in both data sets (Fig 5 J, K). Strikingly, all 34 transcripts, which were upregulated in SOD1^{G93A} mice, were downregulated in *Plekhg5*$^{-/-}$ *SOD1*^{G93A} mice (Fig 5 J, K). Conversely, the expression of all 6 upregulated transcripts in *SOD1*^{G93A} mice was downregulated upon Plekhg5 deficiency (Fig 5 J, K). A comparison with the microglial-specific ALS signature revealed that 18 of the 34 downregulated transcripts overlapped with genes which expression is upregulated during disease progression [46]. To confirm the RNAseq data, we analyzed the changes in the levels of several transcripts by qPCR (Sup. Fig. 5). In addition, we confirmed a reduced microglial activation in *SOD1*^{G93A} mice with Plekhg5 depletion by staining for the microglial markers Iba1 and CD68 (Fig. 5 L). Whereas no microglia activation could be detected in wildtype and Plekhg5$^{-/-}$ animals, we observed a significant increase in the CD68 immunoreactivity in *Plekhg5*$^{+/+}$ *SOD1*^{G93A} mice, which was significantly reduced in *Plekhg5*$^{-/-}$ *SOD1*^{G93A} mice (Fig. 5 L, M). Taken together, these data suggest that the impaired SOD1^{G93A} secretion upon Plekhg5 depletion is also reflected in changes of the neuroinflammatory signature of *SOD1*^{G93A} mice.

The secretion of ALS-linked SOD1^{D90A} is impaired in human iPSC derived MNs

Recently, it has been reported that the secretion of mutant ALS-linked SOD1^{G93A} is reduced compared to its wildtype counterpart upon overexpression in Hela cells [14]. We wondered whether differences in

the secretion of ALS-linked human SOD1 expressed at physiological levels are detectable in human MNs. Therefore, we utilized two previously characterized iPSC lines derived from ALS patients, either harboring a heterozygous R115G mutation or a homozygous D90A mutation in the *SOD1* gene [47, 48]. While the R115G mutation in SOD1 gives rise to structurally unstable proteins, the $SOD1^{D90A}$ mutant protein is structurally stable and has enzymatic activity that is as high as wildtype SOD1 [49]. We compared the secretion of these two mutant SOD1 species to the secretion of wildtype SOD1, which was analyzed in two lines derived from healthy donors (Fig. 6 A, B). We differentiated both iPSC lines to spinal MNs as previously described [48]. Two weeks after maturation, the media and the corresponding lysates were collected, and analyzed by Western blot (Fig. 6).

Whereas the levels of $SOD1^{R115G}$ in the medium only showed a modest decrease, we detected a significantly reduced secretion of $SOD1^{D90A}$. To exclude that the differences in the SOD1 secretion appeared as an artifact due to line-to line variabilities, we used an isogenic line with a corrected $SOD1^{D90A/D90A}$ allele as an additional control (Fig 6. A, B). Compared to its isogenic counterpart, we also observed a reduced secretion of $SOD1^{D90A}$ (Fig 6. A, B).

In order to establish a link between the reduced secretion of $SOD1^{D90A}$ and PLEKHG5, we analyzed the expression levels of PLEKHG5 in the $SOD1^{D90A/D90A}$ line and its isogenic counterpart by Western blot (Fig 6 C). Notably, we found a significantly lower expression of PLEKHG5 in the $SOD1^{D90A/D90A}$line compared to the isogenic control (Fig 6. D), which shows that the reduced secretion of $SOD1^{D90A}$ coincide with the PLEKHG5 expression levels.

In line with this, we also detected a reduced secretion of $SOD1^{WT}$ in MNs derived from control iPSC-line #1 upon sh-RNA mediated knockdown of PLEKHG5 using two different sequences targeting the mRNA of *PLEKHG5* (Fig. 6 E-H). In summary, these findings confirm that the secretion of human SOD1 in (human) iPSC-derived MNs also depends on PLEKHG5.

Discussion

In summary our data show that Plekhg5 regulates the autophagy-dependent UPS of Sod1. Deficiency of Plekhg5 in mice resulted in accumulations of Sod1 predominantly in axons terminating within the spinal cord and MN terminals within the muscle. The restriction of this phenotype to the axon requires the compartmentalized action of Plekhg5, which is in agreement with previous work showing that Plekhg5 drives the autophagy of synaptic vesicles at motoneuron terminals by activating Rab26 [17]. As a result of Plekhg5 depletion, Sod1 accumulates over time in axon terminals of $Plekhg5^{-/-}$ animals. In this context, it is of particular interest that the secretion of Sod1 from synaptosomes is inducible in an activity-dependent manner [50]. Recent work linked degradative autophagy to neuronal activity [6, 51, 52], but it has not yet been addressed, whether secretory autophagy in neurons is linked to their activity in a similar manner.

Mechanistically, we demonstrate that the UPS of Sod1 depends on Atg9 and Atg5, but not on Atg2. These findings suggest that the secretion of Sod1 requires the phagophore generation, and LC3 lipidation

but not phagophore extension and closure. A possible explanation for these findings is the location of Sod1 in the intermembrane space of the double membrane as shown for IL-1β [40]. This idea is supported by our observation that Sod1 is mostly secreted as a free protein. Furthermore, using SIM and iEM microscopy we detected Sod1 at the membrane rather than the lumen of the vesicles accumulating in Plekhg5-deficient mice. Direct translocation into the intermembrane space by heat shock proteins (HSPs) or the injection into the intermembrane space upon fusion with an endosome could result in the localization between the double membrane of an autophagosome. Recently, a conserved acidic domain within Sod1 has been identified as an export signal for UPS [14]. However, it is still unknown how this motif functions and which binding partner is recruited.

Following vesicle sequestration into the autophagosomal carrier, subsequent fusion with the endosomal or lysosomal pathway are possible prior to fusion with the plasma membrane. In line with this, our data show that the $Sod1^{+}$ vesicles undergo fusion with $Lamp1^{+}$ vesicles. A subset of vesicle cluster also stained positive for the lysosomal marker Cathepsin D. The analysis of the mRFP-GFP-LC3 tandem reporter confirmed the autophagosomal origin of these vesicles, but also revealed that roughly 50% of the vesicle cluster showed a certain degree of lysosomal acidification, which was sufficient to quench the GFP signal. However, the vesicle cluster also stained positive for Rab27b, a small GTPase which is detected on secretory LROs, but not on genuine lysosomes. Furthermore, LROs located in the periphery show a lower pH than conventional lysosomes and possess a limited degradative capacity, if at all [41]. Therefore, we conclude that the membrane carrier in which Sod1 accumulates upon depletion of Plekhg5 represents a secretory LRO rather than a conventional lysosome/autolysosome. This is further supported by our EM data which confirm the absence of conventional, electron-dense lysosomes at the vesicle cluster. In addition, we show an unaltered lysosomal enzyme activity in Plekhg5-deficient mice. In combination with the absence of p62 and Ubiquitin these data demonstrate proper lysosome function in Plekhg5-deficient mice. Thus, we propose that Sod1 is sequestered into an autophagosome which feds the secretory LRO with material for secretion and thereby acquires autophagosomal markers. Plekhg5 depletion disrupts the secretion which causes the accumulations of Sod1. Such a mechanism could be particularly relevant for cleavage-resistant proteins like Sod1.

To address if Plekhg5-mediated Sod1 secretion is also relevant for the disease course of ALS-linked Sod1 mutations, we generated *Plekhg5*$^{-/-}$ *SOD1*^{G93A} mice. Although *Plekhg5*$^{-/-}$ *SOD1*^{G93A} mice showed a markedly accelerated accumulation of $SOD1^{G93A}$ vesicles and a preponed disease onset, the survival of Plekhg5 depleted *SOD1*^{G93A} mice was extended compared to their *Plekhg5*$^{+/+}$ *SOD1*^{G93A} counterparts. Interestingly, a similar phenotype was observed in *Sod1*^{G93A} mice with a MN specific depletion of autophagy [53]. Notably, these animals displayed an attenuated microglia activation, which indicates that some autophagy-dependent processes in MNs drive microglial neuroinflammation in a non-autonomous manner. It is tempting to speculate that the underlying mechanism involves secretory autophagy, which mediates the release of mutant SOD1. Once released, the mutant SOD1 protein acts as a DAMP and binds to TLR2 receptors on microglia [44, 45]. Thus, an impaired secretion of SOD1

causes less microglia activation, attenuating neuroinflammation. However, the accumulation of intracellular, axonal SOD1 most likely impairs MN function leading to earlier disease onset.

To explore the effect on ALS-linked mutations on the secretion of SOD1, we utilized human iPSCs derived from ALS patients carrying SOD1 mutations. This strategy ensures that SOD1 is expressed at physiological levels. We investigated MNs derived from iPSCs carrying a heterozygous R115G mutation, and a second set of iPSCs with a homozygous D90A mutation. Interestingly, the reduction in the secretion of $SOD1^{D90A}$ was more pronounced compared to $SOD1^{R115G}$. $SOD1^{D90A}$ showed a significantly reduced secretion compared to wildtype SOD1, which we analyzed in two control lines from healthy donors, but most importantly also compared to its corrected, isogenic counterpart. A possible explanation for the different behavior of these mutations could be their different structural properties. While the R115G mutation in *SOD1* gives rise to structurally unstable proteins, the $SOD1^{D90A}$ mutant protein is structurally stable and has enzymatic activity that is as high as wildtype SOD1 [49]. However, the D90A mutation is closely located to the acidic amino acid stretch which has been identified as an export signal and might affect the recognition of the yet unidentified binding partner. Furthermore, the double-substitution DE77/78AA within the acidic motif of SOD1, which blocked the secretion of SOD1 caused a similar, markedly increased mobility of SOD1 in the SDS-PAGE as the ALS-linked D90A form. This suggests similarities in the alterations of the polypeptide properties which could affect the export. In addition, we also detected a reduced expression of PLEKH5 in $SOD1^{D90A}$ MNs, which coincides with the impaired secretion of $SOD1^{D90A}$.

The convergence of SOD1 and Plekhg5 to a common pathophysiological mechanism is of particular interest because both proteins have previously been linked to different forms of MND. The diversity of gene mutations causative for fALS makes it challenging to identify common disease mechanisms. Thus, a pathogenetic mechanism directly affecting at least two MND associated proteins provides valuable insight into how different, unrelated proteins converge into a common pathway. Given the increasing number of *PLEKHG5* mutations which have been linked to different forms of MND, PLKEKHG5 emerges as one of the key players for preserving the function of MNs and the peripheral nervous system.

References

1. Komatsu, M., et al., *Loss of autophagy in the central nervous system causes neurodegeneration in mice.* Nature, 2006. **441**(7095): p. 880-4.
2. Hara, T., et al., *Suppression of basal autophagy in neural cells causes neurodegenerative disease in mice.* Nature, 2006. **441**(7095): p. 885-9.
3. Luningschror, P. and M. Sendtner, *Autophagy in the presynaptic compartment.* Curr Opin Neurobiol, 2018. **51**: p. 80-85.
4. Vijayan, V. and P. Verstreken, *Autophagy in the presynaptic compartment in health and disease.* J Cell Biol, 2017. **216**(7): p. 1895-1906.
5. Hill, S.E. and D.A. Colon-Ramos, *The Journey of the Synaptic Autophagosome: A Cell Biological Perspective.* Neuron, 2020. **105**(6): p. 961-973.
6. Decet, M. and P. Verstreken, *Presynaptic Autophagy and the Connection With Neurotransmission.* Front Cell Dev Biol, 2021. **9**: p. 790721.
7. Ponpuak, M., et al., *Secretory autophagy.* Curr Opin Cell Biol, 2015. **35**: p. 106-16.
8. Kim, J., H.Y. Gee, and M.G. Lee, *Unconventional protein secretion - new insights into the pathogenesis and therapeutic targets of human diseases.* J Cell Sci, 2018. **131**(12).
9. Buratta, S., et al., *Lysosomal Exocytosis, Exosome Release and Secretory Autophagy: The Autophagic- and Endo-Lysosomal Systems Go Extracellular.* Int J Mol Sci, 2020. **21**(7).
10. Nilsson, P., et al., *Abeta secretion and plaque formation depend on autophagy.* Cell Rep, 2013. **5**(1): p. 61-9.
11. Kang, S., et al., *Autophagy-Mediated Secretory Pathway is Responsible for Both Normal and Pathological Tau in Neurons.* J Alzheimers Dis, 2019. **70**(3): p. 667-680.
12. Burbidge, K., et al., *LGALS3 (galectin 3) mediates an unconventional secretion of SNCA/alpha-synuclein in response to lysosomal membrane damage by the autophagic-lysosomal pathway in human midbrain dopamine neurons.* Autophagy, 2021: p. 1-29.
13. Trajkovic, K., H. Jeong, and D. Krainc, *Mutant Huntingtin Is Secreted via a Late Endosomal/Lysosomal Unconventional Secretory Pathway.* J Neurosci, 2017. **37**(37): p. 9000-9012.
14. Cruz-Garcia, D., et al., *A diacidic motif determines unconventional secretion of wild-type and ALS-linked mutant SOD1.* J Cell Biol, 2017. **216**(9): p. 2691-2700.
15. Iguchi, Y., et al., *Exosome secretion is a key pathway for clearance of pathological TDP-43.* Brain, 2016. **139**(Pt 12): p. 3187-3201.
16. Marx, R., et al., *Tech: a RhoA GEF selectively expressed in hippocampal and cortical neurons.* J Neurochem, 2005. **92**(4): p. 850-8.
17. Luningschror, P., et al., *Plekhg5-regulated autophagy of synaptic vesicles reveals a pathogenic mechanism in motoneuron disease.* Nat Commun, 2017. **8**(1): p. 678.
18. Binotti, B., et al., *The GTPase Rab26 links synaptic vesicles to the autophagy pathway.* Elife, 2015. **4**: p. e05597.
19. Gonzalez-Quereda, L., et al., *Novel PLEKHG5 mutations in a patient with childhood-onset lower motor neuron disease.* Ann Clin Transl Neurol, 2020.
20. Chen, Z., et al., *Novel variants broaden the phenotypic spectrum of PLEKHG5-associated neuropathies.* Eur J Neurol, 2020.
21. Ozoguz, A., et al., *The distinct genetic pattern of ALS in Turkey and novel mutations.* Neurobiol Aging, 2015. **36**(4): p. 1764 e9-18.
22. Kim, H.J., et al., *Mutations in the PLEKHG5 gene is relevant with autosomal recessive intermediate Charcot-Marie-Tooth disease.* Orphanet J Rare Dis, 2013. **8**: p. 104.
23. Azzedine, H., et al., *PLEKHG5 deficiency leads to an intermediate form of autosomal-recessive Charcot-Marie-Tooth disease.* Hum Mol Genet, 2013. **22**(20): p. 4224-32.
24. Maystadt, I., et al., *The nuclear factor kappaB-activator gene PLEKHG5 is mutated in a form of autosomal recessive lower motor neuron disease with childhood onset.* Am J Hum Genet, 2007. **81**(1): p. 67-76.
25. Senderek, J., *PLEKHG5: Merging phenotypes and disease mechanisms in Charcot-Marie-Tooth neuropathy and lower motor neuron disease.* Eur J Neurol, 2021. **28**(4): p. 1106-1107.
26. Gonzalez-Quereda, L., et al., *Novel PLEKHG5 mutations in a patient with childhood-onset lower motor neuron disease.* Ann Clin Transl Neurol, 2021. **8**(1): p. 294-299.

27. Chen, Z., et al., *Novel variants broaden the phenotypic spectrum of PLEKHG5-associated neuropathies.* Eur J Neurol, 2021. **28**(4): p. 1344-1355.
28. Goldstein, O., et al., *A novel mutation in TARDBP segregates with amyotrophic lateral sclerosis in a large family with early onset and fast progression.* Amyotroph Lateral Scler Frontotemporal Degener, 2020. **21**(3-4): p. 280-285.
29. Kim, G., et al., *ALS Genetics: Gains, Losses, and Implications for Future Therapies.* Neuron, 2020. **108**(5): p. 822-842.
30. Luningschror, P., et al., *Absence of Plekhg5 Results in Myelin Infoldings Corresponding to an Impaired Schwann Cell Autophagy, and a Reduced T-Cell Infiltration Into Peripheral Nerves.* Front Cell Neurosci, 2020. **14**: p. 185.
31. Santosa, K.B., et al., *Clinical relevance of terminal Schwann cells: An overlooked component of the neuromuscular junction.* J Neurosci Res, 2018. **96**(7): p. 1125-1135.
32. Kabuta, T., Y. Suzuki, and K. Wada, *Degradation of amyotrophic lateral sclerosis-linked mutant Cu,Zn-superoxide dismutase proteins by macroautophagy and the proteasome.* J Biol Chem, 2006. **281**(41): p. 30524-33.
33. Chang, L.Y., et al., *Molecular immunocytochemistry of the CuZn superoxide dismutase in rat hepatocytes.* J Cell Biol, 1988. **107**(6 Pt 1): p. 2169-79.
34. Rabouille, C., et al., *The differential degradation of two cytosolic proteins as a tool to monitor autophagy in hepatocytes by immunocytochemistry.* J Cell Biol, 1993. **120**(4): p. 897-908.
35. Grad, L.I., et al., *Intercellular propagated misfolding of wild-type Cu/Zn superoxide dismutase occurs via exosome-dependent and -independent mechanisms.* Proc Natl Acad Sci U S A, 2014. **111**(9): p. 3620-5.
36. Silverman, J.M., et al., *Disease Mechanisms in ALS: Misfolded SOD1 Transferred Through Exosome-Dependent and Exosome-Independent Pathways.* Cell Mol Neurobiol, 2016. **36**(3): p. 377-81.
37. Solvik, T.A., et al., *Secretory autophagy maintains proteostasis upon lysosome inhibition.* J Cell Biol, 2022. **221**(6).
38. Kishi-Itakura, C., et al., *Ultrastructural analysis of autophagosome organization using mammalian autophagy-deficient cells.* J Cell Sci, 2014. **127**(Pt 18): p. 4089-102.
39. Velikkakath, A.K., et al., *Mammalian Atg2 proteins are essential for autophagosome formation and important for regulation of size and distribution of lipid droplets.* Mol Biol Cell, 2012. **23**(5): p. 896-909.
40. Zhang, M., et al., *Translocation of interleukin-1beta into a vesicle intermediate in autophagy-mediated secretion.* Elife, 2015. **4**.
41. Barral, D.C., et al., *Current methods to analyze lysosome morphology, positioning, motility and function.* Traffic, 2022. **23**(5): p. 238-269.
42. Acevedo-Arozena, A., et al., *A comprehensive assessment of the SOD1G93A low-copy transgenic mouse, which models human amyotrophic lateral sclerosis.* Dis Model Mech, 2011. **4**(5): p. 686-700.
43. Brenner, D., et al., *Heterozygous Tbk1 loss has opposing effects in early and late stages of ALS in mice.* J Exp Med, 2019. **216**(2): p. 267-278.
44. Gravel, M., et al., *IL-10 Controls Early Microglial Phenotypes and Disease Onset in ALS Caused by Misfolded Superoxide Dismutase 1.* J Neurosci, 2016. **36**(3): p. 1031-48.
45. Zhao, W., et al., *Extracellular mutant SOD1 induces microglial-mediated motoneuron injury.* Glia, 2010. **58**(2): p. 231-43.
46. Chiu, I.M., et al., *A neurodegeneration-specific gene-expression signature of acutely isolated microglia from an amyotrophic lateral sclerosis mouse model.* Cell Rep, 2013. **4**(2): p. 385-401.
47. Gunther, R., et al., *Alteration of Mitochondrial Integrity as Upstream Event in the Pathophysiology of SOD1-ALS.* Cells, 2022. **11**(7).
48. Massih, B., et al., *A 3D cell culture system for bioengineering human neuromuscular junctions to model ALS.* Front Cell Dev Biol, 2023. **11**: p. 996952.
49. Marklund, S.L., et al., *Normal binding and reactivity of copper in mutant superoxide dismutase isolated from amyotrophic lateral sclerosis patients.* J Neurochem, 1997. **69**(2): p. 675-81.

50. Santillo, M., et al., *Evidence of calcium- and SNARE-dependent release of CuZn superoxide dismutase from rat pituitary GH3 cells and synaptosomes in response to depolarization.* J Neurochem, 2007. **102**(3): p. 679-85.
51. Bademosi, A.T., et al., *EndophilinA-dependent coupling between activity-induced calcium influx and synaptic autophagy is disrupted by a Parkinson-risk mutation.* Neuron, 2023.
52. Yang, S., et al., *Presynaptic autophagy is coupled to the synaptic vesicle cycle via ATG-9.* Neuron, 2022. **110**(5): p. 824-840 e10.
53. Rudnick, N.D., et al., *Distinct roles for motor neuron autophagy early and late in the SOD1(G93A) mouse model of ALS.* Proc Natl Acad Sci U S A, 2017. **114**(39): p. E8294-E8303.
54. Forssmann, W.G., et al., *An improved perfusion fixation method for the testis.* Anat Rec, 1977. **188**(3): p. 307-14.
55. Danscher, G., *Histochemical demonstration of heavy metals. A revised version of the sulphide silver method suitable for both light and electronmicroscopy.* Histochemistry, 1981. **71**(1): p. 1-16.
56. **Griebel M., S.D., Stein N., Schukraft N., Tovote P., Blum R., Flath CM.**, *Deep-learning in the bioimaging wild: Handling ambiguous data with deepflash2.* 2021.
57. Wiese, S., et al., *Isolation and enrichment of embryonic mouse motoneurons from the lumbar spinal cord of individual mouse embryos.* Nat Protoc, 2010. **5**(1): p. 31-8.
58. Yu, J., et al., *Induced pluripotent stem cell lines derived from human somatic cells.* Science, 2007. **318**(5858): p. 1917-20.
59. Agrotis, A., et al., *Redundancy of human ATG4 protease isoforms in autophagy and LC3/GABARAP processing revealed in cells.* Autophagy, 2019. **15**(6): p. 976-997.
60. De Lorenzo, F., et al., *CDNF rescues motor neurons in models of amyotrophic lateral sclerosis by targeting endoplasmic reticulum stress.* Brain, 2023.
61. Martin, M., *Cutadapt removes adapter sequences from high-throughput sequencing reads.* 2011.
62. Dobin, A., et al., *STAR: ultrafast universal RNA-seq aligner.* Bioinformatics, 2013. **29**(1): p. 15-21.
63. Liao, Y., G.K. Smyth, and W. Shi, *featureCounts: an efficient general purpose program for assigning sequence reads to genomic features.* Bioinformatics, 2014. **30**(7): p. 923-30.
64. Love, M.I., W. Huber, and S. Anders, *Moderated estimation of fold change and dispersion for RNA-seq data with DESeq2.* Genome Biol, 2014. **15**(12): p. 550.
65. Yu, G., et al., *clusterProfiler: an R package for comparing biological themes among gene clusters.* OMICS, 2012. **16**(5): p. 284-7.
66. Selvaraj, B.T., et al., *C9ORF72 repeat expansion causes vulnerability of motor neurons to Ca(2+)-permeable AMPA receptor-mediated excitotoxicity.* Nat Commun, 2018. **9**(1): p. 347.
67. Naujock, M., et al., *4-Aminopyridine Induced Activity Rescues Hypoexcitable Motor Neurons from Amyotrophic Lateral Sclerosis Patient-Derived Induced Pluripotent Stem Cells.* Stem Cells, 2016. **34**(6): p. 1563-75.
68. Bursch, F., et al., *Altered calcium dynamics and glutamate receptor properties in iPSC-derived motor neurons from ALS patients with C9orf72, FUS, SOD1 or TDP43 mutations.* Hum Mol Genet, 2019. **28**(17): p. 2835-2850.

Methods:

Mice:

Mice were housed at 12/12 h light/dark conditions with constant temperature and humidity. Food and water were provided ad libitum. All mice strains were kept on a C57BL/6 background. All animal experiments were performed in accordance with institutional guidelines of the University clinic Wuerzburg and regulations on animal protection of the German federal law. The original mice strains used in this study are listed in the supplementary table 2.

To assess the phenotype of $SOD1^{G93A}$ mice, we used previously described criteria [17]. We defined the disease onset as the beginning of weight loss after reaching the peak weight and the survival as the age at which disease-associated paralysis prevented a mouse from righting itself after being placed on its side or reaching a weight-loss of >20%.

Immunohistochemistry for muscles

The tibialis anterior and gastrocnemius muscles were dissected, and muscle fibers were separated into continuous fiber strands and post-fixed for 2 h in 4% paraformaldehyde (PFA). Muscles fibers were washed three times with PBS, followed by 0.1 M glycin for 30 min, ammonium acetate puffer for 30 min, and incubated in 10% donkey serum with 0.3% Trition X-100 overnight at 4°C. Three subsequent washing steps with TBS-T containing 0.1% Trition X-100 were performed and the samples were incubated with primary antibodies in blocking solution for 2-3 days at 4°C. The samples were washed three times with TBS-T, incubated with secondary antibodies at RT for 2 h, thoroughly washed with PBS and mounted with FlourSave (Merck, 345789). To visualize postsynaptic Acetylcholine receptors, α-bungarotoxin conjugated to Alexa-488 from Invitrogen (B13422) was used.

Immunohistochemistry for spinal cord sections

Mice were deeply anaesthetized and trans-cardially perfused with 4% PFA. Spinal cords were removed after perfusion, post-fixed for 2 h with 4% PFA and sectional cut with 40 µm thickness at a Leica VT1000S Vibratome. Free-floating spinal cord sections were washed three times with PBS, followed by a 15 min incubation in 0.1 M glycine. Subsequently, the sections were incubated for 30 min in ammonium acetate puffer, washed two times with PBS, and incubated in 10% donkey serum with 0.3% Trition X-100 for 2 h at RT. Three subsequent washing steps with TBS-T containing 0.1% Trition X-100 were performed and the samples were incubated with primary antibodies in blocking solution for 2-3 days at 4°C. Samples were washed three times, and incubated with secondary antibodies at RT for 2 h. After thoroughly washing with PBS, samples were mounted with FlourSave. Acetylcholine receptors were stained with α-bungarotoxin (Invitrogen, B13422) coupled to a 488 fluorophore. Alexa-488-, DyLight-550-, Cy3- and Cy5- conjugated secondary antibodies were obtained from Jackson

Immuno-Research Laboratories. DAPI (Sigma-Aldrich, D9542-5MG) was used for nucleic acid staining. Primary antibodies used for immunohistochemistry are listed in supplementary table 4.

Electron microscopy

Mice were trans-cardially perfused, slightly modified according to Forssmann et al. [54]. Briefly, mice blood was rinsed for 2 min and afterwards fixated with 3% PFA, 3% glutaraldehyde (Serva, 23114.01), 0.5% picric acid (Sigma Aldrich, 197378) in 0.1 M sodium phosphate buffer (PB), pH 7.2 for 10 min. Spinal cord segments were post-fixed 1-2 h at 4 °C and osmicated with 2% OsO4 (VWR, 7436.1) for 2.5 h at 4 °C. Samples were embedded in Araldite and cut into 60-80 nm sections, stained with uranyl acetate for 40 min and lead citrate for 8 min. Sections were imaged at a transmission electron microscope (JEOL JEM-2100) at 200kV and images were recorded with a TVIPS F416 camera.

Immunoelectron microscopy

Mice were trans-cardially perfused with 4% PFA, 0.2% glutaraldehyde, 0.5% picric acid in 0.1 M PB, pH 7.2 for 10 minutes. Spinal cord segments were post-fixed in 4% PFA for 2 h at 4°C. Afterwards, sectional cut with 40-µm thickness at a Leica VT1000S Vibratome. Free-floating samples were washed three times in 0.1 M PB, followed by 30 min 0.1 M glycine, and blocked with 10% donkey serum containing 4% bovine-serum-albumin (Pan biotech, P06-1391025), and 4% cold-water-fish skin (Merck, G7041) in 0.1 M PB for 30 min at RT. Sample were additionally incubated with 0.01% Triton X-100 in 0.1M PB for 15 min. Primary antibody was applied with 10% blocking solution in 0.1M PB overnight and subsequently washed out afterwards. Samples were incubated with secondary antibody in 0.1M PB with 10% blocking solution for 1 hour at RT, washed out and post-fixed in 4% glutaraldehyde for 30 min. Alexa 546 FluoroNanogold (Nanoprobes, 7403) particles were silver intensified in two steps according to Danscher et al. [55]. Briefly, gold particles were silver intensified for 5 and 6 min in fresh developer solution at 38 °C. Silver intensified samples were post-fixed in PB buffered 0.5% OsO4 at 4°C for 15 min and subsequently serial dehydrated in ethanol. Samples were embedded in Epon. Cured Epon blocks were sectioned with 70 nm thickness and contrasted with lead citrate for 10 min and uranyl acetate for 15 min. The samples were imaged at a transmission electron microscope (JEOL JEM-2100) at 200kV and images were recorded with a TVIPS F416 camera. Identical samples without primary antibody were used as controls.

SIM Microscopy

Samples were processed identical to spinal cord immunohistochemistry samples. Additionally, Tetraspecks (Invitrogen, T7280) were applied on new objects slide for chromatic aberration correction. Samples were scanned at a SIM Microscope (Zeiss Elyra S.1 SIM), reconstructed and channels aligned. SIM stacked images were analyzed via deepflash2. Briefly, new models were generated for SOD1

positive ring-like structures and manually controlled. Total fluorescence intensity of Lamp1 signal was quantified at overlapping ring masks and inside of each ring respectively.

Fluorescence signal quantification

Signal quantification was performed by utilizing the ImageJ application in combination with the deepflash2 analysis tool [56]. Five images were manually analyzed by experts, and corresponding masks used for model training. Resulting masks were particle analyzed with ImageJ, quantified, and normalized to the gray matter size of the corresponding spinal cord section.

The Imaris software (7.7x) was used to reconstruct confocal z-stacks as 3D images. Background was filtered by a manually set threshold and quality filters to render fully connected axons.

Primary mouse MN culture

Murine embryonic spinal MNs were isolated and cultured as previously described [57]. Briefly, after dissection of the ventrolateral part of E13 embryos, spinal cord tissues were incubated for 15 min in 0.05% trypsin in Hank's balanced salt solution (HBSS). Cells were triturated and incubated in Neurobasal medium, supplemented with 100 µg/mL Penicillin/Streptomycin/Glutamax (Gibco, 10378016) on Nunclon plates (Thermo Fisher Scientific, 150350) pre-coated with antibodies against the p75 NGF receptor (MLR2, kind gift of Robert Rush, Flinders University, Adelaide, Australia) for 45 min. Plates were washed with Neurobasal medium, and the remaining MNs were recovered from the plate with depolarization solution (0.8% NaCl, 35 mM KCl and 2 mM CaCl2) and collected in full medium (2% horse serum, 1× B-27 in Neurobasal medium with Glutamax). 2-3 spinal cord tissues were collected and pooled for one experimental condition. Cells were plated on four-well dishes (Greiner Bio-One, 627170) pre-coated with poly-ornithine/laminin (Sigma-Aldrich, L2020-1MG).

Cells were cultured in the presence of the neurotrophic factor BDNF (10 ng/ml), and medium was changed every second day. Precipitation experiments were performed on day 7. 16 h before precipitation, medium was replaced by horse serum and BDNF-depleted medium (0.5ml/well).

NSC34 cell culture

NSC34 cells were cultured in Dulbecco's modified Eagle's medium high glucose Glutamax (Gibco, 61965059) containing 10% FCS and 100 µg/mL Penicillin/Streptomycin. For lentiviral transduction, NSC34 cells were incubated with viral particles for 15 min at RT directly before seeding and were transduced a second time after one week. For precipitation experiments and pharmacological assays, 600.000 cells were seeded on six-well dishes pre-coated with collagen (Gibco, A1048301). The next day, medium was replaced by FCS-depleted medium 16 h before precipitation or pharmacological assay (1.5 ml/well).

Human neuroprogenitor cell (NPC) culture

NPCs were cultured as previously described [48]. Briefly, NPC cultures were split about once every week with Accutase (Thermo Fisher, #07920) and expanded for at least 15 passages to achieve pure NPC cultures. NPCs were cultured in neuronal medium consisting of Neurobasal medium (Gibco, #21103049), Dulbecco's modified Eagle's medium F-12 (DMEM/F-12) (Gibco, #21331046), MACS NeuroBrew-21 (Miltenyi Biotech, #130-097-263), N-2 Supplement (Gibco, #17502048) and 100 µg/mL Penicillin/Streptomycin/Glutamax (Gibco, #10378016) supplemented with 3 µM CHIR99021, 0.5 µM PMA, and 150 µM Ascorbic acid (AA) (Sigma, # A92902) was changed every other day.

Human MN culture

For NPC differentiation into MNs, cells were cultured for 9 days in neuronal medium supplemented with 1 µM PMA. On day 2, 1 µM Retinoic acid (Stemcell Technologies, # 72264) was added to the medium. The medium was changed every other day. After 9 days, NPCs were seeded on six-well dishes pre-coated with Matrigel and the medium was switched to neuronal medium supplemented with 10 ng/mL glia-derived neurotrophic factor (GDNF) (Alomone Labs, # G-240), 10 ng/mL brain-derived neurotrophic factor (BDNF) (PeproTech, #450-02), and 500 µM dibutyryl-cAMP (dbcAMP) (Stemcell Technologies, #73886). Experiments were performed on day 14. 16 h before precipitation, the medium was replaced by MACS NeuroBrew-21 and small molecule depleted-neuronal medium (1.5ml/well). Control iPSC-line #1 was provided by Prof. Chandran MNs derived from the iPSC-line IMR90-4 (control iPSC-line #2), originally purchased from WiCell [58], were provided by the lab of Prof. Seeger as pre-differentiated cryostocks. Both iPSC-lines with ALS-linked SOD1 mutations ($SOD1^{R115G}$ and $SOD1^{D90A}$) and the corresponding $SOD1^{D90A}$ isogenic control were provided by Prof. Herrmann as NPCs.

Trichloroacetic acid (TCA) precipitation

Secretion assay was adapted from Cruz-Garcia et al. with minor modifications [14]. Briefly, 1.5 ml or 0.5 ml cell culture medium was collected. Cells were washed with PBS, lysed in 2× Laemmli and boiled at 99 °C for 5 min. Collected medium was centrifuged first at 1,000 g for 5 min and subsequently at 10,000 g for 30 min. 30 µg of BSA (Thermo Scientific) carrier protein and 0.2 ml of 100% trichloroacetic acid (TCA) were added to 1.5 ml medium and were mixed properly. For precipitation experiments with mouse MN medium no BSA was added. Proteins were precipitated on ice at 4 °C for 1 h and centrifuged 16,000 g for 30 min. The pellet was resuspended in 30 µl 2× Laemmli and boiled at 99 °C for 5 min.

Pharmacological Assay

After 16 h starvation, medium was replaced by 1.5 ml fresh supplement-depleted medium with pharmacological inhibitors for 8 h. The following pharmacological inhibitors were used: MG-123 (10 µM, Enzo Life Science, BML-PI102-0005), 3-Methyladenine (5 µM, MedChem Express, HY-19312), Aloxistatin (E64d) (10µg/ml, MedChem Express, HY-100229), Pepstatin A Methyl Ester (10 µg/ml,

Merck, 516485), GW4869 (10 µM, Sigma-Aldrich, D1692). For HBSS (Gibco, 14170138) treatment, medium was replaced by HBSS for 1 h. Proteins were precipitated as described above. The pellet was resuspended in 30 µl 2× Laemmli and boiled at 99 °C for 5 min.

Western Blot

Equal amounts of protein were separated by SDS-PAGE, and transferred to PVDF Membranes (120 V, 45 min, 4°C). Membranes were blocked in TBS-T with 5% milk powder for 2 h at RT, probed with primary antibodies overnight at 4 °C, and incubated with horseradish peroxidase-conjugated secondary antibodies for 1 h at RT. Membranes were washed three times in TBS-T for 15 min and incubated for 5 min with developer reagents (Immobilon, WBKLS0500). Primary antibodies used for Western blot analysis are listed in supplementary table 5. Peroxidase-conjugated secondary antibodies against mouse, rabbit, chicken, rat and guinea pig were obtained from Jackson Immuno-Research Laboratories. Peroxidase-conjugated secondary antibody against goat was obtained from Merck.

Subcellular membrane fractionation

The protocol was adapted and modified from Zhang et al. [40]. NSC34 cells ($10x10^6$ cells/dish in four 15-cm dishes) were cultured to confluence and starved in HBSS for 1 h. Cells were harvested by scraping, and homogenised with 5 ml B1 lysis buffer (20 mM HEPES-KOH, pH 7.2, 400 mM sucrose, 1 mM EDTA, 0.3 mM DTT, and a combination of cOmplete™ Protease Inhibitor Cocktail and PhosSTOP™) (Roche) through a 22G needle (5 ml syringe) until cell lysis of ~90% was achieved, as visualised by Trypan blue staining. The homogenates were subjected to differential centrifugation at 3,000 g (20 min), 25,000 g (30 min), and 100,000 g (45 min, NVT 65 rotor) to collect subcellular fractions at each step. The 25k pellet was further separated by sucrose step gradient centrifugation by resuspending in 1.28 ml of 1.25 M sucrose buffer and overlaying it with 0.85 ml of 1.1 M and 0.5 ml of 0.85 M sucrose buffer. Centrifugation was performed at 120,000 g for 2 h at 4°C (SW32Ti rotor). The membrane layer at the boundary between 0.25/1.1 M (L fraction) and pellet (P) was collected. The L fraction was further resuspended in 19% Optiprep solution and step gradient containing following layers were generated-0.5 ml 22.5%, 1 ml 19% (sample), 0.9 ml 16%, 0.9 ml 12%, 1 ml 8%, 0.5 ml 5% and 0.2 ml 0%. Each density of OptiPrep was prepared by diluting 50% OptiPrep (20 mM Tricine-KOH, pH 7.4, 42 mM sucrose and 1mM EDTA) with a buffer containing 20 mM Tricine-KOH, pH 7.4, 250 mM sucrose and 1mM EDTA. The OptiPrep gradient was centrifuged at 150,000×g for 3 hr (SW32Ti rotor) and subsequently nine fractions were collected from the top. Fractions were diluted with B88 buffer (20 mM HEPES-KOH, pH 7.2, 250 mM sorbitol, 150 mM potassium acetate and 5 mM magnesium acetate) and membranes were collected by centrifugation at 100,000×g for 1 hr. All membrane fractions were normalised to their membrane phosphatidylcholine content and analyzed by western blots.

Immunoisolation of 3xFLAG-LC3

NSC34 cells (10x106 cells/dish, five 15-cm dishes) transduced with FUV-3xFLAG-LC3B were maintained at confluence for 2 days and starved with HBSS for 1 h. The 25,000 g membrane pellet was collected as described above. The pellet was resuspended in 1 ml of immunoisolation buffer (25 mM HEPES, pH 7.4, 140 mM potassium chloride, 5 mM sodium chloride, 2.5 mM magnesium acetate, 50 mM sucrose, and 2 mM EGTA). Resuspended pellets were divided into two equal portions containing Flag M2 beads with or without 0.2 mg/ml 3xFLAG tag-blocking peptides and mixed overnight at 4°C in an end-to-end rotor. Membranes associated with the beads were washed three times with immunoisolation buffer and eluted twice by addition of 0.5 mg/ml 3xFLAG peptide for 0.5 h at RT. Eluates were centrifuged at 100,000g for 50 minutes at 4°C and analyzed by Western blot.

Preparation of detergent-soluble and -insoluble fractions.

Mouse spinal cord were dissected in frozen in liquid nitrogen. Tissues were homogenized in five volumes of ice-cold 0.25 M sucrose buffer (50 mM Tris-HCl pH 7.4, 1 mM EDTA) supplemented with a cOmplete™ Protease Inhibitor Cocktail (Roche). Homogenates were centrifuged at 500g for 10 min at 4°C. Subsequently, supernatants were collected and lysed with an equal volume of cold sucrose buffer containing 1% Triton X-100. Lysates were subjected to centrifugation at 13,000g for 15 min at 4°C to separate supernatants (Triton-X-100 soluble fraction) and pellets. Pellets were resuspended in 1% SDS in PBS (Triton-X-100-insoluble fractions).

Preparation of tissue lysates for lysosomal enzymes activity assays

Spinal cord tissue was homogenized in 20 volumes (vol) of 50mM Tris HCl 50 mM NaCl and 0.1% Triton X100 (vol/vol), incubated on ice for 30 min, and cleared by centrifugation at 13000 rpm for 20 min at 4°C. The specific activity of lysosomal enzymes (β-hexosaminidase, β-glucuronidase, and β-galactosidase) was determined colorimetrically with monosaccharide substrates coupled to p-nitrophenyl under acidic condition. For β-glucuronidase and β-galactosidase, 50 µl of the lysate was incubated with the colorimetric substrates (p-nitrophenyl-β-D-glucuronide and p-nitrophenyl-2-acetamido-2-deoxy-beta-D-glucopyranoside, respectively) for 4 h in a 0.1 M potassium-citrate buffer at pH 4.6, containing 0.08 % NaN3, and 0.2 % BSA. For β-hexosaminidase activity determination, 10 µl of the lysate was incubated for 30 min with the substrate (p-nitrophenyl-2-acetamido-2-deoxy-β-D-glucopyranosid) in the same buffer. The reaction was stopped by the addition of 0.4 M Glycin / NaOH pH 10.4, and the absorption was measured at a wavelength of OD405 nm in a 96-well plate reader.

Plasmid construction

To generate the plasmids for knockdown of Atg9, Atg2a, and Atg2b, different short hairpin (sh)-sequences were synthesized as sense and antisense oligos and cloned into the BamHI and EcoRI restriction sites of pSIH-H1-eGFP. The individual oligo sequences can be found in supplementary table 6.

To generate FUV-3xFLAG-LC3 we cloned the 3xFLAG-LC3 cassette of CMV-3xFLAG-LC3B [59] into the backbone of the FUV-HA-TDP43-WT [60]. CMV-3xFLAG-LC3 was digested by KpnI, and SmaI, and the resulting 1.3 kB insert was purified using the NucleoSpin Gel and PCR Clean-up kit (Macherey Nagel) and blunted using the Anza™ DNA End Repair kit (Thermo Scientific). FUV-HA-TDP43 was digested by BamHI, and EcoRI and the 10 kB backbone was purified using NucleoSpin Gel and PCR Clean-up kit (Macherey Nagel), blunted using the Anza™ DNA Blunt End Kit (Thermo Scientific) and dephosphorylated with FastAP (Thermo Scientific). Subsequently, both fragments were ligated with T4 DNA Ligase (Thermo Scientific).

Lentivirus Production and Transduction

Lentiviral particles were produced by co-transfecting HEK293T cells with the indicated expression and packaging plasmids by calcium phosphate precipitation. The medium was replaced 16 h after transfection. 48 h after transfection the medium was collected the virus was concentrated by ultracentrifugation. For lentiviral transduction, the cells were incubated with viral particles for 10 min at RT directly before plating.

RNA extraction

Dissected spinal cord tissues were frozen in liquid nitrogen and RNA was extracted using the RNeasy Lipid Tissue Mini Kit (Qiagen) according to the manufacturer's instructions. To remove genomic DNA, we performed on-column DNase digestion with the RNase-Free DNase Set (Qiagen) according to manufacturer's instructions.

cDNA synthesis & qPCR

1 µg RNA was reverse transcribed with random hexamers using the first Strand cDNA Synthesis Kit (Thermo Scientific) according to the manufacturer's instructions. Reverse transcription reactions were diluted 1:5 in water and qPCR reactions were set up with the Luminaris HiGreen qPCR Master Mix (Thermo Fisher Scientific) on a LightCycler® 96 (Roche). Relative expression was calculated using the ΔΔCt method.

RNAseq

RNA quality was checked using a 2100 Bioanalyzer with the RNA 6000 Nano kit (Agilent Technologies). The RIN for all samples was ≥8.7. DNA libraries suitable for sequencing were prepared from 500 ng of total RNA with oligo-dT capture beads for poly-A-mRNA enrichment using the TruSeq Stranded mRNA Library Preparation Kit (Illumina) according to manufacturer's instructions. After 12 cycles of PCR amplification, the size distribution of the barcoded DNA libraries was estimated ~310 bp by electrophoresis on Agilent DNA 1000 Bioanalyzer microfluidic chips.

Sequencing of pooled libraries, spiked with 1% PhiX control library, was performed at 33 million reads/sample in single-end mode with 75 nt read length on the NextSeq 500 platform (Illumina) using a High Output sequencing kit. Demultiplexed FASTQ files were generated with bcl2fastq2 v2.20.0.422 (Illumina).

To assure high sequence quality, Illumina reads were quality- and adapter-trimmed via Cutadapt [61] version 2.4 using a cutoff Phred score of 20 in NextSeq mode, and reads without any remaining bases were discarded (command line parameters: --nextseq-trim=20 -m 1 -a AGATCGGAAGAGCACACGTCTGAACTCCAGTCAC). Processed reads were subsequently mapped to the mouse genome (GRCm38.p6) and the cDNA sequence of human SOD1 (NM_000454.4) using STAR [62] v2.7.2b with default parameters based on mouse RefSeq annotation version 108 combined with SOD1 annotation. Read counts on exon level summarized for each gene were generated using featureCounts v1.6.4 from the Subread package [63]. Multi-mapping and multi-overlapping reads were counted strand-specific and reversely stranded with a fractional count for each alignment and overlapping feature (command line parameters: -s 2 -t exon -M -O --fraction). The count output was utilized to identify differentially expressed genes using DESeq2 [64] version 1.24.0. Read counts were normalized by DESeq2 and fold-change shrinkage was applied by setting the parameter "betaPrior=TRUE". Differential expression of genes was assumed at an adjusted p-value (padj) after Benjamini-Hochberg correction < 0.05 and $|\log2FoldChange| \geq 1$. cluster Profiler [65] version 3.12.0 was used to perform functional enrichment analyses based on Kyoto Encyclopedia of Genes and Genomes (KEGG) pathways and Gene Ontology (GO) terms. The *enricher* function was used to perform hypergeometric tests based on lists of significant genes and the *GSEA* function was applied for gene set enrichment analysis considering the DESeq2 log2FoldChange of all analyzed genes.

Supplementary Tables:

Supplementary Table 1 - cell lines:

iPSC Line	Genotype	Reference
34D6 - control iPSC-line #1	WT	[66]
IMR90- control iPSC line #2	WT	[58]
SOD1 R115G	heterozygous R115G	[67]
SOD1 D90A	homozygous D90A	[47]
SOD1 D90A igc - (isogenic control)	WT	[68]

Supplementary Table 2 – mouse strains

Name	Genetic background	Source
Plekhg5$^{-/-}$	B6.Pekgh5/J	[17]
SOD1^{G93A}	B6SJL-TgN(SOD1-G93A)^{dl}1Gur/J	Jackson Lab, #002300
Thy1::YFP	B6.Cg-Tg(Thy1-YFPH)23Jrs/J	Jackson Lab, #003782
mRFP-GFP-LC3	C57BL/6-Tg(CAG-RFP/EGFP/Map1lc3b)1Hill/J	Jackson Lab, #027139

Supplementary Table 3 - plasmids

Name	Reference
pSIH-shLuciferase	[17]
pSIH-shPlekhg5#D	[17]
pSIH-shPlekhg5#E	[17]
pSIH-shAtg9#1	this study
pSIH-shAtg9#2	this study
pSIH-shAtg2a#1	this study
pSIH-shAtg2a#2	this study
pSIH-shAtg2b#1	this study
pSIH-shAtg2b#2	this study
FUV-EGFP-Rab27b-TN	this study
FUV-EGFP-Rab27b-QL	this study
FUV-3xFlag-LC3	this study

Supplementary Table 4 - primary antibodies for immunohistochemistry:

Name	Company	Catalogue number
Synaptophysin-1	Synaptic systems	101 400
Neurofilament heavy	Millipore Sigma	AB5539
SOD1	Enzo Life Science	ADI-SOD-100-F
Lamp1	Invitrogen	14-1071-82
Lamp1	DSHB	1D4B
ChAT	Millipore Sigma	ab144P
GFP	Abcam	ab13970
RFP	Rockland	600-401-379
p62	Progen	GP62-C
CD68	Bio-Rad	MCA1957T
CathD	Santa Cruz Biotechnology	6494
Iba1	Synaptic systems	234 004
Ubiquitin	Agilent Dako	Z0458

Supplementary Table 5 - primary antibodies for Western blot:

Name	Company	Catalogue number
SOD1	Enzo Life Science	ADI-SOD-100-F
Actin	Santa Cruz Biotechnology	Sc-8432
TUJ-1	Neuromics	MO15013
Atg9	Abcam	Ab108338
LC3B	Novus Biologicals	NB100-2220
Atg5	Cell Signaling Technologies	12994
Atg2a	Santa Cruz Biotechnology	Sc-514207
Atg2b	Proteintech	25155-1-AP
Calnexin	SicGen antibodies	AB0041-200
anti-GM130	BD Biosciences	610822
Lamp-1	Invitrogen	14-1071-82
Cytochrome C	Santa Cruz Biotechnology	sc-13156
Tsg101	Proteintech	14497-1-AP
Tsg101	Santa Cruz Biotechnology	sc-7964
Flag M2 Agarose	Millipore Sigma	A2220
Flag	Sigma life sciences	F7425-2MG
Cathepsin D	Davids Biotechnology	Custome made
anti-Adaptin y	BD Biosciences	610385
eIF2α	Cell Signaling Technologies	119A11
Plekhg5	Proteintech	19830-1-AP
Rab5a	Cell Signaling Technologies	#46449

Supplementary Table 6 - oligonucleotides:

Name	Sequence 5´- 3´	Company	Reference
Ccl3 qPCR Fwd	TCT CCT ACA GCC GGA AGA TTC	metabion	this study
Ccl3 qPCR Rev	CTT TGG AGT CAG CGC AGA TC	metabion	this study
Ccl4 qPCR Fwd	TCC CAC TTC CTG CTG TTT CT	metabion	this study
Ccl4 qPCR Rev	ATG TAC TCA GTG ACC CAG GG	metabion	this study
Ccl6 qPCR Fwd	TGC CAC ACA GAT CCC ATG TA	metabion	this study
Ccl6 qPCR Rev	CTC TGA ACT CTC CGA TCG CT	metabion	this study
Ccl9 qPCR Fwd	GCC TGT CCT ATA ACT CAC GGA	metabion	this study
Ccl9 qPCR Rev	TTG TAG GTC CGT GGT TGT GA	metabion	this study
CD68 qPCR Fwd	ACA AAA CCA AGG TCC AGG GA	metabion	this study
CD68 qPCR Rev	CAC ATT GTA TTC CAC CGC CA	metabion	this study
Trem2 qPCR Fwd	ATG CTG GAG ATC TCT GGG TC	metabion	this study
Trem2 qPCRRev	AGA AGA ATG GAG GTG GGT GG	metabion	this study

Name	Sequence 5´- 3´	Company	Reference
Plekhg5$^{-/-}$, Geno Fwd	TAAAAGCTGGCAGCCTGAAT	metabion	[17]
Plekhg5$^{-/-}$, Geno Genetrap-Rev	GCTAGCACAACCCCTCACTC	metabion	[17]
Plekhg5$^{-/-}$, Geno Rev	ACCCCAAGGTCTGTCCTCTT	metabion	[17]

Fwd SOD Ex 4f	CAT CAG CCC TAA TCC ATC TGA	metabion	Jackson Lab, oIMR0113
Rev SOD Ex 4r	CGC GAC TAA CAA TCA AAG TGA	metabion	Jackson Lab, oIMR0114
Thy1::YFP	TCC TTG AAG AAG ATG GTC CG	metabion	Jackson Lab, olMR1416
Thy1::YFP	AAG TTC ATC TGC ACC ACC	metabion	Jackson Lab, olMR0872
$Atg5^{fl/fl}$; 1	GAA TAT GAA GGC ACA CCC CTG AAA TG	metabion	[2]
$Atg5^{fl/fl}$; 2	ACA ACG TCG AGC ACA GCT GCG CAA GG	metabion	[2]
$Atg5^{fl/fl}$; 3	GTA CTG CAT AAT GGT TTA ACT CTT GC	metabion	[2]
mRFP-GFP-LC3 Transgene Fwd A GFP	CAT GGA CGA GCT GTA CAA GT	metabion	Jackson Lab, #24935
mRFP-GFP-LC3 Transgene Rev A Map1LC3B;	CAC CGT GAT CAG GTA CAA GGA	metabion	Jackson Lab, #24936
mRFP-GFP-LC3 Internal positive control Fwd A,	CTA GGC CAC AGA ATT GAA AGA TCT	metabion	Jackson Lab, oIMR7338
mRFP-GFP-LC3 Internal positive control Rev A,	GTA GGT GGA AAT TCT AGC ATC ATC C	metabion	Jackson Lab, oIMR7339

sh-RNA oligonucleotide	Sequence 5´ - 3´	Company	Reference
sh-Atg2a#1 sense	GATCCGTATCTACAACAGGATCAATACTTCCTG TCAGA TATTGATCCTGTTGTAGATAC TTTTTG	metabion	this study
sh-Atg2a#1 antisense	AATTCAAAAAGTATCTACAACAGGATCAATATC TGACAGGAAGTATTGATCCTGTTGTAGATACG	metabion	this study
sh-Atg2a#2 sense	GATCCTATGTCTGTGTCCTGGATATTCTTCCTGT CAGAAATATCCAGGACACAGACATATTTTTG	metabion	this study
sh-Atg2a#2 antisense	AATTCAAAAATATGTCTGTGTCCTGGATATTTCT GACAGGAAGAATATCCAGGACACAGACATAG	metabion	this study
sh-Atg2b#1 sense	GATCCAGAAGTCACTGAAGGATTTATCTTCCTG TCAGAATAAATCCTTCAGTGACTTCTTTTTTG	metabion	this study
sh-Atg2b#1 antisense	AATTCAAAAAAGAAGTCACTGAAGGATTTATTC TGACAGGAAGATAAATCCTTCAGTGACTTCTG	metabion	this study
sh-Atg2b#2 sense	GATCCTTCCAACATGCTGACAATTAACTTCCTGT CAGA TTAATTGTCAGCATGTTGGAATTTTTG	metabion	this study
sh-Atg2b#2 antisense	AATTCAAAAATTCCAACATGCTGACAATTAATC TGACAGGAAGTTAATTGTCAGCATGTTGGAAG	metabion	this study
sh-Atg9#1 sense	GATCCTGTAGGAGCAGGATGGAAATACTTCCTG TCAGATATTTCCATCCTGCTCCTACATTTTTG	metabion	this study

sh-Atg9#1 antisense	AATTCAAAAATGTAGGAGCAGGATGGAAATAT CTGACAGGAAGTATTTCCATCCTGCTCCTACA G	metabion	this study
sh-Atg9#2 sense	GATCCGTGGACTATGACATCCTATTTCTTCCTGT CAGAGTGGACTATGACATCCTATTTTTTTTG	metabion	this study
sh-Atg9#2 antisense	AATTCAAAAAGTGGACTATGACATCCTATTTTC TGACAGGAAGGTGGACTATGACATCCTATTTG	metabion	this study
sh-PLEKHG5#1 sense	GATCCGAATGCTTCACTCTGAAATTTCTTCCTGT CAGAAAATTTCAGAGTGAAGCATTCTTTTTG	metabion	this study
sh-PLEKHG5#1 antisense	AATTCAAAAAGAATGCTTCACTCTGAAATTTTC TGACAGGAAGAAATTTCAGAGTGAAGCATTCG	metabion	this study
sh-PLEKHG5#2 sense	GATCCGAGGTGCTGCTGCCTGTATTTCTTCCTGT CAGAAAATACAGGCAGCAGCACCTCTTTTTG	metabion	this study
sh-PLEKHG5#2 antisense	AATTCAAAAAGAGGTGCTGCTGCCTGTATTTTC TGACAGGAAGAAATACAGGCAGCAGCACCTCG	metabion	this study
sh-PLEKHG5#3 sense	GATCCGACAAGCTCCTGAAGGAATTTCTTCCTG TCAGAAAATTCCTTCAGGAGCTTGTCTTTTTG	metabion	this study
sh-PLEKHG5#3 antisense	AATTCAAAAAGACAAGCTCCTGAAGGAATTTTC TGACAGGAAGAAATTCCTTCAGGAGCTTGTCG	metabion	this study
sh-PLEKHG5#4 sense	GATCCTGGCTGGGTGGACACCATTTACTTCCTGT CAGATAAATGGTGTCCACCCAGCCATTTTTG	metabion	this study
sh-PLEKHG5#4 antisense	AATTCAAAAATGGCTGGGTGGACACCATTTATC TGACAGGAAGTAAATGGTGTCCACCCAGCCAG	metabion	this study

Acknowledgements

We thank Janina Dix for excellent technical support. We are grateful to Hilde Troll for lentiviral and AAV vector production. We thank Regine Sendtner and Sebastian Rose for monitoring of the transgenic animals. We are grateful to Peter Heimann for helpful suggestions on the iEM protocol. PL was supported by the BMBF grants VORAN, 161L0150 and VORAN-2, 16LW066BMBF, and the DFG grant DFG LU 2347/3-1. The JEOL JEM-2100 transmission electron microscope is funded by the Deutsche Forschungsgemeinschaft (DFG, German Research Foundation) – 218894163 and the structured illumination microscope Zeiss Elyra S.1 SIM is funded by DFG – 261184502 (INST 93/823-1 FUGG).

Figure legends

Figure 1. Plekhg5 regulates the secretion of Sod1.

A: Sod1 staining of spinal cord cross sections revealed numerous accumulations of Sod1 in *Plekhg5*$^{-/-}$ mice as compared to *Plekhg5*$^{+/+}$ control animals.

B: Quantification of Sod1 accumulations. *Plekhg5*$^{+/+}$ mice, n=3; *Plekhg5*$^{-/-}$ mice, n=5. Mean±SEM; t-Test, two-tailed.

C: NMJ within the gastrocnemius visualized by BTX and NF-M staining. Note the Sod1 accumulations at the axon terminal of *Plekhg5*$^{-/-}$ mice.

D: Spinal cord cross-section of *Plekhg5*$^{-/-}$ stained for Sod1 and ChAT showing a Sod1 accumulation close to the soma of a MN.

E: Spinal cord cross-sections of *Plekhg5*$^{-/-}$ *Thy1::YFP* mice stained for Sod1 and GFP show the localization of Sod1 accumulations in distal parts of axons.

F: Imaris 3D reconstruction of the image shown in the lower panel of E.

G: Accumulation of Tritin-X-100 soluble Sod1 in the spinal cord of *Plekhg5*$^{-/-}$ mice. Spinal cord homogenates were separated into Triton-X-100-soluble and SDS-soluble fractions and analyzed by Western blot.

H: Quantification of the spinal cord Sod1 levels in the Triton-X-100-soluble and SDS-soluble fraction of *Plekhg5*$^{-/-}$ and *Plekhg5*$^{+/+}$ mice. n=6; Mean±SEM; t-Test, two-tailed.

I: Western blot showing sh-RNA-mediated knockdown of Plekhg5 in primary MNs with two different sequences to target Plekhg5 (sequence#1=#1; sequence#2=#2).

J, K: Western blots showing reduced Sod1 levels in the medium of Plekhg5-depleted primary MNs (J) and Plekhg5-depleted NSC34 cells (K).

L: Western blot quantifications of the Sod1levels upon knockdown of Plekhg5 in primary MNs (J) and NSC34 cells (K). The Sod1 levels were normalized to sh-Luc and set to 1 in each experiment. Mean±SEM. One sample t-test. Lysate n=5, medium n=5 (J); lysate n=5, medium n=3 (K).

Figure 2. Sod1 is secreted in an autophagy-dependent manner.

A, B: Western blots of lysates and media from NSC34 cells treated with 3-MA (A), and GW4689 (B) for 8h. Treatment with 3-MA decreases Sod1 levels in media.

C: Quantification of the Sod1 levels normalized to the untreated condition and set to 1 in each experiment. 3-MA, n=3; GW4689, n=3. Mean±SEM. One-Sample t-test.

D: Amino acid deprivation by starvation in HBSS triggers the secretion of Sod1. Western blot of the lysate and medium from NSC34 cells treated for 1 h with HBSS.

E: Western blot showing similar LC3-I and LC3-II levels upon sh-RNA-mediated knockdown of Atg9 in primary MNs. Two different sequences to target Atg9 were used.

F: Quantification of the LC3-II intensity upon knockdown of Atg9 normalized to Actin. n=4. Mean±SEM. t-test, two-tailed.

G: Reduced Sod1 levels in the medium of primary MNs upon knockdown of Atg9 shown by Western blot.

H: Quantification of the Sod1 intensity. The Sod1 expression was normalized to sh-Luc and set to 1 in each experiment. One sample t-test. Lysate n=3, medium n=3 (sh-Atg9#1); Lysate n=3, medium n=4 (sh-Atg9#2). Mean±SEM. One-sample t-test.

I: Western blot showing reduced levels of LC3-II in primary MNs depleted of Atg5 by Cre-mediated excision of *Atg5*$^{fl/fl}$.

J: Quantification of the LC3-II levels upon depletion of Atg5 normalized to Tuj1. n=4. Mean±SEM. t-test, two-tailed.

K: Depletion of Atg5 in primary MNs results in a reduced secretion of Sod1 as shown by Western blot.

L: Quantification of the Sod1 intensity. The Sod1 expression was normalized to sh-Luc and set to 1 in each experiment. n=3. Mean±SEM. t-test, two-tailed.

M: Western blot showing the simultaneous sh-RNA mediated knockdown of Atg2a and Atg2b in primary MNs. The cells were transduced with different combinations of sh-RNA targeting Atg2a or Atg2b.

N: Western blot analyzes reveals elevated LC3-II levels upon depletion of Atg2a/b.

O: Quantification of the LC3-II levels upon depletion of Atg2a/b normalized to Actin. n=4. Mean±SEM. t-test, two-tailed.

P: Depletion of Atg2a and Atg2b did not affect the secretion of Sod1 in primary MNs as shown by Western blot.

Q: Quantification of the Sod1 intensity. The Sod1 intensity was normalized to sh-Luc and set to 1 in each experiment. n=4. Mean±SEM. One-sample t-test.

R: Membrane fractionation scheme. Briefly, cell lysates were subjected to differential centrifugations at 3000×g (3k), 25,000×g (25k) and 100,000×g (100k). The 25k pellet, in which Sod1 was mainly enriched, was selected and a sucrose gradient ultracentrifugation was performed to separate membranes

in the 25k pellet to the L (light) and P (pellet) fractions. The L fraction, which contained the majority of Sod1, was further resolved on an OptiPrep gradient. Nine fractions were collected from the top.

S-U: Western blots showing the distribution of Sod1 and the indicated membrane markers in the different membrane fractions. T, top; B, bottom.

V: LC3 positive membranes were immunoisolated with anti-FLAG agarose from the 25 k pellet and the presence of Sod1 was determined by Western blot analysis. FT, flowthrough; IP: immunoprecipitation.

W: Scheme for the differential centrifugation protocol used to isolate extracellular vesicles from the media of NSC34 cells. Briefly, the medium was subjected to serial differential ultracentrifugation to recover large (10,000×g; 10k) and small membranes (100,000×g; 100k). Free soluble proteins were precipitated with trichloroacetic acid (TCA).

X: Sod1 is mainly secreted as a free protein in NSC34 cells. Western blot analysis of the input, 10k pellet, 100k pellet and precipitated free soluble proteins (TCA) for Tsg101 and Sod1.

Figure 3. Sod1 accumulates in autophagosomal structures in the spinal cord of Plekhg5-deficient mice.

A: Western blot analysis of membrane (left) and cytosolic fractions (right) reveals an enrichment of Sod1 in the 25k membrane fraction upon Plekhg5 knockdown in NSC34 cells.

B: Quantification of the Sod1 intensity in the 25k membrane and cytosolic fraction. The Sod1 intensity of the 25k pellet was normalized to γ-Adaptin. The Sod1 intensity of the cytosolic fraction was normalized to eIF2α. n=3. Mean±SEM. Two-way ANOVA; Sidak's multiple comparison test.

C: Sod1 accumulations in *Plekhg5*$^{-/-}$ mice stained positive for the endosomal/lysosomal marker Lamp1. Co-staining of spinal cord cross sections from *Plekhg5*$^{+/+}$ and *Plekhg5*$^{-/-}$ mice for Sod1, Lamp1 and DAPI.

D: A subset of Sod1^{+} Lamp1^{+} vesicle cluster showed immunoreactivity for the lysosomal marker CathepsinD. Triple-staining of spinal cord cross sections from *Plekhg5*$^{+/+}$ and *Plekhg5*$^{-/-}$ mice for Sod1, Lamp1, CathD and DAPI. Arrowhead point to vesicle cluster positive for Sod1, Lamp1 and CathD. The asterisk labels a vesicle cluster positive for Sod1 and Lamp1, but negative for CathD.

E: Co-staining of Sod1, mRFP-GFP-LC3 and DAPI in spinal cord cross sections from *Plekhg5*$^{-/-}$ CAG:::mRFP-GFP-LC3 mice.

F: Quantification of Sod1 accumulations reveals an enrichment of Sod1 accumulations positive for RFP^{+}GFP^{-}.

G: Electron microscopic micrograph of a vesicle cluster in *Plekhg5*$^{-/-}$ mice. Post-synaptic spines adjacent to the vesicle cluster are highlighted in orange. Inset 1 shows double membraned organelles. Inset 2 shows smaller organelles with single membranes. Inset 3 shows a postsynaptic spine in direct contact to the vesicle accumulation.

H: High-resolution SIM images of a vesicle cluster labeled for Lamp1 and Sod1 in *Plekhg5*$^{-/-}$ mice.

I: High magnification images of vesicles shown in (H) show that Sod1 overlaps with the ring-like Lamp1 staining (upper panel) or locates to the lumen of Lamp1^{+} vesicle (lower panel).

J: Quantification of the Sod1 intensity reveals that Sod1 mainly overlaps with the Lamp1 signal.

K: Line scan of the vesicle shown in upper panel of I

L: Line scan of the vesicle shown in lower panel of I

M: Immuno-electron microscopic micrographs reveals that Sod1 is absent from the lumen but locates to the intermembrane space of autophagosomes.

Figure 4. Sod1 accumulates in Plekhg5-deficient mice due to an impaired secretion of lysosomal related organelles, but not due to lysosomal dysfunction.

A, B: Elevated Sod1 levels in the medium upon lysosomal dysfunction. Western blots of lysates and media from NSC34 cells treated with Pepstatin A and E64D (A) and Bafilomycin (Baf) (B) for 8h.

C: Quantification of the Sod1 levels normalized to the untreated condition and set to 1 in each experiment. Pep+E64D, n=6; Baf, n=5. Mean±SEM. One-Sample t-test.

D: Quantification of the activity of the lysosomal enzymes ß-hexosaminidase, ß-galactosidase, and ß-glucuronidase in spinal cord lysates reveals no difference between *Plekhg5*$^{+/+}$ and *Plekhg5*$^{-/-}$ mice.

E, F: Lamp1 accumulations in *Plekhg5*$^{-/-}$ mice are negative for p62 (E) and Ubiquitin (F). Co-staining of spinal cord cross sections from *Plekhg5*$^{-/-}$ and *Plekhg5*$^{+/+}$ mice labeled for Lamp1, p62 and DAPI (E) and Lamp1, Ubiquitin and DAPI (F).

G: Lamp2^{+} Rab27b^{+} vesicle cluster in close proximity to a ChAT^{+} MN. Spinal cord cross section from *Plekhg5*$^{-/-}$ and *Plekhg5*$^{+/+}$ mice co-stained fro Lamp2, Rab27 and ChAT.

H: Sod1 levels are decreased in medium of primary MNs expressing dominant negative (TN) Rab27b. Western blot analysis of Sod1 in lysate and medium of primary MNs expressing constitutively active (QL) Rab27b and dominant negative (TN) Rab27b.

I: Quantification of Sod1 intensities normalized to control and set to 1 in all experiments. EGFP-Rab27b-TN, n= 3; EGFP-Rab27b-QL. Mean±SEM. One-Sample t-test.

Figure 5. Depletion of Plekhg5 in *Sod1*^{G93A} prepones the disease onset but extends the survival.

A, B: Kaplan–Meier plots showing the effects of Plekhg5 depletion on the phenotype of *Sod1*^{G93A} mice.

A: The onset of weight loss is accelerated in *Plekhg5*$^{-/-}$ *Sod1*^{G93A} mice compared to *Plekhg5*$^{+/+}$ *Sod1*^{G93A}. Log-rank test.

B: Lifespan is extended in *Plekhg5*$^{-/-}$ *Sod1*^{G93A} mice compared to their *Plekhg5*$^{+/+}$ *Sod1*^{G93A} counterparts. Log-rank test.

C-E: Average disease onset (C), survival (D) and duration (E). Two-tailed t-test. Mean ± SEM. Each dot represents one animal. A-E: *Plekhg5*$^{+/+}$ *Sod1*^{G93A}, n=20. *Plekhg5*$^{-/-}$ *Sod1*^{G93A}, n=12.

F: Sod1 staining of spinal cord cross sections revealed an accelerated accumulation of Sod1 in *Plekhg5*$^{-/-}$ *Sod1*^{G93A} mice compared to *Plekhg5*$^{+/+}$ *Sod1*^{G93A} mice at disease onset and disease endstage.

G: Quantification of Sod1 accumulations. Onset: *Plekhg5*$^{+/+}$ *Sod1*^{G93A}, n=3; *Plekhg5*$^{-/-}$ *Sod1*^{G93A}, n=5. Endstage: *Plekhg5*$^{+/+}$ *Sod1*^{G93A}, n=4; *Plekhg5*$^{-/-}$ *Sod1*^{G93A}, n=4. Mean±SEM. One-way ANOVA; Tukey's Multiple Comparisons.

H, I: Sod1 accumulations in *Plekhg5* $^{-/-}$ Sod1^{G93A} mice stain negative for p62 (H) but positive for Lamp1 (I).

J: Scatterplot showing the magnitude of change (fold change, log2) of the transcripts that were significantly altered in spinal cord of SOD1^{G93A} vs. wildtype (WT) mice and significantly altered in SOD1^{G93A} mice vs. Plekhg5$^{-/-}$ SOD1^{G93A}. Total RNA was extracted from spinal cord of three mice per genotype. Pearson correlation, r=-0.9390.

K: Heat Map showing the relative expression levels of transcripts that were significantly altered in spinal cord of SOD1^{G93A} vs. wildtype (WT) mice and significantly altered in SOD1^{G93A} mice vs. Plekhg5$^{-/-}$ SOD1^{G93A}. The expression levels are shown as fold change normalized to the mean levels of Plekhg5$^{+/+}$ (WT) mice.

L: Staining for Iba1 and CD68 spinal cord reveals a reduced microglial neuroinflammation in *Plekhg5*$^{-/-}$ *Sod1*^{G93A}.

M: Quantification of CD68 immunoreactivity. *Plekhg5*$^{+/+}$, n=3; *Plekhg5*$^{-/-}$, n=5; *Plekhg5*$^{+/+}$ *Sod1*^{G93A}, n=4; *Plekhg5*$^{-/-}$ *Sod1*^{G93A}, n=3. One-way ANOVA; Tukey's Multiple Comparisons.

Figure 6. Impaired secretion of SOD1^{D90A} in human iPSC-derived MNs.

A: Western blots showing reduced SOD1 levels in the medium of iPSC-derived MNs with SOD1$^{D90A/D90A}$ mutation.

B: Western blot quantification of the SOD1 intensity. The SOD1 intensity of SOD1$^{R115G/WT}$ MNs was normalized to the mean value of both controls and set to 1 in each experiment. The SOD1 intensity of SOD1$^{D90A/D90A}$ MNs was normalized to its corrected counterpart and set to 1 in each experiment. n=8 Mean±SEM. One-sample t-test.

C: Western blots showing reduced PLEKHG5 levels in the lysate of Sod1$^{D90A/D90A}$ MNs.

D: Western blot quantification of the PLEKHG5 intensity relative to Tuj1. n= 7. Paired t-test, two-tailed.

E: Western blot to test different sh-sequences to knockdown PLEKHG5 in human cells. PLEKHG5-Flag was expressed in 293FT cells along with the sh-sequence indicated. Sequences #1 and #3 were used in subsequent experiments.

F: Western blot showing sh-RNA-mediated knockdown of PLEKHG5 in control#1 MNs with two different sequences to target PLEKHG5 (sequence#1 and sequence#3).

G: Western blot showing reduced SOD1 levels in the medium of PLEKHG5-depleted MNs.

H: Western blot quantification of the SOD1 intensity. The SOD1 intensity was normalized to control and set to 1 in each experiment. Mean±SEM. One sample t-test. Lysate n=3, medium n=3.

Supplementary Figure 1. Sod1 accumulates in the spinal cord of Plekhg5-deficient mice in the intermembrane space of autophagosomes.

Immuno-electron microscopic micrographs of spinal cord cross-sections of Plekhg5-deficient mice reveal that Sod1 locates to the intermembrane space of autophagosomes (right panel). The signal is absent by omitting the primary AB from during the staining procedure (left panel).

Supplementary Figure 2. Plekhg5 depletion in SOD1^{G93A} mice does not affect p62 accumulations within the spinal cord.

A: Spinal cord cross section stained for p62.

B: Quantification of p62 clusters. Mean±SEM. One-way ANOVA; Tukey's Multiple Comparisons. *Plekhg5*$^{+/+}$, n=3; *Plekhg5*$^{-/-}$, n=4; *Plekhg5*$^{+/+}$ *Sod1*^{G93A}, n=4; *Plekhg5*$^{-/-}$ *Sod1*^{G93A}, n=4.

C, D: Spinal cord cross sections co-stained for p62 and ChAT (C). High magnification images of an individual spinal motoneuron (D). p62 clusters were absent in Plekhg5-deficient mice, and only detectable in SOD1^{G93A}-expressing mice.

Supplementary Figure 3. Motoneuron survival is improved in *Plekhg5*$^{-/-}$ *SOD1*^{G93A} mice compared to *Plekhg5*$^{+/+}$ *Sod1*^{G93A}.

A, B: ChAT staining in spinal cord sections of *Plekhg5*$^{+/+}$, *Plekhg5*$^{-/-}$, *Plekhg5*$^{+/+}$ *Sod1*^{G93A} and *Plekhg5*$^{-/-}$ *Sod1*^{G93A} mice at disease onset (A) and disease endstage (B) show reduced ChAT levels in *Plekhg5*$^{+/+}$ *Sod1*^{G93A} and *Plekhg5*$^{-/-}$ *Sod1*^{G93A} mice at disease endstage. MN survival in *Plekhg5*$^{-/-}$ *Sod1*^{G93A} mice is slightly, but significantly improved at disease endstage compared to *Plekhg5*$^{+/+}$ *SOD1*^{G93A} mice. Scale bar: 200 µm.

C: Quantification of ChAT^{+} cells. Mean±SEM. T-test, two-tailed. Onset: *Plekhg5*$^{+/+}$, n=3; *Plekhg5*$^{-/-}$, n=4; *Plekhg5*$^{+/+}$ *Sod1*^{G93A}, n=4; *Plekhg5*$^{-/-}$ *Sod1*^{G93A}, n=3. Endstage: *Plekhg5*$^{+/+}$ *Sod1*^{G93A}, n=3; *Plekhg5*$^{-/-}$ *Sod1*^{G93A}, n=4.

Supplementary Figure 4. Analysis of NMJs Morphology and innervation.

A, B: NMJs visualized by BTX, synaptophysin and NF-M staining in *Plekhg5*$^{+/+}$, *Plekhg5*$^{-/-}$, *Plekhg5*$^{+/+}$ *Sod1*^{G93A} and *Plekhg5*$^{-/-}$ *Sod1*^{G93A} mice. Note that balloon-like NMJs are only present in *Plekhg5*$^{-/-}$ and *Plekhg5*$^{-/-}$ *Sod1*^{G93A} mice (B).

C: Quantification of denervated NMJs and balloon-like NMJs. NMJ denervation is significantly increased in *Plekhg5*$^{+/+}$ *Sod1*^{G93A} compared to *Plekhg5*$^{-/-}$ and *Plekhg5*$^{-/-}$ *Sod1*^{G93A} mice at disease onset and endstage. Balloon-like NMJs structures in *Plekhg5*$^{-/-}$ and *Plekhg5*$^{-/-}$ *Sod1*^{G93A} mice increase at disease endstage but do not coincide with NMJ denervation. Mean±SEM One-way ANOVA; Tukey's Multiple Comparisons. Onset: *Plekhg5*$^{+/+}$, n=5; *Plekhg5*$^{-/-}$, n=4; *Plekhg5*$^{+/+}$ *Sod1*^{G93A}, n=6; *Plekhg5*$^{-/-}$ *Sod1*^{G93A}, n=5. Endstage: *Plekhg5*$^{+/+}$, n=4; *Plekhg5*$^{-/-}$, n=4; *Plekhg5*$^{+/+}$ *Sod1*^{G93A}, n=5; *Plekhg5*$^{-/-}$ *Sod1*^{G93A}, n=5.

Supplementary Figure 5. RNAseq data validation by qPCR.

Microglia activation is increased in *Plekhg5*$^{+/+}$ *Sod1*^{G93A}. Expression of selected transcripts associated with microglia activation were analyzed by qPCR. *Plekhg5*$^{+/+}$, n=3; *Plekhg5*$^{-/-}$, n=3; *Plekhg5*$^{+/+}$ *Sod1*^{G93A}, n=3; *Plekhg5*$^{-/-}$ *Sod1*^{G93A}, n=5. Mean±SEM. One-way ANOVA; Tukey's Multiple Comparisons.

Figure 1

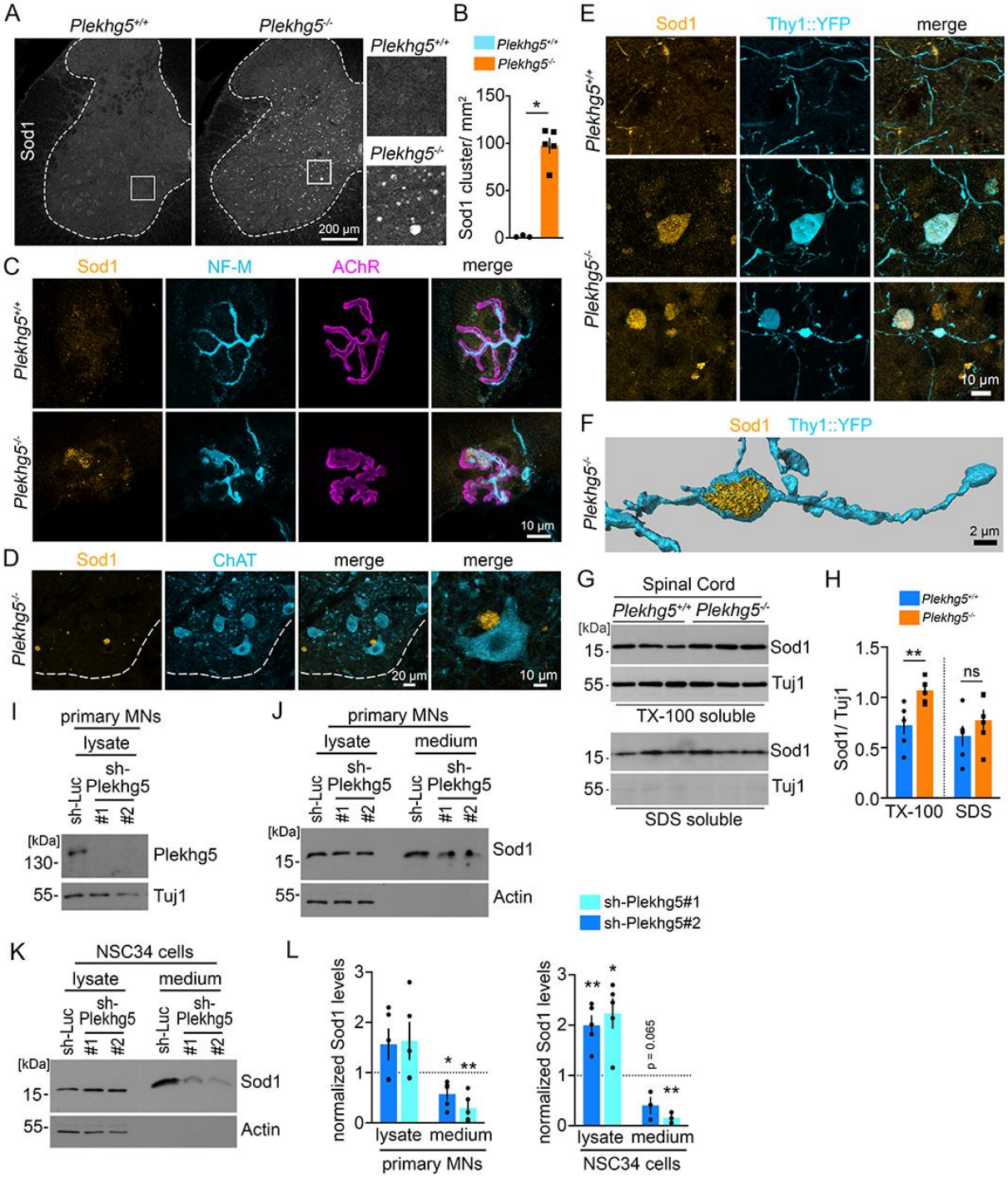
A
Plekhg5+/+
Plekhg5-/-
Sod1
200 µm
B
Plekhg5+/+
Plekhg5-/-
Sod1 cluster/ mm2
150
100
50
0
*
C
Sod1
NF-M
AChR
merge
10 µm
D
Sod1
ChAT
merge
merge
20 µm
10 µm
E
Sod1
Thy1::YFP
merge
10 µm
F
Sod1 Thy1::YFP
2 µm
G
Spinal Cord
Plekhg5+/+ Plekhg5-/-
[kDa]
15-
55-
Sod1
Tuj1
TX-100 soluble
SDS soluble
H
Plekhg5+/+
Plekhg5-/-
Sod1/ Tuj1
1.5
1.0
0.5
0.0
**
ns
TX-100
SDS
I
primary MNs
lysate
sh-Luc
sh-Plekhg5 #1
sh-Plekhg5 #2
[kDa]
130-
55-
Plekhg5
Tuj1
J
primary MNs
lysate
medium
sh-Luc
sh-Plekhg5 #1
sh-Plekhg5 #2
[kDa]
15-
55-
Sod1
Actin
sh-Plekhg5#1
sh-Plekhg5#2
K
NSC34 cells
lysate
medium
sh-Luc
sh-Plekhg5 #1
sh-Plekhg5 #2
[kDa]
15-
55-
Sod1
Actin
L
normalized Sod1 levels
3
2
1
0
*
**
lysate medium
primary MNs
normalized Sod1 levels
**
*
p = 0.065
**
lysate medium
NSC34 cells

Figure 2

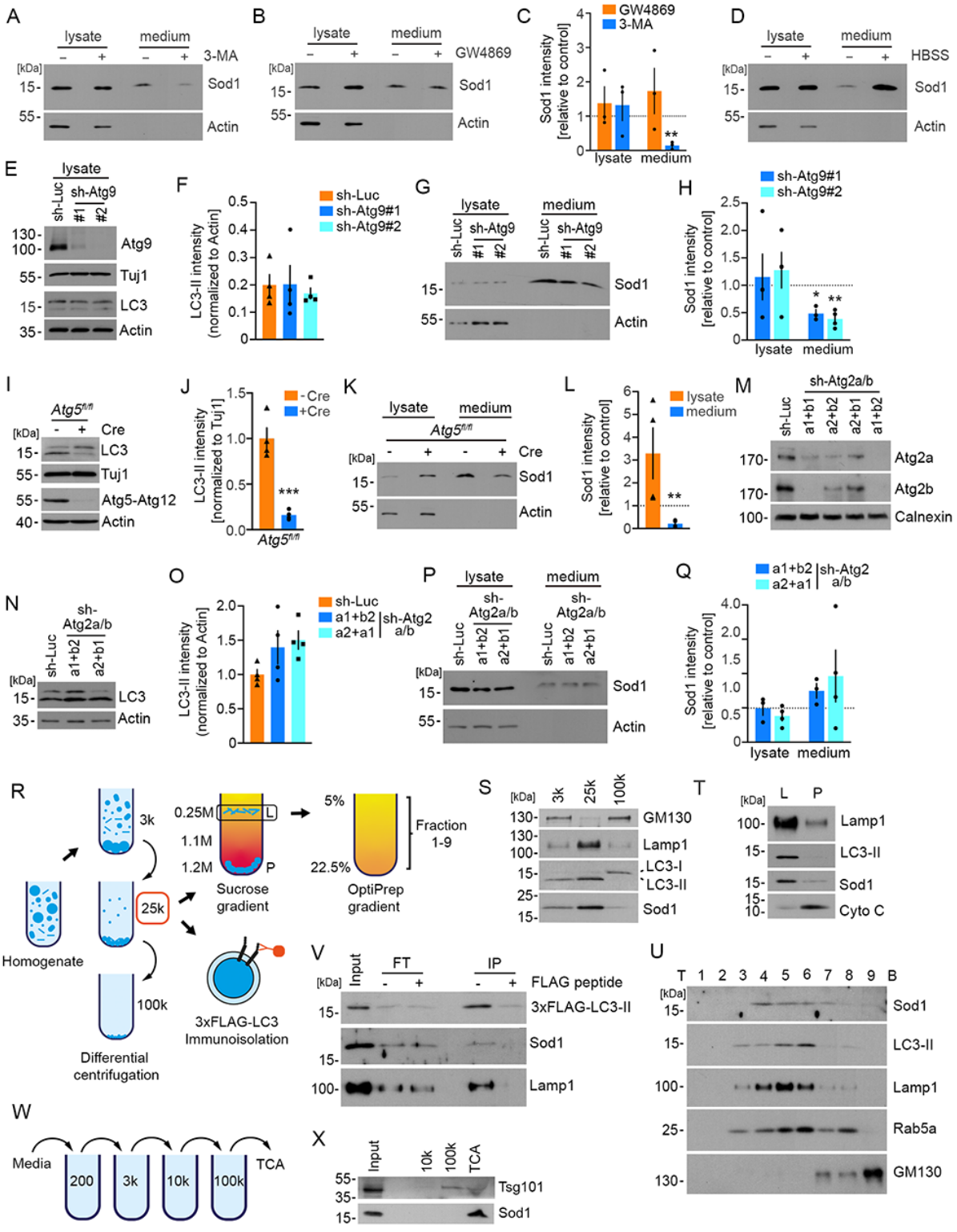
A
lysate
medium
3-MA
Sod1
Actin
B
GW4869
C
GW4869
3-MA
Sod1 intensity [relative to control]
D
HBSS
E
sh-Luc
sh-Atg9 #1
#2
Atg9
Tuj1
LC3
F
LC3-II intensity (normalized to Actin)
sh-Luc
sh-Atg9#1
sh-Atg9#2
G
H
I
Atg5fl/fl
Cre
Atg5-Atg12
J
LC3-II intensity [normalized to Tuj1]
-Cre
+Cre
K
L
M
sh-Atg2a/b
Atg2a
Atg2b
Calnexin
N
sh-Atg2a/b
O
a1+b2
a2+a1
sh-Atg2 a/b
P
Q
R
3k
25k
100k
Homogenate
Differential centrifugation
0.25M
1.1M
1.2M
Sucrose gradient
5%
22.5%
OptiPrep gradient
Fraction 1-9
S
GM130
Lamp1
LC3-I
LC3-II
T
L
P
Cyto C
U
Rab5a
V
Input
FT
IP
FLAG peptide
3xFLAG-LC3-II
3xFLAG-LC3 Immunoisolation
W
Media
200
3k
10k
100k
TCA
X
Tsg101

Figure 3

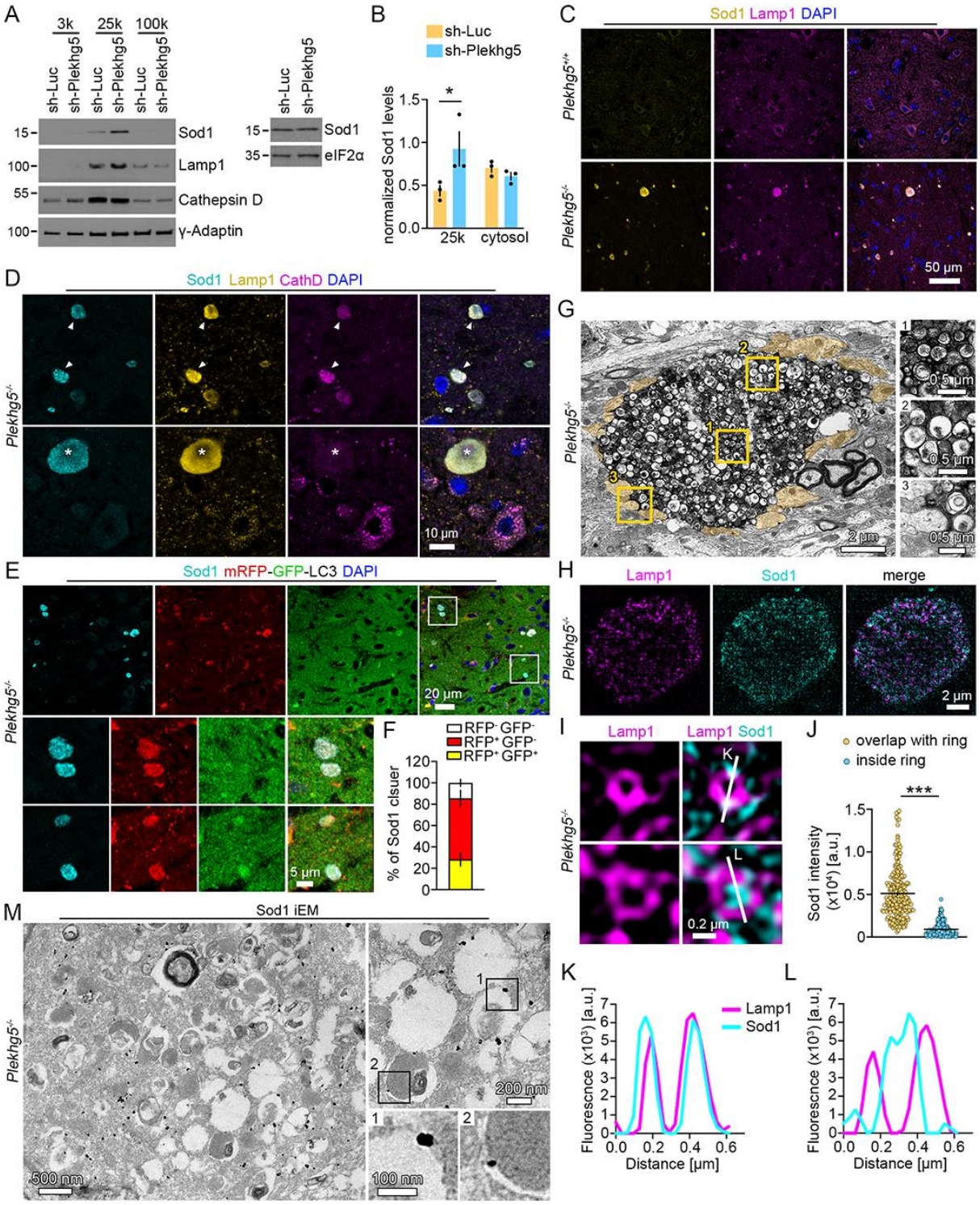
A
3k
25k
100k
sh-Luc
sh-Plekhg5
Sod1
Lamp1
Cathepsin D
γ-Adaptin
eIF2α
B
sh-Luc
sh-Plekhg5
normalized Sod1 levels
25k
cytosol
C
Sod1 Lamp1 DAPI
Plekhg5+/+
Plekhg5-/-
50 μm
D
Sod1 Lamp1 CathD DAPI
Plekhg5-/-
10 μm
E
Sod1 mRFP-GFP-LC3 DAPI
Plekhg5-/-
20 μm
5 μm
F
RFP- GFP-
RFP+ GFP-
RFP+ GFP+
% of Sod1 clsuer
G
Plekhg5-/-
2 μm
0.5 μm
H
Lamp1
Sod1
merge
Plekhg5-/-
2 μm
I
Lamp1
Lamp1 Sod1
Plekhg5-/-
0.2 μm
J
overlap with ring
inside ring
***
Sod1 intensity (x10⁴) [a.u.]
K
L
Lamp1
Sod1
Fluorescnce (x10³) [a.u.]
Distance [μm]
M
Sod1 iEM
Plekhg5-/-
500 nm
200 nm
100 nm

Figure 4

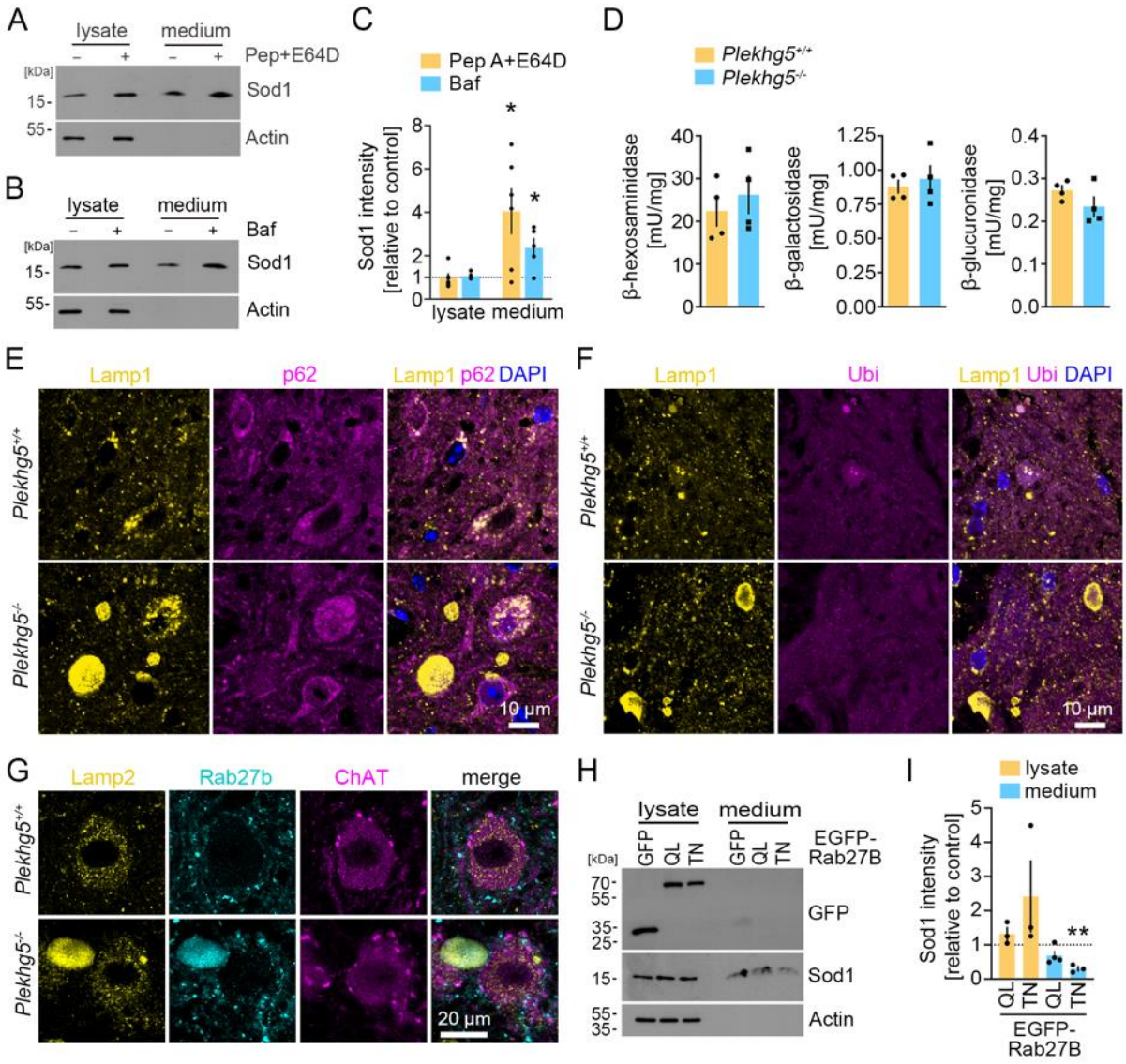
A
lysate
medium
Pep+E64D
[kDa]
15-
55-
Sod1
Actin
B
lysate
medium
Baf
[kDa]
15-
55-
Sod1
Actin
C
Pep A+E64D
Baf
Sod1 intensity [relative to control]
lysate medium
D
Plekhg5+/+
Plekhg5-/-
β-hexosaminidase [mU/mg]
β-galactosidase [mU/mg]
β-glucuronidase [mU/mg]
E
Lamp1
p62
Lamp1 p62 DAPI
Plekhg5+/+
Plekhg5-/-
10 µm
F
Lamp1
Ubi
Lamp1 Ubi DAPI
Plekhg5+/+
Plekhg5-/-
10 µm
G
Lamp2
Rab27b
ChAT
merge
Plekhg5+/+
Plekhg5-/-
20 µm
H
lysate
medium
GFP
QL
TN
GFP
QL
TN
EGFP-Rab27B
[kDa]
70-
55-
35-
25-
15-
55-
35-
GFP
Sod1
Actin
I
lysate
medium
Sod1 intensity [relative to control]
**
QL
TN
QL
TN
EGFP-Rab27B

Figure 5

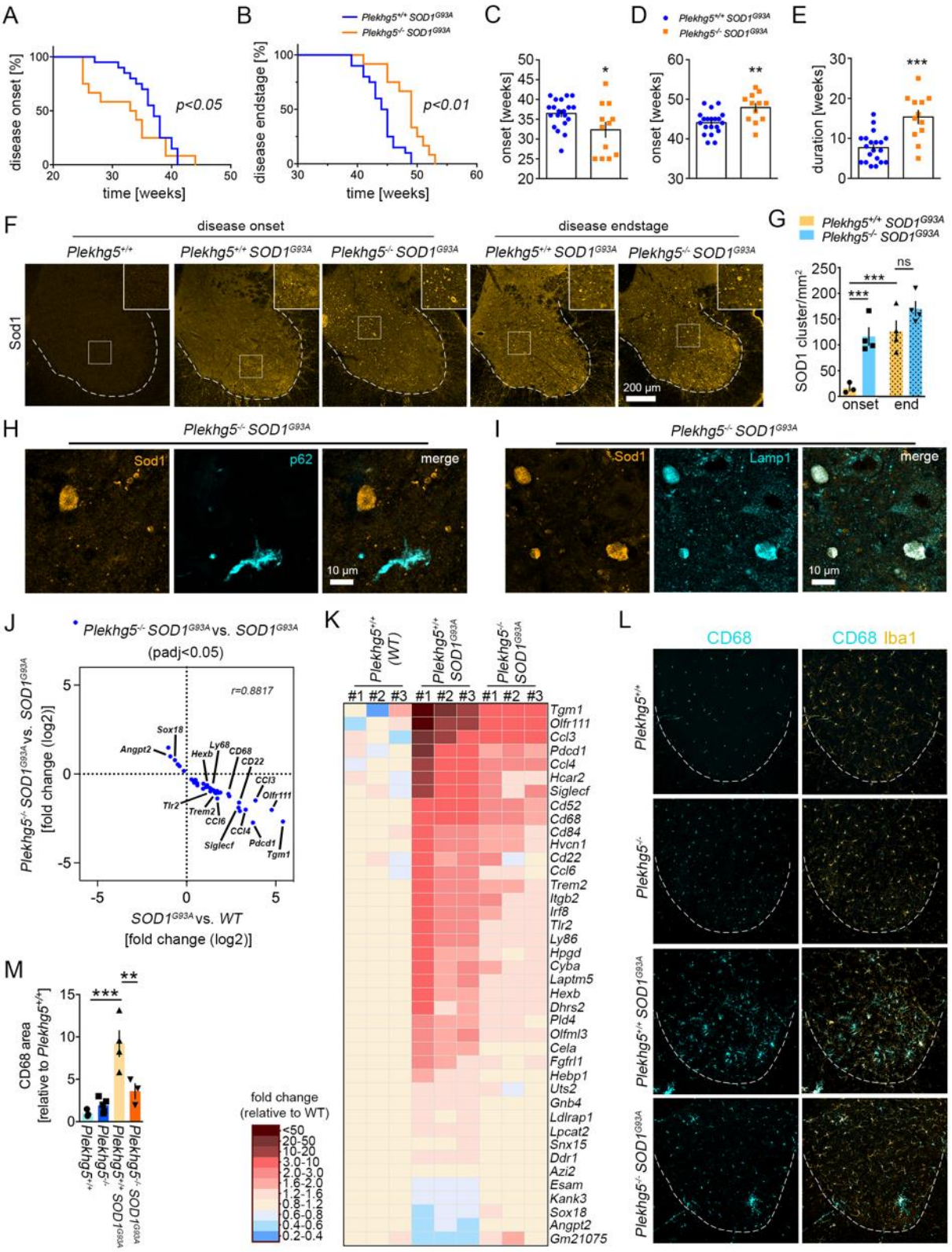
A
disease onset [%]
time [weeks]
p<0.05
B
disease endstage [%]
time [weeks]
p<0.01
C
onset [weeks]
D
onset [weeks]
E
duration [weeks]
F
disease onset
disease endstage
Sod1
200 µm
G
SOD1 cluster/mm²
onset
end
ns
H
Sod1
p62
merge
10 µm
I
Sod1
Lamp1
merge
10 µm
J
(padj<0.05)
r=0.8817
[fold change (log2)]
K
fold change (relative to WT)
Tgm1
Olfr111
Ccl3
Pdcd1
Ccl4
Hcar2
Siglecf
Cd52
Cd68
Cd84
Hvcn1
Cd22
Ccl6
Trem2
Itgb2
Irf8
Tlr2
Ly86
Hpgd
Cyba
Laptm5
Hexb
Dhrs2
Pld4
Olfml3
Cela
Fgfrl1
Hebp1
Uts2
Gnb4
Ldlrap1
Lpcat2
Snx15
Ddr1
Azi2
Esam
Kank3
Sox18
Angpt2
Gm21075
L
CD68
CD68 Iba1
M
CD68 area
[relative to Plekhg5+/+]

Figure 6

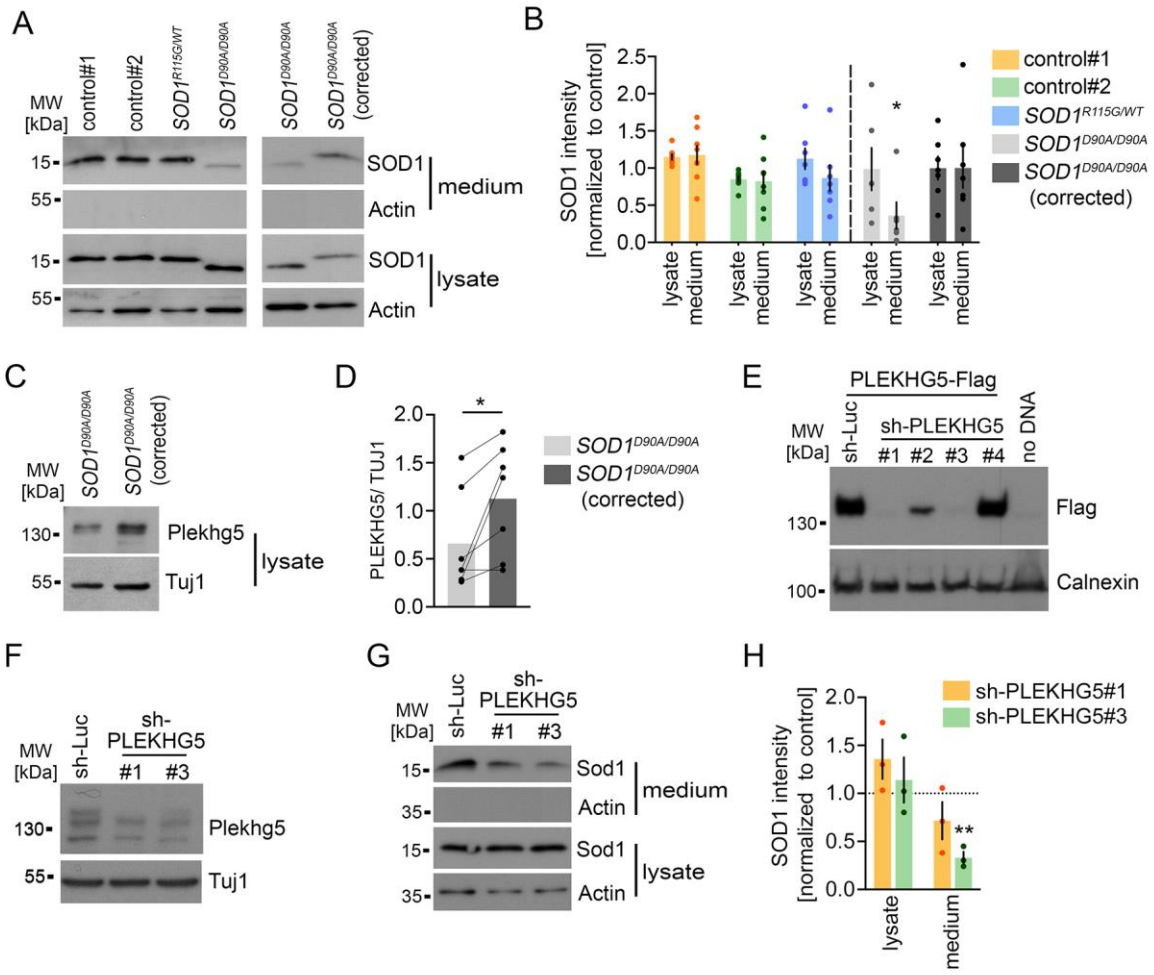
A
MW [kDa]
control#1
control#2
SOD1R115G/WT
SOD1D90A/D90A
SOD1D90A/D90A
SOD1D90A/D90A (corrected)
15
55
SOD1
Actin
medium
lysate
B
SOD1 intensity [normalized to control]
control#1
control#2
SOD1R115G/WT
SOD1D90A/D90A
SOD1D90A/D90A (corrected)
lysate
medium
C
MW [kDa]
SOD1D90A/D90A
SOD1D90A/D90A (corrected)
130
55
Plekhg5
Tuj1
lysate
D
PLEKHG5/ TUJ1
SOD1D90A/D90A
SOD1D90A/D90A (corrected)
E
PLEKHG5-Flag
MW [kDa]
sh-Luc
sh-PLEKHG5
#1 #2 #3 #4
no DNA
130
100
Flag
Calnexin
F
MW [kDa]
sh-Luc
sh-PLEKHG5
#1 #3
130
55
Plekhg5
Tuj1
G
MW [kDa]
sh-Luc
sh-PLEKHG5
#1 #3
15
35
Sod1
Actin
medium
lysate
H
SOD1 intensity [normalized to control]
sh-PLEKHG5#1
sh-PLEKHG5#3
lysate
medium

Supplementary Figure 1

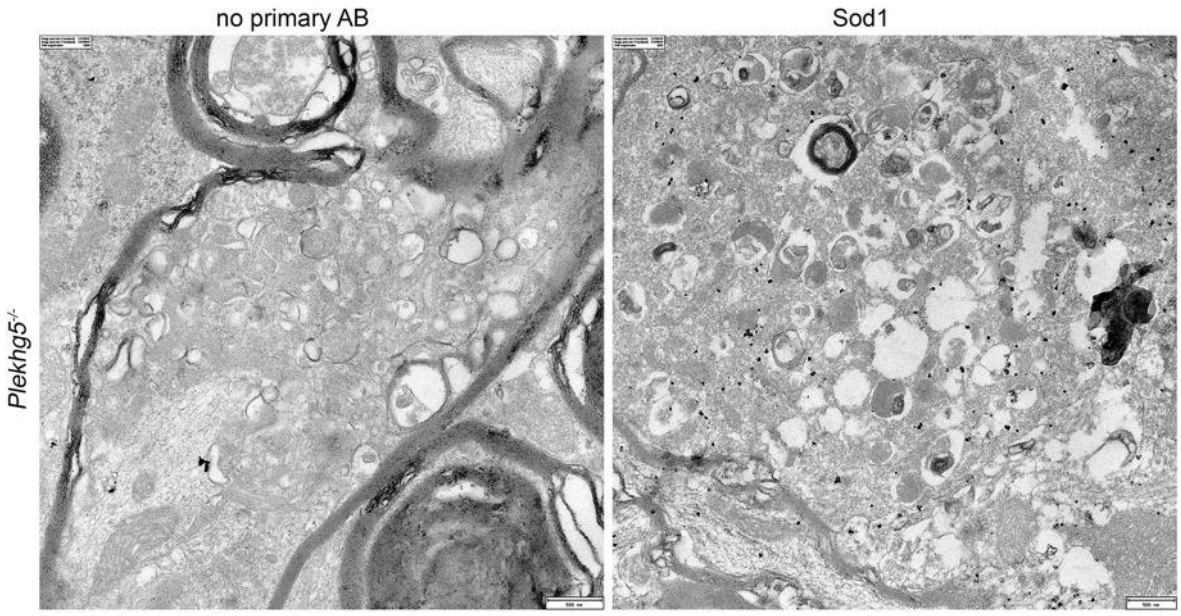

Supplementary Figure 2

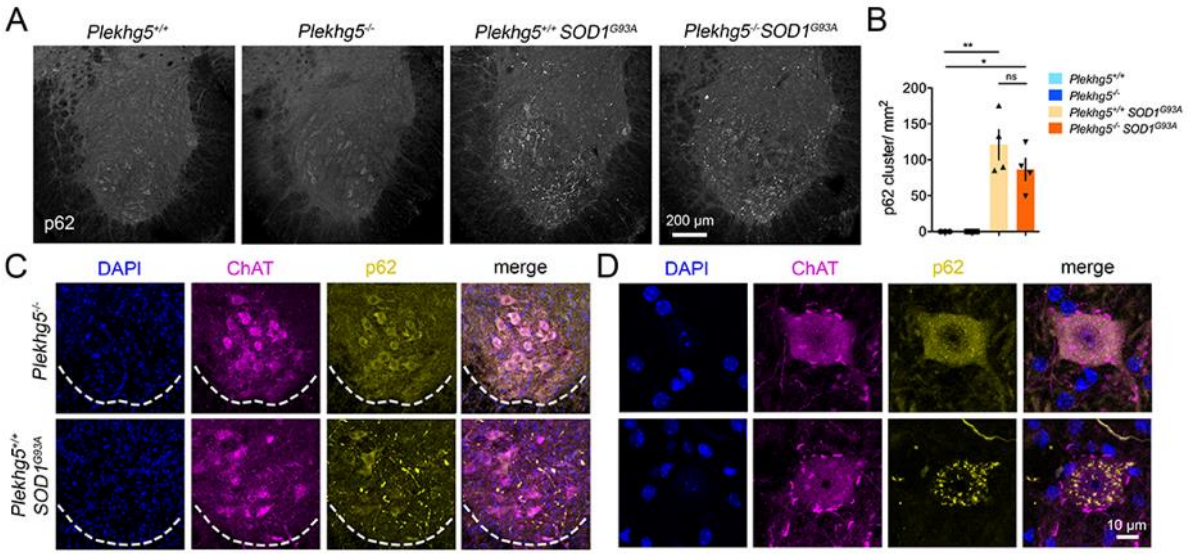

Supplementary Figure 3

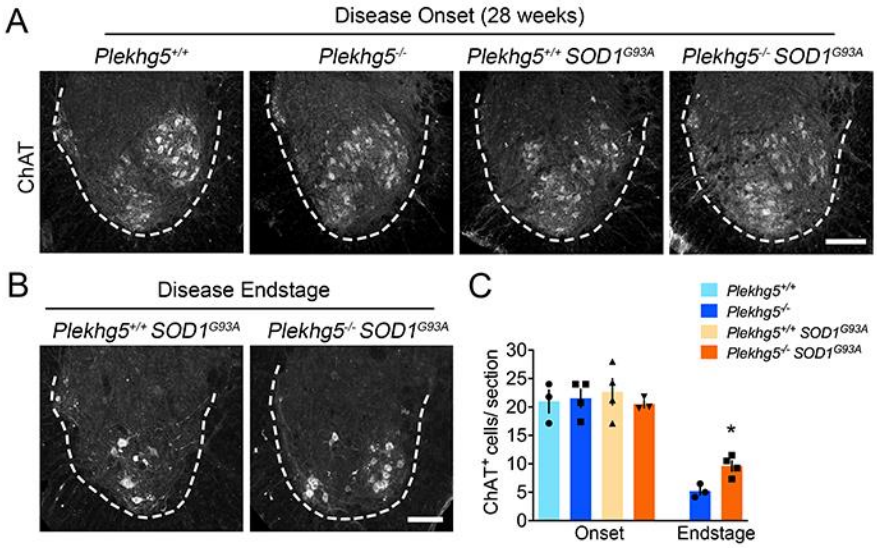

Supplementary Figure 4

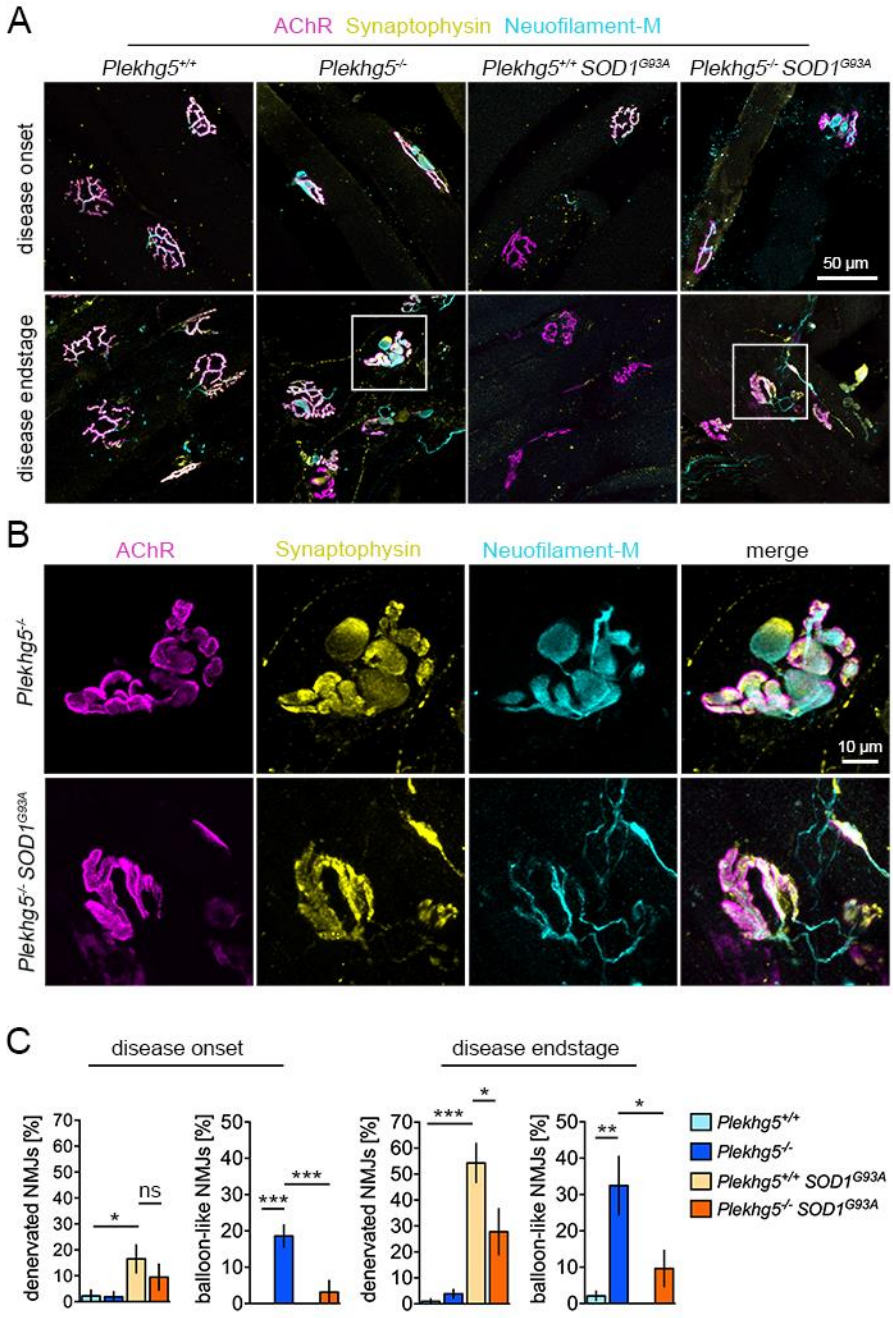

Supplementary Figure 5

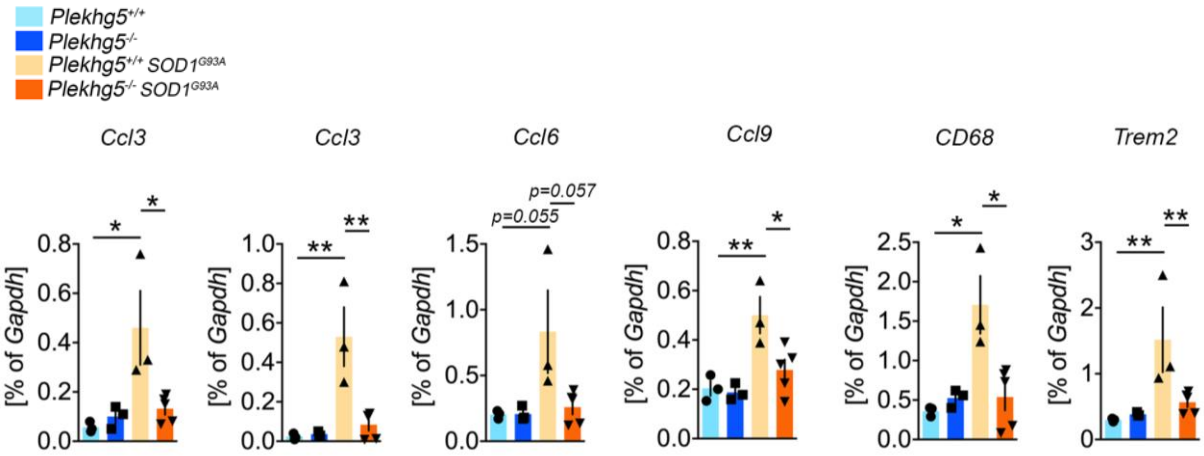

8 Appendix

8.1 List of Abbreviations

A4V	Alanine at codon 4 changed to valine
ACh	Acetylcholine
AChE	Acetylcholinesterase
AChR	Acetylcholine receptor
ALS	Amyotrophic Lateral Sclerosis
ATG proteins	Autophagy-related proteins
BL	Basal lamina
ChR2-YFP	Channelrhodopsin-2-YFP
CMT	Charcot-Marie-Tooth disease
CNS	Central nerve system
CNTF	Cliary neurotrophic factor
D90A	Aspartic acid at codon 90 changed to alanine
dHMN	Distal hereditary motor neuropathy
DSMA4	Distal spinal muscular atrophy
FACS	Fluorescence Activated Cell Sorting
fALS	Familial ALS
GEF	Guanine exchange factor
iPSCs	Induced pluripotent stem cells
iPSZ	Induzierte pluripotente Stammzellen
LMN	Lower motor neuron
LROs	Lysosomal-related organelles
MN	Motor neuron
MND	Motor neuron disease
MNE	Motoneuronerkrankung
mTORC1	Mammalian target of rapamycin complex 1

NME	Neuromuskuläre Endplatte
NMJ	Neuromuscular junction
PLEKHG5/Plekhg5	Pleckstrin homology domain-containing family G member 5
PNS	Peripheral nervous system
sALS	Sporadic ALS
SMA	Spinal muscle atrophy
SMN1	Survival of motor neuron 1
SOD1/Sod1	Superoxide dismutase 1
SV	Synaptic vesicles
UMN	Upper motor neuron
UPS	Unconventional protein secretion

8.2 List of Figures

.

8.3 List of Publications

Miljus N, **Massih B**, Weis MA, Rison JV, Bonnas CB, Sillaber I, Ehrenreich H, Geurten BRH, & Heinrich R. Neuroprotection and endocytosis: erythropoietin receptors in insect nervous systems. J Neurochem. 2017;141(1).

Lüningschrör P, Slotta C, Heimann P, Briese M, Weikert UM, **Massih B**, Appenzeller S, Sendtner M, Kaltschmidt C, & Kaltschmidt B. Absence of Plekhg5 Results in Myelin Infoldings Corresponding to an Impaired Schwann Cell Autophagy, and a Reduced T-Cell Infiltration Into Peripheral Nerves. Front Cell Neurosci. 2020 Jul 7;14:185.

Massih B, Veh A, Schenke M, Mungwa S, Seeger B, Selvaraj BT, Chandran S, Reinhardt P, Sterneckert J, Hermann A, Sendtner M, & Lüningschrör P. A 3D cell culture system for bioengineering human neuromuscular junctions to model ALS. Front Cell Dev Biol. 2023 Feb 14;11:67.

Hahn N, Büschgens L, Schwedhelm-Domeyer N, Bank S, Geurten BRH, Neugebauer P, **Massih B**, Göpfert MC, & Heinrich R. The Orphan Cytokine Receptor CRLF3 Emerged With the Origin of the Nervous System and Is a Neuroprotective Erythropoietin Receptor in Locusts. Front Mol Neurosci. 2019 Oct 11;12.

In preparation for publication:

Plekhg5 regulates the unconventional secretion of Sod1 by presynaptic secretory autophagy. Amy-Jayne Hutchings*, **Bita Massih***, Alexander Veh*, Neha Jadhav Giridhar, Christina Angerer, Maren Schenke, Bhuvaneish T. Selvaraj, Siddharthan Chandran, Peter Reinhardt, Jared Sterneckert, Bettina Seeger, Christian Stigloher, Michael Briese, Andreas Hermann, Markus Damme, Michael Sendtner, Patrick Lüningschrör#

8.4 Statement of individual author contributions to figures and tables of included manuscript in the dissertation

Manuscript 1 (complete reference): A 3D cell culture system for bioengineering human neuromuscular junctions to model ALS					
Figure	**Author Initials,** Responsibility decreasing from left to right				
1	BM	AV			
2	BM	MSch	PL	SM	
3	BM	AV	MSch	PL	
4	BM	MSch			

Explanations (if applicable): The study in manuscript 1 was conducted with the help of the listed authors. Further, BS, BTS, SC, PR, JS, AH contributed by providing the human iPSC-lines.

Manuscript 2 (complete reference): Plekhg5 regulates the unconventional secretion of Sod1 by presynaptic secretory autophagy (Status: Unpublished)					
Figure	**Author Initials,** Responsibility decreasing from left to right				
1	BM, AV				
2	BM	NJG	CA	PL	
3	AV	NJG	CA	CS	
4	BM	MD	PL	TO	
5	AJH	AV	PL	MB	
6	BM	TO	MSch		
Supplementary Fig.1	AV	CS			
Supplementary Fig.2	AJH				
Supplementary Fig.3	AJH	AV			
Supplementary Fig.4	AJH				
Supplementary Fig.5	BM	AJH	PL		

Explanations (if applicable): The study in manuscript 2 was conducted with the help of the listed authors. Further, BS, BTS, SC, PR, JS, AH, SP contributed by providing the human iPSC-lines.

I also confirm my primary supervisor's acceptance.

Doctoral Researcher's Name Date Place Signature

8.5 Statement of individual author contributions and of legal second publication rights to manuscripts included in the dissertation

Manuscript 1 (complete reference): A 3D cell culture system for bioengineering human neuromuscular junctions to model ALS					
Participated in	**Author Initials,** Responsibility decreasing from left to right				
Study Design Methods Development	BM	PL	SM		
Data Collection	BM	MSch			
Data Analysis and Interpretation	BM	AV			
Manuscript Writing					
Writing of Introduction	BM	PL	MS		
Writing of Materials & Methods	BM	PL			
Writing of Discussion	BM	PL	MS		
Writing of First Draft	BM	PL			

Explanations (if applicable): The study in manuscript 1 was conducted with the help of the listed authors. Further, BS, BTS, SC, PR, JS, AH contributed by providing the human iPSC-lines.

Manuscript 2 (complete reference): Plekhg5 regulates the unconventional secretion of Sod1 by presynaptic secretory autophagy (Status: Unpublished)					
Participated in	**Author Initials,** Responsibility decreasing from left to right				
Study Design Methods Development	PL	AJH, BM, AV			
Data Collection	AJH, BM, AV	NJG	MD	CA, TO, MSch	
Data Analysis and Interpretation	AJH, BM, AV	PL	MD	MB	CS
Manuscript Writing					
Writing of Introduction	PL	BM, AV	AJH	MD	MS
Writing of Materials & Methods	PL, BM, AV				
Writing of Discussion	PL	BM, AV	AJH	MD	MS
Writing of First Draft	PL	BM, AV			

Explanations (if applicable): The study in manuscript 2 was conducted with the help of the listed authors. Further, BS, BTS, SC, PR, JS, AH, SP contributed by providing the human iPSC-lines.

If applicable, the doctoral researcher confirms that she/he has obtained permission from both the publishers (copyright) and the co-authors for legal second publication.

The doctoral researcher and the primary supervisor confirm the correctness of the above mentioned assessment.

Doctoral Researcher's Name	Date	Place	Signature

Primary Supervisor's Name	Date	Place	Signature

8.6 Affidavit

Affidavit

I hereby confirm that my thesis entitled "**Human stem cell-based models to analyze the pathophysiology of motor neuron diseases**" is the result of my own work. I did not receive any help or support from commercial consultants. All sources and / or materials applied are listed and specified in the thesis.

Furthermore, I confirm that this thesis has not yet been submitted as part of another examination process neither in identical nor in similar form.

Place, Date Signature

Eidesstattliche Erklärung

Hiermit erkläre ich an Eides statt, die Dissertation "**Humane Stammzell-basierte Modelle zur Analyse der Pathophysiologie von Motoneuronerkrankungen**" eigenständig, d.h. insbesondere selbständig und ohne Hilfe eines kommerziellen Promotionsberaters, angefertigt und keine anderen als die von mir angegebenen Quellen und Hilfsmittel verwendet zu haben.

Ich erkläre außerdem, dass die Dissertation weder in gleicher noch in ähnlicher Form bereits in einem anderen Prüfungsverfahren vorgelegen hat.

Ort, Datum Unterschrift

8.7 Acknowledgement

First and foremost, I would like to express my gratitude to **Dr. Patrick Lüningschrör** for giving me the opportunity to pursue my doctoral research on this interesting project. I thank him for his excellent guidance, his time, and his patience. I also thank him for continuous encouragement and confidence in me and my work. His contagious enthusiasm for science has influenced me for my scientific career.

Secondly, I want to thank my second supervisor **Prof. Dr. Erhard Wischmeyer** for the continuous support that has certainly contributed to the success of the project. I thank him for the commitment to my supervision and for valuable discussions and suggestions during our annual meetings.

I want to thank my third supervisor **Prof. Dr. Dr. Andreas Hermann** for his helpful support and guidance over the last years. Particularly, I would like to thank him for the great collaboration which contributed to the success of the project and the publications.

Likewise, I want to thank **Prof. Dr. Carmen Villmann** for taking over the job of the chairperson.

I thank all my colleagues and collaborators who contributed to the project and publications, specially I thank **Bettina Seeger** and **Maren Schenke**. I also thank the **Lüningschrör Group**, **Janina**, **Alex** and **Neha**, for the support and always-helpful hand whenever I needed it.

A heartfelt thanks goes to **Martin Hambrecht** for proofreading.

Thank you, **Luisa**, for proofreading and so much more, and thank you **Saeede**, **Hossein**, **Max** and **Orlando**.

Ein besonderer Dank gilt meinen Eltern und meinem Bruder, die mich zu jeder Zeit unterstützt haben und mir den Weg zum PhD ermöglicht haben.

Mein größter Dank gilt Mario.

8.8 Curriculum Vitae

„Krabbenexperimente!”